LUMINESCENT ENHANCEMENT OF EUROPIUM METAL-BASED CALCIUM FLUORIDE NANOPARTICLES USING SURFACE MODIFICATIONS: A THEORETICAL AND AN EXPERIMENTAL STUDY OF THE ANTENNA EFFECT

A thesis presented to the faculty of the Graduate College of Western Carolina University in partial fulfillment of the requirements for the degree of Master of Science in Chemistry

By

Matteo Fratarcangeli

Advisor: Dr. Channa De Silva

Professor of Chemistry

Department of Chemistry & Physics

Committee Members: Dr. Brian Dinkelmeyer, Chemistry & Physics

Dr. Robert Youker, Biology

April 2023

ACKNOWLEDGEMENTS

I would like to thank all of the professors and peers that have supported me so far, as well as all the institutions that made my research possible. In particular: I would like to extend my thanks to the Department of Chemistry and Physics and the Academic Project Grant (APG) Program for funding my project during the school year and the Summer Undergraduate Research Program (SURP) and the Summer Graduate Research Assistantship for funding my project during the summer. I would like to thank the IT Department for providing us with the ability to use a powerful virtual machine. I would like to thank Dr. Scott Huffman for helping me resolve problems that I encountered with the FT-IR and Mr. Matt Burleson for being so available when instrumentation issues arose. Most importantly, I would like to thank Dr. De Silva for all the support and many experiences that he allowed me to participate in. Finally, I would like to thank the entirety of the chemistry graduate students for the support, the advice and patience.

TABLE OF CONTENT

LIST OF FIGURES

LIST OF TABLES

ABSTRACT

LUMINESCENT ENHANCEMENT OF EUROPIUM METAL-BASED CALCIUM FLUORIDE NANOPARTICLES USING SURFACE MODIFICATIONS: A THEORETICAL AND EXPERIMETAL STUDY OF THE ANTENNA EFFECT

Matteo Fratarcangeli, Master of Science in Chemistry

Western Carolina University (April 2023)

Advisor: Dr. Channa De Silva

Europium metal-based nanomaterials show promising applications in optical imaging of biological samples, bio-analytical sensing, biomedical assay technologies, and high throughput drug screening. They present unique photophysical properties including monochromatic light emission, long luminescent lifetimes enabling time-resolved measurements, limited photobleaching, large Stokes shifts, and negligible ligand field effects. Ligand design and understanding their electronic properties for enhancing the luminescent quantum efficiency of europium-based probes is extremely important for their potential applications in cellular imaging. Among the europium metal-based nanocrystals, europium-doped calcium fluoride nanoparticles are suitable for cellular imaging due to their high biocompatibility compared to previously studied crystal matrices including $NaYF_4$ and LaF_3. However, their luminescent efficiencies should be further improved for cellular imaging. In this work, we report a. computational studies of the electronic properties of europium fluorobenzoate complexes aiming to better understand the electronic structure and the luminescent efficiency for designing highly luminescent imaging probes, b. surface modifications of europium-doped calcium fluoride nanoparticles for enhancing their luminescence, and c. preliminary imaging of nanoparticles using epifluorescent microscopy. Our computational studies revealed that the calculated structural parameters agree well with the experimental values. On average, the calculated metal-ligand bonds are shorter in monohydrate complexes compared to those observed for dihydrate complexes. This could affect the electronic excited states and the luminescent efficiency of the complexes. The optimal ISC and ET were identified as 1.1548 eV and 1.3746 eV, respectively for the

Eu^{3+} fluorobenzoate complexes. The correlation among the experimental luminescent quantum yields and the calculated electronic excited states were analyzed providing insight into designing molecular structures for improving europium-centered luminescence. The synthesis of the europium-doped nanoparticles was successful. The smallest nanoparticles had a diameter of 40 nm. X-ray diffraction studies revealed the cubic face-centered crystal structure of CaF_2. Surface modification was confirmed using FT-IR and UV-Vis spectroscopy. The nanoparticles present a λ_{max} at 341 nm and a bright orange emission band at 613 nm. The surface functionalization promoted ligand-to-metal energy transfer process resulting in europium-centered luminescence. The luminescent quantum yield of the nanoparticles depends on the size and surface coating. Nanoparticles with an average size of 470 nm and 160 nm presented a maximum luminescent quantum yield of 11.8% and 23.7%, respectively. Preliminary imaging studies of nanoparticles using epifluorescence microscopy revealed that the nanoparticles are clearly visible under 365 nm excitation and can have potential cellular imaging applications.

CHAPTER ONE: INTRODUCTION

1.1 Background

1.1.1 Computational Chemistry

Computational chemistry is an established field of chemistry that has gained popularity in the past few decades due to hardware and software improvements. Also, powerful programs that were once only available for large computers, have now been rewritten to run on personal and inexpensive machines. The workings of programs are now better described by their manual and other books written to explain inexperienced users how to use these programs[1]. Computational chemistry simulates chemical structures and reactions numerically, using as a foundation, the fundamental law of physics[2]. The produced theoretical models are extremely powerful and can be used to investigate a vast variety of properties, such as:

- Molecular geometry: prediction of 3D structure of molecules, including bond lengths, bond angles, and dihedral angles;
- Molecule and transition state energies: revealing which isomer will be favored at equilibrium and, the reaction time (by comparing the transition state, reactants, and products energies);
- Chemical reactivity: identification of nucleophilic and electrophilic sites to predict where the molecule will be attacked by different reagents, elucidating likely modes of catalysis;
- IR, UV, and NMR spectra: calculating spectra to identify unknown molecules;
- Interaction of substrate with enzyme: studying how a new drug interacts with a protein and its active site;
- Physical properties of substances: identification of properties of individual molecules as well as the molecular behavior in bulk materials.

To study those questions, computational chemists have a selection of theories to choose from: molecular mechanics, ab-initio calculations, semiempirical calculations, density functional theory (DFT) calculations, and molecular dynamics calculations[1]. Each of these theories have their own strength and

weaknesses and can be used in different applications. For example, molecular mechanics is relatively inexpensive to run, but it is not the most precise model. Therefore, it is usually used to optimize structures of large biomolecules. On the other hand, ab-initio and semi-empirical calculations can be computationally intensive and can produce extremely precise results. These two theories are generally used on small molecules that require extremely precise calculations.

1.1.2 Electronic Structure Methods

Electronic structure methods are based on the laws of quantum mechanics instead of classical physics. In this regard, they are all based on the Schrödinger equation, which when solved can provide energies and properties of a molecule. However, the Schrödinger equation can only be solved for the hydrogen atom and for this reason the electronic structure methods are characterized by the different mathematical approximations to the solution of the equation[2].

Semi-empirical calculations use experimentally determined values to simplify the calculation. In other words, they solve approximated forms of the Schrödinger equation that require appropriate parameters for the studied chemical system. On the other hand, ab-initio methods do not use any experimental parameters and instead they use series of rigorous mathematical approximations. These two methods differ in the tradeoff between computational cost and accuracy of results. Semi-empirical calculations have shorter computation times and provide reasonable qualitative and quantitative results when accurate parameter sets exist. Ab-initio calculations provide high quality quantitative and qualitative results but require more powerful computer systems and longer computational time[2].

1.1.3 Density Functional Theory

In the past two decades a new class of electronic structure methods has seen a vast increase in popularity: density functional theory (DFT). DFT differentiates from other theories because it is based on the electron density function (electron/charge density) and not on the Schrödinger equation. Unlike wavefunctions, electron density can be measured by using electron or X-ray diffraction. Apart from being an

experimental observable, the electron density is only a function of electron position, meaning that only three variables are needed (x, y, z). On the other end, the wavefunction has four variables (one spin coordinate and three special coordinates) for every electron in the system[1]. Compared to other electronic structure methods, DFT requires significantly less computational resources due to how it implements electron-electron interactions (electron correlations). DFT methods compute electron correlations using functionals of the electron density. DFT functionals divide the electronic energy into different components that are calculated separately: the kinetic energy, the electron-nuclear interactions, the Coulomb repulsion, and the exchange-correlation term which accounts for the remainder of the electron-electron interactions. In most modern methods, the later term is further divided into the exchange and correlated components which are calculated separately[2].

To date, many functionals have been defined and they generally differ in the way they handle the exchange and correlation components. Local exchange and correlation functionals involve only the electron spin densities. Gradient-corrected (non-local) functionals involve both the electron spin densities and their gradients. Finally, several hybrid functionals have been created which define the exchange component as linear combination of ab-initio, local and gradient-corrected exchange terms. This exchange component is then combined with a local and/or gradient-corrected correlation term. The best-known hybrid functional is Becke's three parameter formulation also known as B3LYP[3–6].

1.1.4 Basis Sets

Basis sets are the mathematical description of orbitals within a studied system and are necessary for every computation. Larger basis sets are more accurate because they impose less limitation on the position of electrons in space. Based on quantum mechanics, electrons have a finite probability of being anywhere in space and to represent this in a computation an infinite basis set would be needed. Basis sets for electronic structure methods use linear combination of gaussian functions to form the orbital. Basis sets assign groups of functions to all atoms in a molecule to approximate their orbitals and the more functions are present the large the basis set will be.

Minimal basis sets contain fixed-size atomic-type orbitals composed of the minimum number of basis functions needed for each atom, for example the hydrogen atom contains one function that describes the 1s orbital and the carbon atom contains 5 functions that describe the 1s, 2s, $2p_x$, $2p_y$, $2p_z$. An example of this is the STO-3G basis set. This basis set uses three gaussian functions for each of its basis functions. Increasing the number of functions is the first way to make a larger basis sets. Split valence basis sets, like 6-31, have two or more sizes for each of valence orbitals. Part of this basis sets is also 6-311G, which is known as a triple split valence basis set and uses a linear combination of three sizes of function for each atomic orbital. While split valence basis sets only allow the orbitals to change size, polarized basis sets allow orbitals to also change shape. In other words, polarized basis sets add orbitals with angular momentum beyond what is required to describe the ground state. They can add d orbitals to carbon atoms and p orbitals to hydrogen atoms. Examples of these basis sets are 6-31G(d) which adds d orbitals to heavy atoms and 6-311G(d,p) which adds d orbitals to heavy atoms and p orbitals to hydrogens, these basis sets are also referred to as 6-31G* and 6-311G**. Finally, to further increase the size of a basis set, diffuse functions can be added. Diffuse functions model larger-size versions of the s and p functional and allow the orbital to occupy a larger region of space. Diffuse functions are useful in systems with lone pairs, significant negative charge, or systems in their excited states. Diffused functions are usually represented by a "+" sign: 6-311+G(d) adds a diffusion function to heavy atoms while the 6-311++G(d) adds a diffusion function to hydrogen atoms as well.

Atoms beyond the third row are generally treated differently than previously discussed. In these atoms, electrons near the nucleus are treated in an approximate way using effective core potential (ECPs). A characteristic of ECPs is that they replace the chemically inert core electrons with effective potentials that incorporate relativistic effects in the calculations, but do not treat each electron individually. This significantly reduces the basis sets needed to perform the calculation without significantly decreasing accuracy of the calculated energies. Some examples of ECPs are the Stuttgart-Dresden large-core and small-core quasi-relativistic effective core potentials[2].

1.1.5 Nanomaterials

In recent years, nanotechnology research has permeated many fields in many different disciplines including chemistry, biology, materials science, and medicine. Few highlights include the use of Au nanospheres for cancer diagnosis and treatment[7] in medicine, encapsulated metal nanoparticles (NPs) used in catalysis[8], plant stimulatory carbon nanomaterials used in agriculture[9] and Al_2O_3 nanoparticles used to increase concrete strength in the construction field[10]. Nanotechnology is the ability to manipulate the structure, behavior, and properties of matter at atomic or near-atomic scale. Nanomaterials are usually defined as materials, systems, and functional devices in the size range of 1-100 nm. The interest in nanotechnology started to flourish when it was demonstrated that properties of materials at the nanoscale are substantially different from properties of the bulk material[11]. Nanomaterials properties are not only dictated by their chemical composition, but also by their morphology and surface properties. Different morphologies of the same bulk material can have substantial differences. An example of this, is the difference in properties between different low-dimensional allotropes of carbon. Carbon nanotubes can be characterized as semiconductors or metals depending on their atomic structure, they also have great mechanic properties and are considered the strongest one-dimensional materials. Graphene on the other hand, has incredibly high tensile strength, electrical and thermal conductivity, and transparency[12]. Other changes in properties between bulk materials and nanomaterials could be attributed to the increase in surface area, which causes increased reactivity and is a major benefit for catalysts, batteries, and absorptive materials.

Nanomaterials show great promise in many fields such as medicine (antiviral drugs, molecular probes for several types of imaging and drug carriers), electronic industry (OLEDs, semiconductors and nanodevices) and materials-related industry (nanoscale catalysts, water purification and improved or tunable bulk material properties). The origin of such versatility come from key properties that are common to all materials in the nanoscale. The large surface-to-volume ratio of nanomaterials makes them perfect for composite materials, catalysis, reactive systems, and chemical energy storage. Manipulation of the size of the nanostructure will change bulk material properties without changing chemical composition

and the smaller size allows them to increase density of bulk materials (increase conductivity, reduced resistance, etc.)[11].

1.1.6 Lanthanide-based Nanomaterials

Lanthanide-based nanomaterials have found promising applications in therapy, bioimaging, sensing, lighting and displays[13,14]. The recent developments in nanoscience have allowed these materials to begin *in vivo* studies by taking advantages of their tunable size, morphology, and surface bio immobilization. These nanoparticles could develop to be standard platforms for bio applications through doping and surface functionalization[15].

Lanthanide-based nanoparticles have attracted increasing interest in different fields due to the luminescent properties of trivalent lanthanide ions which include large Stokes shifts (europium complexes in Starck et al. present an absorption maxima in the 340-350 nm range and emit light in the 610-620 nm creating a Stoke shift of 260-270 nm[16]), long luminescent lifetimes (Tb^{3+} complexes in Bui et al. present luminescence lifetimes around 0.8 ms in glycerol and 0.2 ms in methanol, while Eu^{3+} complexes present luminescent lifetimes around 1 ms and 0.9 ms in methanol and glycerol respectively[17]), narrow and monochromatic emission bands (Eu^{3+} complex in Leif et al. produces two emission bands at 590 nm and 620 nm with the later emission having a full-width at half maximum of 5.2 nm[18]), and reduced photobleaching (Tb^{3+} complexes in Lima et al. only show signs of photobleaching after 25 minutes of continuous irradiation[19]) making them suitable for potential bioimaging and analytical sensing (protons, anions, metal ions and biomolecules). However, the intensity of this emission is extremely low due to the LaPorte forbidden nature of *f-f* transitions[15,20].

To solve this problem, lanthanides are often coupled with chromophores that indirectly excite the lanthanide ions in a phenomenon known as the "antenna effect"[21–23]. In this process, after the antenna ligand (chromophore) has been excited to the singlet level through UV-visible radiation, the energy is transferred to the triplet level through a process called inter system crossing (ISC). Consequently, the energy is transferred from the antenna molecule to the lanthanide ion through a process called

intramolecular energy transfer (ET). Finally, the excited lanthanide ion relaxes through radiative and non-radiative means[15,20]. The emission wavelength that results from this process depends on the lanthanide metal ion but is independent of the structural and electronic properties of the antenna ligands since the 4f orbitals are not involved in metal-ligand bonding due to shielding effects by the filled 5s and 5p orbitals. Nd^{3+}, Yb^{3+}, Er^{3+}, Pr^{3+}, Sm^{3+}, Dy^{3+}, Ho^{3+}, and Tm^{3+} metal ions exhibit emission in the NIR region, Eu^{3+} emits red light, Tb^{3+} emits green light, Sm^{3+} emits orange light, Tm^{3+} emits blue light and Gd^{3+} emits in the ultraviolet region[24]. Because of the shielded nature of the 4f orbitals, once a metal ion is chosen the emission wavelength is fixed and efforts can be made to modify the ligand system to fine tune energy transfer processes or to optimize properties necessary for future applications (dispersibility in water or other solvents, cellular uptake, cellular specificity, sensitivity to pollutants in solution, etc.).

To date, the range of ligands used to enhance the luminescent quantum yield of lanthanide ions and specifically Eu^{3+} is very vast and diversified, ranging from relatively simple benzoic acid derivatives to larger hexadentate ligands as well as a combination of β-diketonate ligands and phenanthroline, bipyridine and phosphine oxide derivatives. In 2017, Kalyakina et al. synthesized 9 Eu^{3+} complexes using fluorobenzoic acid derivatives that had a vast range of luminescent quantum yields. The complexes had formulas of $Eu(L)_3(H_2O)$ and $Eu(L)_3(H_2O)_2$, and the highest luminescent quantum yield in this study (45%) was achieved using 2,3,4,5-tetrafluorobenzoic acid[25] (Figure 1a). In 2016, Costa et al. synthesized highly luminescent metal-organic framework (MOF) microcrystals using trimesic acid (Figure 1b) as a ligand and a laser ablation technique. The MOF had a formula of $EuL(H_2O)_4$ and a luminescent quantum yield of 40%[26]. More complex ligands with more conjugated rings have also been studied, and an example is the Eu^{3+} complexes synthesized in 2020 by Hasegawa et al. In his work, europium is complexed with S and R variants of 2-([(*E*)-2,2'-bipyridin-6-ylmethylidene]amino)propenamide (Figure 1c) (L^{val}) and 1,2-{di[(*E*)-2,2'-bipyridin-6-ylmethylidene]amino}propane (Figure 1d) (L^{me}). The complexes had a formula of $EuL(NO_2)_3$ and presented different luminescent quantum yields. The S and R forms of the Eu-L^{val} complex had luminescent quantum yields of 44.5% and 44.8%[27], respectively. The Eu- L^{me} complex was reported to have a luminescent quantum yield of 18.9% in its S form and 16.0% in

its R form[27]. In 2019, Ogata et al. synthesized europium complexes with N^1,N^2-di([2,2'-bipyridin]-5-yl)ethane-1,2-diamine derivatives. The initial complex with an unmodified ligand (Figure 1e) presents a formula EuL and had a luminescent quantum yield of 14.8%[28]. The modified ligand had acyl groups of varying length. The complexes with modified ligands (Figure 1f) had formulas of $Eu_2L_3(NO_2)_6$ and presented increase luminescent quantum yields of 33.5%, 51.1%, 38.7%, 55.0%, 54.8% and 50.3%[28] for 8C, 12C, 13C, 14C, 18C and 22C acyl chains, respectively. In 2016 Starck et al. studied europium complexes triazacyclononane triscarboxylate and phosphinate ligands (Figure 1g). These complexes had formula EuL^{3-} and the highest luminescent quantum yield achieved was 34% in water and 76% in methanol[16]. Finally, many complexes have been created that combine two or more ligands to improve the luminescent quantum yield of Eu^{3+} complexes. An example is Lima et al, which in 2013 combined 2-thenoyltrifluoroacetone (TTA) and 1,1'-(sulfinyldimethanediyl)dibenzene (DBSO) (Figure 1h) to obtain a complex with formula $Eu(TTA)_3(DBSO)_2$ which has an impressive luminescent quantum yield of 85%[29].

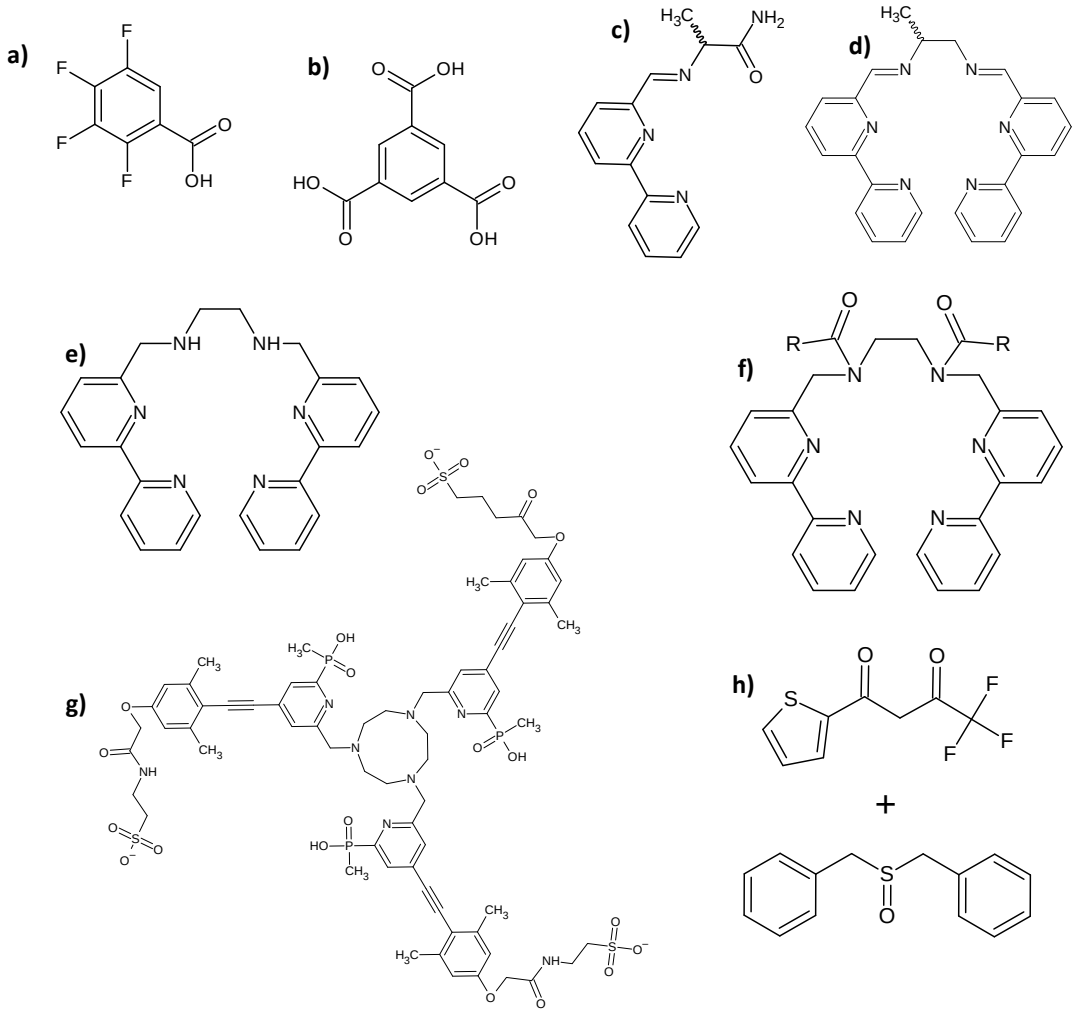

Figure 1. 2D structures of previously utilized ligands for Eu^{3+} complexes.

Previous studies on surface functionalization of lanthanide-based nanoparticles have shown extremely interesting results. Li et al. were able to perform a coating exchange on 18% Yb^{3+}/2% Er^{3+}:$NaYF_4$ upconverting nanoparticles (UCNPs) using a biomimetic PEGylated phospholipid to replace oleic acid. The coating exchange allowed for biocompatible and water-soluble nanoparticles without affecting the up-conversion process. Subsequently, folate was added to the PEGylated phospholipid coating to explore the use of these Lipo-UCNPs as targeted imaging for cancer cells. HeLa cells exposed to folate Lipo-UCNPs showed green luminescent spots throughout the cytoplasm, therefore indicating internalization of nanoparticles into the cell[30]. Liu et al. showed that by functionalizing the surface of

Er:CaF_2 nanoparticles with fluorescein isothiocyanate they were able to bypass the forbidden *f-f* transitions using the antenna effect to produce a 28-fold increase in the Er^{3+} based near infrared (NIR) emission[31].

Calcium fluoride presents numerous advantages to lanthanide-doping. Calcium ions have a similar atomic radius to most lanthanide ions allowing the CaF_2 to retain its crystal structure even with doping percentages as high as 35 %[32]. CaF_2 is known to be transparent in the UV-visible-NIR range and is commonly used in applications where far-UV transparency is required[33]. At the same time, CaF_2 and lanthanide-doped CaF_2 present high biocompatibility and low cytotoxicity[34]. In the past, many synthetic methods have been developed to synthesize CaF_2 nanoparticles. In 2010, Pandurangappa et al. synthesized CaF_2 nanocrystals through a hydrothermal method and co-precipitation method. For the hydrothermal method, a solution of $CaCl_2$ and NH_4F were mixed in a 30 mL autoclave and subsequently heated to a temperature of 160°C for 24 hrs in an oven. For the co-precipitation method, the same two solutions were added to a 100 mL Erlenmeyer flask and stirred for 2 hrs. Both reactions produced crystalline CaF_2 nanoparticles with powder x-ray diffraction (XRD) pattern consistent with face centered cubic geometry[35]. The size of the nanoparticles were 20-28 nm and 30-35 nm for hydrothermal and co-precipitation methods, respectively[35]. In 2006, Labéguerie et al. synthesized CaF_2 nanoparticles using non-aqueous nanoreactors. In this synthesis method, a solution of $Ca(NO_3)_2$ in isopropanol and anhydrous HF in isopropanol are added to two separate solutions of polystyrene in THF. Due to polystyrene being soluble only in THF and not isopropyl alcohol, the two solutions are immiscible and therefore undergo homogenization. During homogenization, isopropanol nanodroplets form and act as nanoreactors. After, the $Ca(NO_3)_2$ and HF homogenized solution are slowly poured together and stirred for 10 to 120 minutes[36]. When the two solutions are mixed, inter-nanoreactor exchanges occur allowing F^- anions and metal cations to react with each other and form nanoparticles. The XRD patterns of the nanoparticles are consistent with the face centered cubic geometry and TEM imaging revealed a cubic morphology. The size for nanoparticles stirred for 10 min, 30 min and 120 min was reported to be 13, 15 and 14 nm[36], respectively. Eu^{3+}:CaF_2 nanoparticles were also synthesized using the same method and TEM revealed a

spherical morphology and an average size of 11 nm[36]. In 2016, Kuzmanoski et al. synthesize a variety of doped CaF_2 nanoparticles by utilizing a microwave-assisted synthesis in ionic liquids under an argon atmosphere. $CaCl_2$ and other metal chlorides were dissolved in ethanol, while the fluoride source $[OMIm][BF_4]$ (OMIm: octylmethylimidazoliyum) was dissolved in the ionic liquid $[Bu_3MeN][N(SO_2CF_3)_2]$ (BU_3MeN: tributylmethylammonium). In a microwave reactor, the ionic liquid solution was heated to 100°C and then the metal chloride solution was added under high stirring. The ethanol was evaporated off and the solution was heated to 200°C for 20 minutes. Based on DLS measurements, the synthesized nanoparticles range from 20-30 nm up to 50-70 nm depending on the doping metal[37]. All nanoparticles show XRD patterns consistent with the face centered cubic geometry of CaF_2[37].

1.2 Project Design

1.2.1 Computational Studies

As previously stated, europium complexes have very appealing luminescent properties that makes them extremely viable candidates in OLEDs, biomedical sensing, and other sensory devices. The mechanisms behind their properties have been studied in large detail but the field is lacking the knowledge to guide the selection of ligands that yield highly efficient complexes. To increase the knowledge in this field it is important to understand the role and effects that the electronic structure of the ligand has on the system. To do so, we computationally studied the electronic properties of europium complexes synthetized and experimentally studied by Kalyakina et al. The ligands in the complexes are 1-fluorobenzoate derivatives and differ in the number, position, and nature of the substituents. The chemical structure of the ligands is shown in Figure 2. The complexes show a range of luminescent quantum yield (QY) values that span from 0% to 45%[25]. $Eu(TTA)_3(H_2O)_2$ [38] (QY = 23%[39,40]) was also modeled to compare the benzoate and β-diketonate systems as well as to study the system that will be used to enhance the luminescent quantum yield of the nanoparticles. The electronic properties of the complexes were calculated using Gaussian 09[41] suite. Density functional theory (DFT) was used to -minimize the molecular structures and

time-dependent density functional theory (TD-DFT) was used to calculate the singlet and triplet energy levels of the complexes. Treatment of 4f electrons still provides challenges and limitations in lanthanide-ligand systems. However, 4*f* electrons are not involved in metal-ligand bonding. Furthermore, it has been shown in the past that the use of large core relativistic effective core potentials (RECPs) for the lanthanide atoms can provide sufficient accuracy in computational results for the lanthanide-ligand systems with simplified computational efforts[42–45].

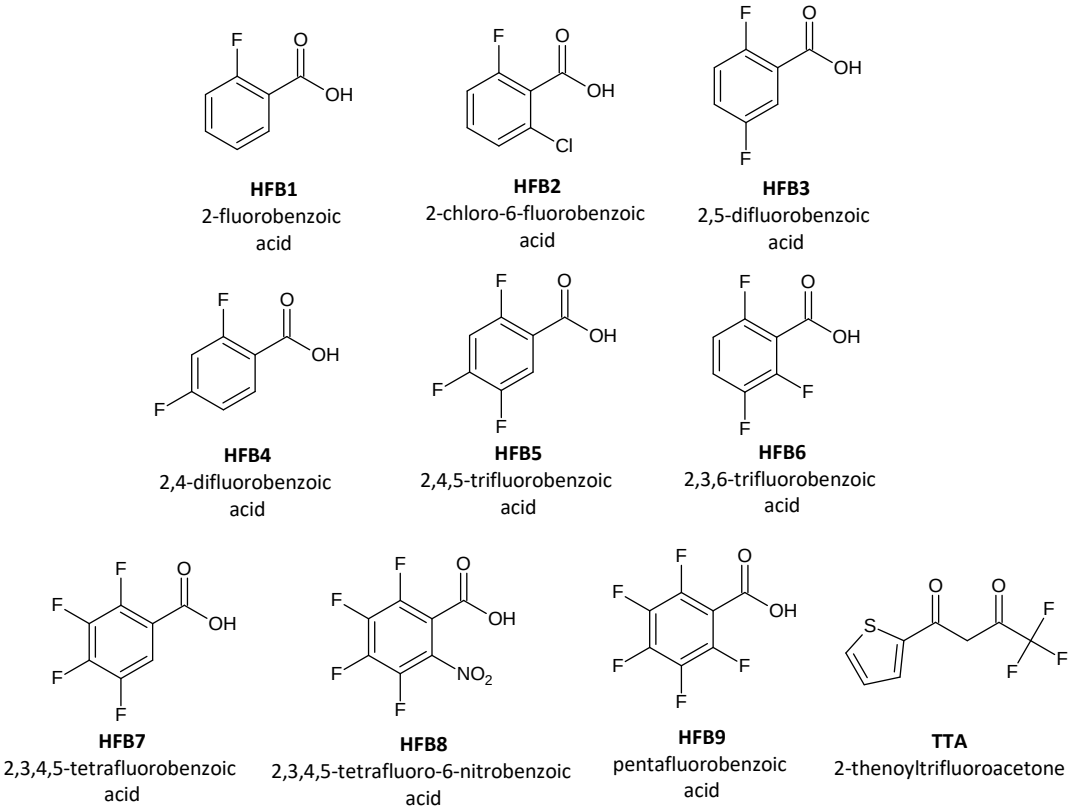

Figure 2. Structure of studied ligands used in computational studies.

1.2.2 Synthesis of Eu^{3+}-doped CaF_2 nanoparticles

This synthetic method uses a microwave-assisted co-precipitation method. To overcome the high formation constant of CaF_2, thermal decomposition of a Ca^{2+} and Eu^{3+} complexes and the use of $NaBF_4$ as a source of F^- would provide appropriate control of the reaction. Ethylenediaminetetraacetate disodium salt (Na_2EDTA), shown in Figure 3, was used as a chelating agent for Ca^{2+} and Eu^{3+} ions because of its

known chelating affinity to divalent and trivalent metal ions. This allows the formation of EDTA complexes that slowly release the metal ions under aqueous refluxing conditions[46].

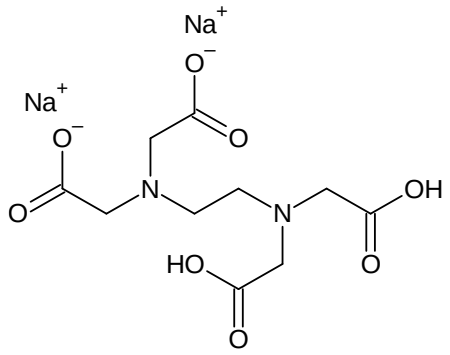

Figure 3. Structure of Ethylenediaminetetraacetic acid disodium salt (Na_2EDTA)

Lin Ma et al. theorized that microwave radiation, which can create a homogenous heating gradient compared to a traditional heating method would cause a controlled release of Ca^{2+} and Eu^{3+} ions into the solution through the decomposition of metal EDTA complexes producing homogeneous products and providing an easily scalable nano-synthetic method[46]. The size of the nanoparticles can be accurately tuned by controlling the concentration of the reactants and the solution pH[32]. Based on previous studies, an initial metal chloride concentration of 0.056M and a solution pH of 6 were chosen to obtain monodispersed crystalline nanoparticles with an approximate size of 200 nm[32]. A 10% europium doping was chosen to minimize self-quenching of the lanthanide ions while still providing reasonable luminescent quantum yields when compared to other doping percentages. The net ionic equation for this reaction is shown in Figure 4.

$$0.9\,Ca^{2+}_{(aq)} + 0.1\,Eu^{3+}_{(aq)} + EDTA^{4-}_{(aq)} + F^{-}_{(aq)} \xrightarrow[pH = 6]{\text{reflux: } 100^{o},\ 30\ \text{min}} Eu{:}CaF_{2\,(s)}$$

Figure 4. Net ionic equation for the formation of Eu^{3+}-doped CaF_2 nanoparticles.

1.2.3 Surface Coating

Because of using excess EDTA as a chelating agent in the synthesis for the controlled release of metal cations, the nanoparticles obtained are coated with EDTA. Thus, the produced nanoparticles are monodispersed and water soluble. However, EDTA does not help to enhance the luminescent quantum yield of the nanoparticles. To increase the luminescent quantum yield, the nanoparticles are coated with 2-thenoyltrifluoroacetone (TTA) shown in Figure 5. This ligand was chosen because it has previously been used in europium complexes with high luminescent quantum yields[39,40]. The surface modification reaction was conducted in water and TTA was solubilized by deprotonating using triethylamine as shown in Figure 6a. The deprotonation is used to create β-diketonate anions that have affinity for lanthanide ions and easily form complexes as seen in Figure 6b. To maximize the luminescent quantum yield, different NPs-to-TTA mass ratios (1-1, 1-5, 1-10, 1-25, 1-50, 1-75, 1-100) were explored during the surface modification process. Three different sizes of nanoparticles (470, 150-170 and 94 nm) were coated with TTA to test the effects of size on the quantum yield. Nanoparticles with a size of 94 nm were also coated with PEG8000 to improve the water dispersibility.

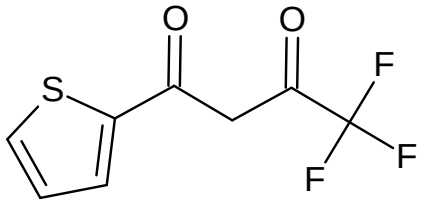

Figure 5. Chemical structure of 2-thenoyltrifluoroacetone (TTA).

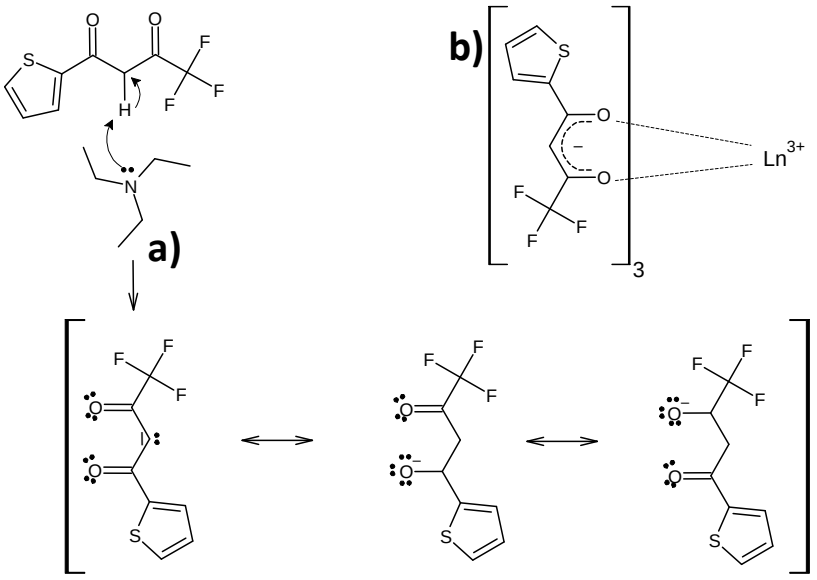

Figure 6. a) Deprotonation mechanism of TTA by triethylamine. b) β-diketonate TTA ion binding to trivalent lanthanide ions.

CHAPTER TWO: EXPERIMENTAL

2.1 Computational Studies

The Gaussian 09 computational chemistry package[41] was used to carry out the density functional theory (DFT) calculations of the lanthanide complexes. The B3LYP exchange correlation functional[47] was used for all calculations. The geometry optimization was conducted with no geometry constraints. The optimized geometries were then subjected to frequency calculations to confirm that the optimized molecular structures were the minimum energy point. The singlet and triplet electronic energy levels of the complexes at the ground state optimized geometries were calculated using TD-DFT calculations.

The synthesis, purification, characterization, and experimental luminescent studies of the Eu^{3+} complexes were reported elsewhere[25,38]. All complexes were modeled following the crystal structures reported in their respective papers. Complexes from Kalyakina et al. with ligands FB1, FB3-FB5, FB7 and FB8 were modeled as dihydrate complexes and complexes with ligands FB2, FB6 and FB9 were modeled as monohydrate complexes. To further explore the effects of coordinated waters on the singlet and triplet states, the complexes with ligand FB2, FB6 and FB9 were also modeled as dihydrate complexes. To explore how the position of fluorine on the benzoic acid ring affects the electronic energy levels of the complexes, the FB1 complex was modeled using the 2 ortho, 2 meta and 1 para variants. The $Eu(TTA)_3(H_2O)_2$ complex was modeled using the structure reported by Vallet et al. In Eu-ligand systems, *f*-orbitals do not significantly participate in metal-ligand bonding[48]. For this study, the Stuttgart-Dresden quasi-relativistic effective large core potentials (ECP) and the optimized [7s6p5d][5s4p3d]-GTO valence basis set were used[49,50] for the europium metal center. For H, C, N, O, F, S and Cl atoms the 6-31g(d) and 6-311+g(d,p) basis sets were used[51,52]. All molecular orbitals shapes were created with the default isovalue (0.02) in Gaussian 09. Isovalues describe how far from the nucleus the constructed surface will be (large isovalues = closer to nucleus, smaller isovalues = further from nucleus).

2.2 Experimental Details

2.2.1 Materials

All chemicals and reagents were used as obtained without further purification. The water used in the experiments was ultrapure (18.2 Ω) grade. All glassware was washed with 2M nitric acid and 10g/L Alconox solution and then followed by a rinse with ultrapure water. The pH measurements were taken using the Vernier pH probe connected to a computer via the GoLink USB adaptor and the Logger Pro 3 software provided by Vernier. Sonication was performed using a Fischer Scientific FS-140H ultrasonic cleaner. All centrifuge tubes were made of polyethylene and produced by Falcon®. Centrifugation of 15 mL tubes was done using a Fischer Scientific accuSpin 8C Clinical Centrifuge, while centrifugation of 50 mL tubes was done using a ThermoScientific Sorvall Lynx 4000 Centrifuge with a ThermoScientific BIOFlex HC rotor. A Fisher Scientific Standard Vortex Mixer was utilized to agitate nanoparticle suspensions. For nanoparticle imaging, Formvar carbon films on 200-mesh copper grids from Electron Microscopy Sciences were used. Reagents are as follows: anhydrous calcium chloride ($CaCl_2$, 99.6%, Fischer Scientific), disodium ethylenediamine tetraacetate ($Na_2C_{10}H_{14}O_8N_2 \cdot 2H_2O$, 95% , Fischer Scientific), sodium tetrafluoroborate ($NaBF_4$, 95% , Alfa Aesar), europium (III) chloride hexahydrate ($EuCl_3 \cdot 6H_2O$, 99.9% , Acros Organics), 2-thenoyltrifluoroacetone (TTA, $C_8H_5F_3O_2S$, 99%, Acros Organics), triethylamine (TEA, $C_6H_{15}N$, Mallinckrodt), acetonitrile (C_2H_3N, HPLC grade, Fischer Scientific), dichloromethane (CH_2Cl_2, certified ACS, Fisher Scientific).

2.2.2 Microwave Synthesis of Europium-Doped Calcium Fluoride Nanoparticles

In small scale reactions (maximum volume of 100 mL), a CEM Discover 300W microwave reactor (Figure 7a) was used. The reactor was operated using Synergy software. For larger scale reactions with volumes of 300 mL, a CEM Mars 6 was used (Figure 7b and c).

For small scale synthesis, $CaCl_2$ (0.58 g, 5.23 mmol, 10 eq.), $EuCl_3 \cdot 6H_2O$ (0.19 g, 0.52 mmol, 1 eq.) and EDTA (2.97 g, 7.98 mmol, 15 eq.) were dissolved in 55 mL of ultrapure water and the solution was adjusted to a pH of 6 using 4 M NaOH solution. A second solution containing 1.23 g of $NaBF_4$ (1.23

g, 11.20 mmol, 22 eq.) was dissolved in 20 mL of ultrapure water and then added dropwise to the metal chloride solution. The pH was readjusted to 6 using 4 M NaOH. The reaction was added to a 100 mL round bottom flask with a stir bar. The round bottom flask containing the reaction mixture was moved to the CEM Discover 300W microwave reactor with a fractioning column and a water condenser with ice cold water. The reaction mixture was refluxed at 100°C for 30 minutes using a microwave reactor. To do that, the reaction cycle was set to 100°C and 100W, with a ramp time of 5 minutes, a holding time of 30 minutes and a safe temperature of 120°C.

For large scale reactions, the reaction was performed at a 3x scale. $CaCl_2$ (1.74 g, 15.68 mmol, 9 eq.), 0.57 g $EuCl_3 \cdot 6H_2O$ (0.57 g, 1.72 mmol, 1 eq.) and 8.91 g of EDTA (8.91 g, 23.94 mmol, 14 eq.) were dissolved in 165 mL of ultrapure water and the solution was adjusted to a pH of 6 using 4 M NaOH solution. A second solution containing 3.69 g of $NaBF_4$ (3.69 g, 33.61 mmol, 20 eq.) was dissolved in 60 mL of ultrapure water and then added dropwise to the metal chloride solution. The pH was readjusted to 6 using 4 M NaOH. The solution and a medium stir bar were added to a 300 mL round bottom flask with two necks. The round bottom flask containing the reaction mixture was moved to the CEM Mars 6 microwave reactor with a fractioning column and a water condenser with ice cold water. The reaction mixture was refluxed at 100°C for 30 minutes by setting the reaction cycle at 100°C and 800W, with a ramp time of 5 minutes, a holding time of 30 minutes.

For both scales, after the reaction was completed the content of the round bottom flask was moved to 50 mL falcon tubes and centrifuged at 4500 rpm for 3 hours. After centrifugation, the supernatant was discarded, and the pellet was resuspended in ultrapure water. The centrifugation was repeated two more times. After the last centrifugation, the pellet was suspended in 2 mL of ethanol and transferred to a scintillation vial. A Kimwipe was left at the top of the scintillation and the ethanol was allowed to evaporate overnight. The dried nanoparticles were stored away from light.

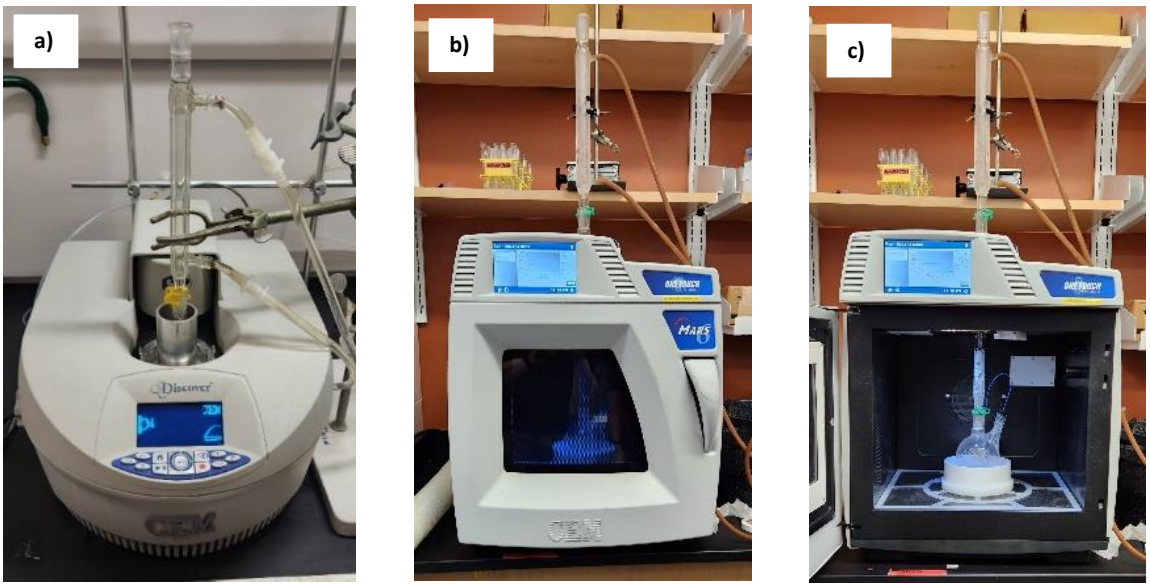

Figure 7. Reaction set up for a) small scale reactions using the CEM Discover 300W and b, and c) large scale reactions using the CEM Mars 6 microwave reactor.

2.2.2 Microwave Synthesis of Fluoride Nanoparticles

$CaCl_2$ (0.62 g, 5.6 mmol, 10 eq.), and EDTA (2.97 g, 7.98 mmol, 1.4 eq.) were dissolved in 55 mL of ultrapure water and the solution was adjusted to a pH of 6 using 4 M NaOH solution. A second solution containing 1.23 g of $NaBF_4$ (1.23 g, 11.20 mmol, 2 eq.) was dissolved in 20 mL of ultrapure water and then added dropwise to the metal chloride solution. The pH was readjusted to 6 using 4 M NaOH. The reaction was added to a 100 mL round bottom flask with a stir bar. The round bottom flask containing the reaction mixture was moved to the CEM Discover 300W microwave reactor with a fractioning column and a water condenser with ice cold water. The reaction mixture was refluxed at 100°C for 30 minutes using a microwave reactor. To do that, the reaction cycle was set to 100°C and 100W, with a ramp time of 5 minutes, a holding time of 30 minutes and a safe temperature of 120°C. After the reaction was completed the content of the round bottom flask was moved to 50 mL falcon tubes and centrifuged at 4500 rpm for 3 hours. After centrifugation, the supernatant was discarded, and the pellet was resuspended in ultrapure water. The centrifugation was repeated two more times. After the last centrifugation, the pellet was suspended in 2 mL of ethanol and transferred to a scintillation vial. A

Kimwipe was left at the top of the scintillation and the ethanol was allowed to evaporate overnight. The dried nanoparticles were stored away from light.

2.2.3 Surface Functionalization Reaction of Doped Nanoparticles using TTA

In a 15 mL falcon tube, 10 mg of nanoparticles and 10 mL of ultrapure water were added. The nanoparticles were suspended using a sonic bath. For all coating ratios, nanoparticles from the same batch were used to eliminate differences that could arise between particles of different batches. Depending on the coating ratio, different amounts of TTA were added (Table 1) and the solution was sonicated again. The appropriate quantity of triethylamine (TEA) (Table 1) for the desired coating ratio was added and the reaction was shaken by hand for 1 minute and then agitated for 2 hours using a vortexer. Finally, the reaction solution was centrifuged. Rotation speed and time are dependent on nanoparticle sizes. For nanoparticles bigger than 100 nm, the samples were spun at 4900 rpm for 100 min, while nanoparticles smaller than 100 nm were centrifuged at 5500 rpm for 90 minutes. After centrifugation, the supernatant was discarded, and the pellet was resuspended in 10 mL of ethanol. The centrifugation was repeated two more times. After the last centrifugation, the pellet was suspended in 2 mL of ethanol and transferred to a scintillation vial. A Kimwipe was added to the top of the scintillation vial and the ethanol was left to evaporate overnight. The TTA coated nanoparticles were stored away from light.

Table 1. Quantities of Eu:CaF_2 nanoparticles, TTA and TEA used to conduct the coating exchange reactions.

Ratios	Mass of NPs (mg)	Mass of TTA (mg)	Volume of TEA (µL)
1:1	10	10	30
1:5	10	50	150
1:10	10	100	300
1:25	10	250	750
1:50	10	500	1500
1:75	10	750	2250
1:100	10	1000	3000

2.2.4 Surface Functionalization Reaction of Doped Nanoparticles using TTA and PEG8000

In a 15 mL falcon tube, 10 mg of nanoparticles and 10 mL of ultrapure water were added. The nanoparticles were suspended using a sonic bath. After, 500 mg of TTA and 5 mg of PEG8000 were added, the solution was sonicated again for 30 seconds, and 1.5 mL of TEA was added. The reaction was shaken by hand for 1 minute and then agitated for 2 hours using a vortexer. Subsequently, the reaction solution was centrifuged at 5500 rpm for 90 min three times. After each centrifugation, the supernatant was discarded, and the pellet was resuspended in 10 mL of ethanol. After the last centrifugation, the pellet was suspended in 2 mL of ethanol and transferred to a scintillation vial. A Kimwipe was added to the top of the scintillation vial and the ethanol was left to evaporate overnight. The TTA coated nanoparticles were stored away from light.

2.3 Characterization

2.3.1 Powder X-ray Diffraction Studies

Powder X-ray diffraction (P-XRD) studies were carried out to determine the identity of the nanoparticles. A Rigaku Miniflex XRD instrument with Cokα source was used with the Jade 7 software. The sample was prepared by suspending the nanoparticles in 2 mL of acetone and slowly applying them on to an XRD plate using a plastic pipette. The plate was left to dry in a fume hood. The process was repeated until an even white layer of nanoparticles was formed. The product was scanned from 15° to 75° at a rate of 2° per minute and a sampling width of 0.05°. The voltage was set to 30 kV and current was set to 15 mA. The scattering slit was set to 4.2° and the receiving slit was set to 0.3 mm. Jade 7 software was used to correct the data from cobalt to copper X-ray source.

The Scherrer equation was used to calculate the crystallite size of the nanoparticles:

$$D = \frac{k\lambda}{\beta cos\theta} \quad (1)$$

where D is the average crystallite size, *k* is the shape factor (0.94 for semispherical particles), λ is the wavelength of the X-rays (1.5406 Å for X-ray Cukα), β is the full width at half maximum (FWHM, in radians) of a chosen peak, and θ is the incident angle (in degrees) of the chosen peak[53].

2.3.2 Dynamic Light Scattering

Dynamic light scattering (DLS) was used to obtain an approximate size distribution of the nanoparticles dispersed in water. A Malvern Zetasizer instrument was used to perform light scattering measurements of the nanoparticle suspensions. The sample was prepared by suspending 4 mg of the product in 3 mL of ultrapure water in a 10 mm disposable plastic cuvette. The measurement was taken with the following parameters: measurement temperature was set at 25°C with an equilibration time of 2 minutes; the refractive index of calcium fluoride was set to 1.433 and the absorption to 0.100; the viscosity of water was set to 0.8872 and the refractive index was set to 1.330; the dispersant viscosity was set as the sample viscosity. Only nanoparticles with a PdI lower than 0.25 and a main peak area of at least 95% were selected for the surface coating (ligand exchange) reactions.

2.3.3 Scanning Electron Microscopy and Energy Dispersive X-ray Spectroscopy

Scanning Electron Microscopy (SEM) was carried out to obtain information about size and morphology of the nanoparticles. Energy Dispersive X-ray Spectroscopy (EDS) studies were carried out to obtain a qualitative elemental analysis. SEM/EDX images courtesy of Joseph Favata (Zeiss Group) who acquired the images as part of a product demo. A ZEISS GeminiSEM 300 with a STEM, In-Lens and Oxford Instruments EDS detector was used for these measurements. The sample was prepared by suspending the nanoparticles in acetone and by adding 10 µL of the suspension to a TEM grid. The grid was then left to dry for 5 minutes. For SEM, the samples were investigated utilizing both transmission mode and surface topography. For transmission mode, the operating voltage was set to 30 kV, with a working distance (WD) of 1.9 mm, and a magnification of 200,000x. For surface tomography, the operating voltage was set to 0.8 kV, a working distance of 1.6mm and a magnification of 200,000x. Images were taken using both

bright-field (BF) and oriented dark-field (ODF) modes. The EDS measurements were taken using EDS scanning while specifically selecting for Ca (kα1), Eu (Lα1) and F (kα1,2) X-ray emissions.

2.3.4 Fourier-Transform Infrared Spectroscopy

Fourier-Transform Infrared (FT-IR) measurements were used to analyze the surface coating of the nanoparticles. A ThermoScientific Nicolet iS10 spectrometer was used with an ATR attachment to take the measurements. The instrument was set to measure the background before each sample, and it was set to perform 32 scans with a 4 cm^{-1} resolution from 4000 cm^{-1} to 500 cm^{-1}. All infrared spectra were baseline adjusted by setting the absorbance at 1774 cm^{-1} to zero.

2.3.5 UV-Vis Absorption Spectroscopy

UV-Vis absorption spectroscopy was used to determine the maximum absorption wavelength of the TTA-coated Eu^{3+}-doped CaF_2 nanoparticles. An Agilent Cary Series UV-Vis-NIR spectrophotometer in double beam mode was used to collect the spectra. The light source was allowed to warm up for 45 minutes before taking the measurements and a zero and baseline correction was applied to the data. The samples were prepared by suspending 50 mg of nanoparticles in 3mL of HPLC-grade acetonitrile in a glass scintillation vial followed by sonication. 1.5 mL of suspended nanoparticles in acetonitrile was moved into a 3mL quartz cuvette (path lengths = 1cm). The sample was consequently diluted until the absorbance at 341 nm was between 0.2 and 0.6. In a separate quartz cuvette, 3 mL of HPLC-grade acetonitrile was used as a blank. The samples were scanned between 800 and 200 nm at a data interval of 1 nm and 600 nm/min and the measurements were carried out in triplicates.

2.3.6 Emission Spectroscopy

The emission spectra of the nanoparticles coated with TTA were collected to compare the emission patterns of other Eu^{3+} complexes. The luminescent spectra of the nanoparticles coated with increasing ratios of TTA were collected to study the change in the luminescent quantum yield. A Perking Elmer LS

55 Luminescence Spectrometer was used to collect the spectra. The light source was allowed to warm up for 45 minutes before the samples were analyzed. The samples were prepared the same way as those prepared for the UV-Vis absorption spectroscopy with the exception that a 4-sided quarts cuvette was used. The samples were excited at 341 nm with a scan rate of 100 nm/min, an excitation slit of 5.0 nm and an emission slit of 5 nm. The emission data was collected from 500 to 800 nm with triplicate measurements.

2.3.7 Luminescent Quantum Yield Calculations

To calculate the luminescent quantum yield of the TTA-coated nanoparticles, absorption and emission spectra were taken using the procedures described above. Between each measurement, the samples were resuspended using a plastic pipette. The luminescence spectrum was fit at wavelengths 503, 528, 565 and 640 nm to a cubic function using a non-linear least squares regression. This cubic function was then subtracted from the whole luminescence spectrum. The baselines obtained with this method for the uncoated nanoparticles, 1-5 and 1-75 coated nanoparticles are shown in Figure 8. The area under the curve from 500 to 640 nm was determined by numerical integration via trapezoid rule[54]. Due to the difficulty in precisely measuring the number of photons emitted and absorbed, a comparative method was used to calculate the luminescent quantum yield:

$$\phi_s = \frac{{n_r}^2}{{n_s}^2}\frac{A_r}{A_s}\frac{I_s}{I_r}\phi_r \quad (2)$$

Here Φ, *n*, *A* and *I* denote the luminescent quantum yield, the refractive index of the solvents, the area under the curve in the emission spectrum, and the absorbance at the excitation wavelength, respectively. The subscript "r" indicates the reference substance, while the subscript "s" stands for the unknown sample[55]. The reference sample was prepared by dissolving 5 mg of $Eu(TTA)_3(H_2O)_2$ in 3 mL of DCM which has a refractive index of 1.4211[56]. The solution was then moved to a 4-sided quartz cuvette and the solution was diluted until the absorbance at 341 nm was between 0.2 and 0.6. The complex in DCM has a

luminescent quantum yield of 23%[39,40]. The solvent used for the nanoparticles was acetonitrile which has a refractive index of 1.34163[57].

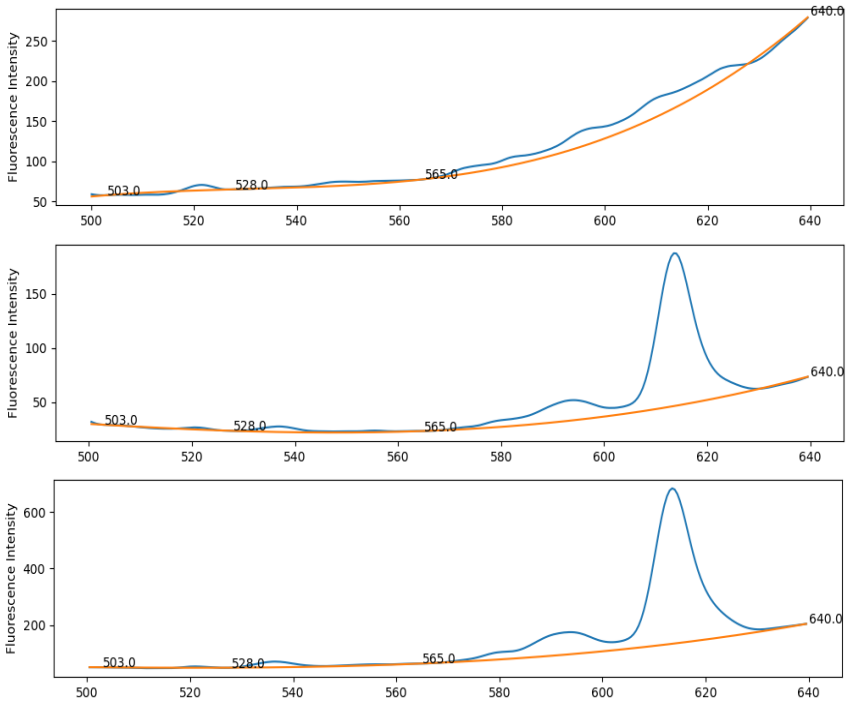

Figure 8. Fit of the baseline of the emission spectra of uncoated nanoparticles (top), 1-5 TTA coated nanoparticles (middle) and 1-75 TTA coated nanoparticles (bottom) obtained using non-linear least squares regression.

2.3.8 Epifluorescent Imaging

To obtain epifluorescent images, the EVOS epifluorescent microscope was used with a custom excitation source centered at 365 nm. Images were taken at a 20x magnification. The samples were prepared by suspending 5 mg of nanoparticles in 500 µL of deionized water and briefly vortexed, then sonicated for 20 seconds. 5 µL of the samples were spotted on an ethanol cleaned glass coverslip. The nanoparticles were allowed to dry before the cover slip was mounted with vectashield to the microscope. All pictures were pseudo colored to better visualize the particles.

CHAPTER THREE: RESULTS AND DISCUSSION

3.1 Computational Studies

3.1.1 Structural Properties

The DFT-optimized molecular structures of the lanthanide complexes synthesized by Kalyakina et al. and Vallet et al. are shown in Figure 10 and Figure A1. To compare the structural parameters calculated using the two basis sets (6-31g(d) and 6-311+G(d,p)) used in this study, DFT-optimized geometries were compared to the experimental single crystal X-ray data presented by Kalyakina et al. and Vallet et al. in their publications (Table **2**). From this point onward, the complexes will be referred to as EuL where L is the ligand of interest. The bonds were assigned using the numbering shown in Figure 9.

The coordination spheres of the DFT-optimized structures are very similar to the structures previously reported using single crystal X-ray diffraction studies. The Eu^{3+} metal ion is coordinated by six oxygen atoms (from three benzoic acid derivatives or TTA ligands) and one or two water molecules. The coordination number of Eu^{3+} ion is either seven or eight depending on the number of coordinated water molecules. The coordination sphere can be explained as a distorted square antiprism.

DFT-optimized Eu-O bond lengths are on average 0.021 Å shorter than experimental values when calculated using the 6-31G(d) basis set and 0.031 Å shorter when calculated with the 6-311+G(d,p) basis set. Specifically, Eu-ligand bonds are 0.013 Å and 0.029 Å shorter for 6-31+G(d) and 6-311+G(d,p) respectively while Eu-water bonds are 0.063 Å shorter for 6-31G(d) and 0.056 Å shorter in 6-311+G(d,p). Both basis sets produced values that agree with a certain degree of error to the experimental values. In complex EuFB1 the Eu-O bond lengths calculated using the 6-31G(d) basis set more closely agrees to experimental values for bonds Eu-$O_{1/3}$ and Eu-O_8, but for the other bonds (Eu-$O_{5/7}$), the 6-311+G(d,p) basis set better agrees with experimental values. For the EuFB2 complex, 6-31G(d) agrees with experimental values for bonds Eu-O_2 and Eu-O_4, but 6-311+G(d,p) produces bond lengths closer to experimental bond lengths for all other bonds. For complex EuFB3, 6-31G(d) strongly agrees with

experimental values only for bond Eu-O_7, but for bonds Eu-$O_{1/5}$ and Eu-O_8 the 6-311G+(d,p) basis set agrees more closely with experimental values. No discerning patterns can be identified in the Eu-O bonds of the studied complexes (Table ***2***). The EuTTA complex also shows no discerning pattern: the 6-31G(d) basis set is more accurate for Eu-O_1, Eu-O_2, Eu-O_4, Eu-O_5, Eu-O_7 and Eu-O_8, while 6-311+G(d,p) is more accurate for Eu-O_3 and Eu-O_6.

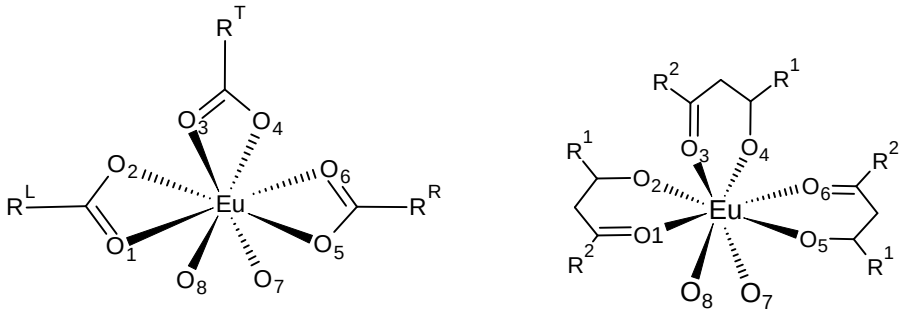

Figure 9. Numbering scheme of oxygen atoms used in fluorobenzoate complexes (left) and TTA complex (right). For the fluorobenzoate complexes, R^L, $R^{T,}$ and R^R are not used to distinguish between different ligand but are used to distinguish between the position of each ligand.

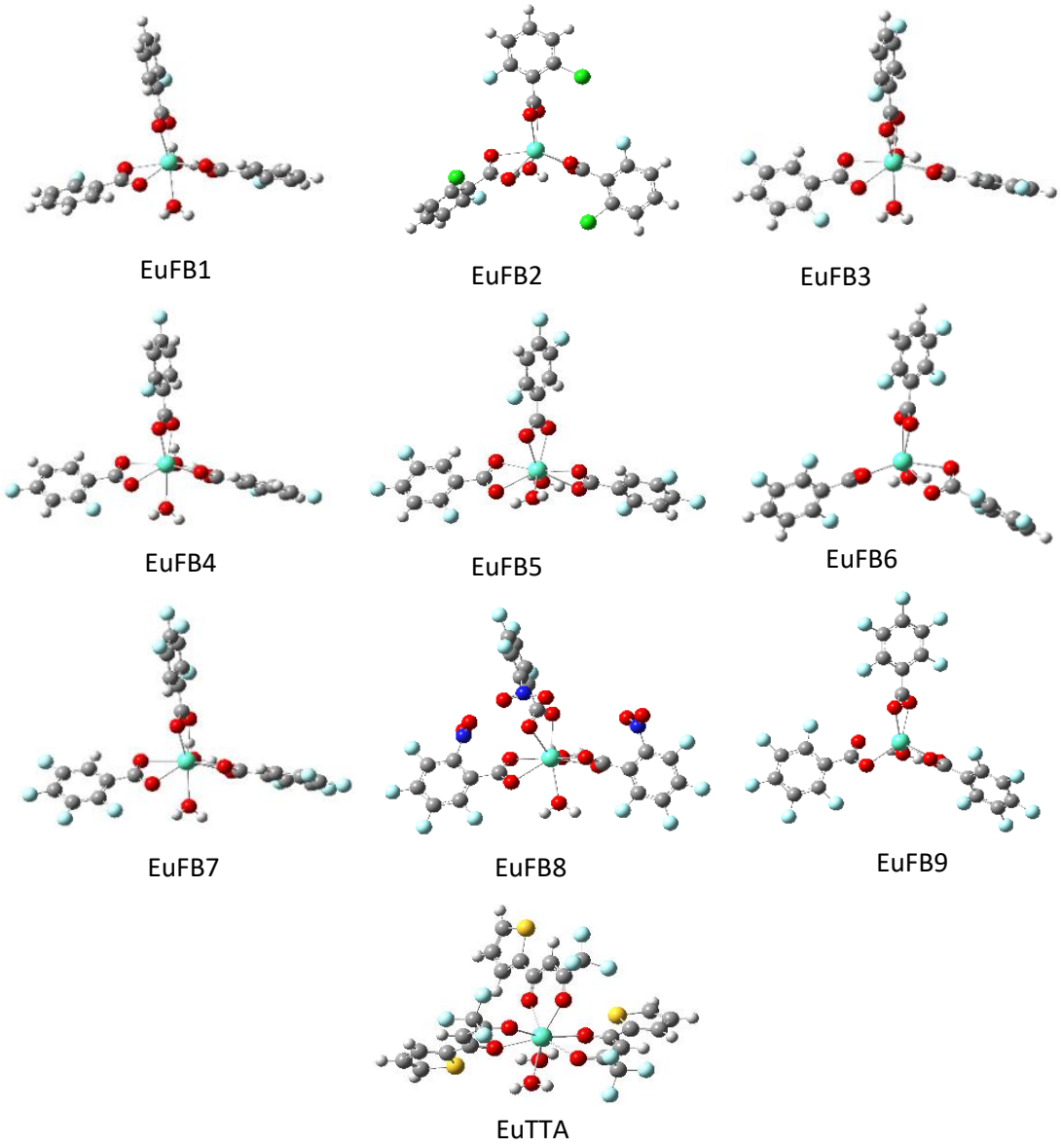

Figure 10. Optimized geometries obtained by DFT calculations using the 6-311+G(d,p) basis set of the studied compounds with structures reported in Kalyakina et al. and Vallet et al. In gray are the C atoms, in white are the H atoms, in red are the O atoms, in light blue are the F atoms, in dark blue are the N atoms, in green are the Cl atoms and in blue-green are the Eu atoms.

Table 2. Comparison between Eu-O experimental bond lengths and calculated bond lengths.

Complexes	Basis set	Eu-O_1 (Å)	Eu-O_2 (Å)	Eu-O_3 (Å)	Eu-O_4 (Å)	Eu-O_5 (Å)	Eu-O_6 (Å)	Eu-O_7 (Å)	Eu-O_8 (Å)
EuFB1	Exp	2.516	2.417	2.389	---	2.420	2.765	2.546	2.478
	6-31G(d)	2.49848	2.41944	2.38883	2.45107	2.50870	2.45725	2.50459	2.59030
	6-311+G(d,p)	2.47750	2.45278	2.43968	2.45001	2.45738	2.49823	2.52978	2.55421
EuFB2	Exp	---	2.321	2.479	2.479	2.321	---	2.476	2.476
	6-31G(d)	2.39338	2.44564	2.38094	2.45482	2.42810	2.43535	2.48056	---
	6-311+G(d,p)	2.43464	2.47634	2.42347	2.43128	2.44805	2.44864	2.47784	---
EuFB3	Exp	2.479	2.545	2.492	2.474	2.297	---	2.375	2.403
	6-31G(d)	2.44226	2.43994	2.41517	2.45581	2.46211	2.49244	2.51106	2.55192
	6-311+G(d,p)	2.46748	2.47752	2.42941	2.45255	2.45899	2.49879	2.51885	2.54464
EuFB4	Exp	---	2.285	2.435	2.501	2.523	2.454	2.379	2.382
	6-31G(d)	2.43977	2.43740	2.41493	2.45573	2.45866	2.49084	2.51487	2.55854
	6-311+G(d,p)	2.46726	2.47040	2.42842	2.46010	2.45499	2.49916	2.52597	2.55069
EuFB5	Exp	---	2.302	2.414	2.505	2.450	2.475	2.400	2.378
	6-31G(d)	2.44026	2.44034	2.41624	2.45504	2.46078	2.49121	2.51015	2.55372
	6-311+G(d,p)	2.44776	2.53825	2.42658	2.42601	2.54134	2.44801	2.49272	2.49287
EuFB6	Exp	---	2.375	2.362	---	---	2.407	2.489	---
	6-31G(d)	2.42206	2.41687	2.37586	2.43528	2.40375	2.47269	2.46509	---
	6-311+G(d,p)	2.44596	2.44824	2.41365	2.43347	2.42603	2.48318	2.46487	---
EuFB7	Exp	---	2.371	2.451	---	2.381	---	2.568	2.524
	6-31G(d)	2.44177	2.44509	2.43288	2.43866	2.46068	2.49008	2.50552	2.54699
	6-311+G(d,p)	2.46682	2.47992	2.44283	2.44789	2.45712	2.50020	2.51416	2.53519
EuTTA	Exp	2.419	2.405	2.369	2.389	2.330	2.380	2.408	2.424
	6-31G(d)	2.38750	2.48513	2.34925	2.38052	2.39384	2.45762	2.50731	2.58343
	6-311+G(d,p)	2.38560	2.48084	2.37315	2.37940	2.41375	2.45428	2.52138	2.58793

The DFT-calculated bond lengths of monohydrate and dihydrate complexes are shown in Table 3. By comparing the average Eu-O bond distances of the ligands and those values for the coordinating water molecules in both hydrate and dihydrate complexes, it was found that increasing the number of coordinated waters cause an increase in Eu-O ligand bond distance. Specifically, Eu-ligand (Eu-$O_{1/6}$) bonds and Eu-H_2O (Eu-$O_{7/8}$) bonds in dihydrate complexes are 1.51% and 2.32% longer than in monohydrate complexes, respectively, when calculated using the 6-31G(d) basis set. For the 6-311+G(d,p) basis set, the Eu-ligand and Eu-H_2O bonds are 1.25% and 2.25% longer, respectively. The presence of a second H_2O molecule in the coordination sphere of the dihydrate complexes causes steric pressure around the europium ion which is alleviated by the elongation of Eu-ligand and Eu-H_2O bonds[58]. Based on these results, increasing the number of coordinated water molecules to the complexes will decrease the luminescent quantum yield for three main reasons. In the Dexter energy transfer[59] mechanism which is prevalent in Eu^{3+} complexes[60], energy transfer can happen between a donor and acceptor system by bilateral exchange of electrons. This mechanism has a rate constant that exponentially

decays as the distance between the two systems increases. Therefore, the increase in bond distances between the monohydrate and dihydrate complexes, even if slight, could have a significant diminishing effect on the energy transfer and therefore the luminescent quantum yield. Coordinated water molecules can attenuate luminescent quantum yield of all lanthanides due to vibrations in the H_2O molecule that arise by energy migration during the energy relaxation process[61]. Also, Eu^{3+} ions are particularly sensitive to water molecule because its emissions (580, 593 and 613 nm) partially overlap with the fourth overtone of water (597-601 nm).[62]

Table 3. DFT-calculated Eu-O bond lengths in monohydrate and dihydrate complexes.

Complexes	Basis set	Eu-O_1 (Å)	Eu-O_2 (Å)	Eu-O_3 (Å)	Eu-O_4 (Å)	Eu-O_5 (Å)	Eu-O_6 (Å)	Eu-O_7 (Å)	Eu-O_8 (Å)
EuFB2(H_2O)	6-31G(d)	2.39338	2.44564	2.38094	2.45482	2.42810	2.43535	2.48056	---
	6-311+G(d,p)	2.43464	2.47634	2.42347	2.43128	2.44805	2.44864	2.47784	---
EuFB2(H_2O)$_2$	6-31G(d)	2.46491	2.45699	2.43292	2.46412	2.47381	2.50314	2.52049	2.56250
	6-311+G(d,p)	2.46372	2.46608	2.44633	2.48051	2.48675	2.50142	2.52344	2.55897
EuFB6(H_2O)	6-31G(d)	2.42206	2.41687	2.37586	2.43528	2.40375	2.47269	2.46509	---
	6-311+G(d,p)	2.44596	2.44824	2.41365	2.43347	2.42603	2.48318	2.46487	---
EuFB6(H_2O)$_2$	6-31G(d)	2.45097	2.45039	2.42452	2.44774	2.45834	2.49372	2.50648	2.55132
	6-311+G(d,p)	2.46928	2.47378	2.43822	2.45672	2.48379	2.51349	2.51115	2.54721
EuFB9(H_2O)	6-31G(d)	2.39653	2.43926	2.38525	2.44651	2.42873	2.43133	2.47582	---
	6-311+G(d,p)	2.41505	2.48055	2.41706	2.43261	2.45140	2.44994	2.46604	---
EuFB9(H_2O)$_2$	6-31G(d)	2.45394	2.45021	2.42297	2.44826	2.46017	2.49447	2.50064	2.54522
	6-311+G(d,p)	2.47352	2.50439	2.43352	2.44705	2.48478	2.48591	2.47950	2.53049

The dihedral angles between the benzene ring and the carboxylate groups are reported in Table 4. The dihedral angles were not reported as calculated, but they were normalized between 0° and 90°. Normally, dihedral angles are reported as numbers between -180° and 180°, but this does not allow for calculation of meaningful average values. To allow for proper average values calculations and for future comparison with the HOMO, LUMO, singlet (S_1) and triplet (T_1) energy levels, the absolute values of negative dihedral angles were reported and for angles greater than 90° the supplementary angle was reported. Comparing the dihedral angles calculated using the 6-31G(d) optimized structure in certain compounds (EuFB3 through EuFB7) it was noted that the dihedral angle for R^R was consistently higher than the angles for R^L and R^T. The difference in dihedral angles is consistently over 30° and a possible explanation could be the presence of coordinated water molecules that cause the benzene ring in the ligand to assume a more strained conformation. However, if that was the case R^L and R^R would present

similar dihedral angles due to their similar environment. Moreover, the large discrepancies between R^L and R^R dihedral angle disappear in the 6-311+G(d,p) basis sets, suggesting that the differences could be artifacts of the more constrained basis set (6-31G(d)). It was also noted that the dihedral angles for R^T are also consistently lower (from about 1° to 10° less) than the angles for R^L and R^R across both basis sets. In this case, the difference in angles is attributed to the different environments in which R^T, R^L and R^R reside. R^L and R^R are close to coordinated water molecules which increase the steric pressure and might cause the ligands to assume a more strained conformation with higher dihedral angles. On the other hand, R^T is outside of the sphere of influence of the coordinated water molecules and can assume a more relaxed conformation and lower dihedral angle. This can be confirmed by comparing the dihedral angles of monohydrate and dihydrate complexes (Table 5). It was observed that the dihedral angles for the dihydrate EuFB6 and EuFB9 complexes (54.181° and 49.207°, respectively) are higher than the angles for the monohydrate EuFB6 and EuFB9 (45.925° and 39.037°, respectively). However, this trend is not found in the EuFB2 complex (dihydrate = 71.467°, monohydrate = 76.796°) where the average dihedral angle increases when going from monohydrate to the dihydrate complex.

Comparing ligands with one ortho substituents against complexes with two ortho substituents, it was noted that while the ortho-monosubstituted ligands have an average dihedral angle that ranges from 0.886° to 5.156° the ortho-disubstituted ligands have dihedral angles that range from 39.037° to 76.796°. The high range of angles in the ortho-disubstituted ligands can be attributed to the nature of the substituent. For all these ligands, one substituent is always fluorine, while the second changes from a fluorine to a chlorine to a nitro group. If the second substituent is fluorine, like in ligands FB6 and FB9, the dihedral angle was recorded on the lower end of the scale (45.925° and 39.037°, respectively). Similarly, a nitro substituent (FB8) had a dihedral angle of 42.774°. Adding a chlorine substituent caused the dihedral angle to increase significantly to a value of 76.796° and it can be related to the large size of the chlorine's atomic orbitals and atomic radius.

Based on these results, we can determine that 6-311+G(d,p) more systematically models the studied complexes. In this project, comparisons and explanations were made using the computational data

obtained using the 6-311+G(d,p) basis set due to higher level of theory and to be more consistent throughout the discussion.

Table 4. Dihedral angles in fluorobenzoate complexes between the benzene ring and the carboxylate group of the left (R^L), top (R^T) and right (R^R) ligands.

Complexes	6-31G*				6-311+G**			
	R^L (°)	R^T (°)	R^R (°)	Avg (°)	R^L (°)	R^T (°)	R^R (°)	Avg (°)
EuFB1	2.753	1.519	3.964	2.745	9.318	1.415	4.312	5.015
EuFB2	59.605	53.724	54.726	56.018	68.450	88.429	73.508	76.796
EuFB3	7.433	2.173	47.101	18.902	11.440	1.909	2.119	5.156
EuFB4	5.546	1.433	42.321	16.433	3.004	1.160	7.563	3.909
EuFB5	4.806	1.763	42.339	16.303	0.073	0.888	1.698	0.886
EuFB6	1.821	37.944	40.163	26.643	44.631	43.191	49.952	45.925
EuFB7	4.979	0.073	40.879	15.310	6.039	2.420	1.898	3.452
EuFB8	54.687	56.122	77.636	62.815	33.876	27.631	66.814	42.774
EuFB9	34.709	32.253	31.676	32.879	40.241	38.482	38.388	39.037

Table 5. Dihedral angles in monohydrate and dihydrate fluorobenzoate complexes between the benzene ring and the carboxylate group of the left (R^L), top (R^T) and right (R^R) ligands.

Complexes	6-31G*				6-311+G**			
	R^L (°)	R^T (°)	R^R (°)	Avg (°)	R^L (°)	R^T (°)	R^R (°)	Avg (°)
EuFB2$(H_2O)_2$	77.200	59.236	64.662	67.033	67.283	69.312	77.807	71.467
EuFB2(H_2O)	59.605	53.724	54.726	56.018	68.450	88.429	73.508	76.796
EuFB6$(H_2O)_2$	45.516	36.317	61.791	47.875	51.151	41.189	70.203	54.181
EuFB6(H_2O)	1.821	37.944	40.163	26.643	44.631	43.191	49.952	45.925
EuFB9$(H_2O)_2$	41.548	33.698	58.777	44.674	42.850	39.442	65.330	49.207
EuFB9(H_2O)	34.709	32.253	31.676	32.879	40.241	38.482	38.388	39.037

3.1.2 Frontier Orbital Analysis

The highest occupied molecular orbital (HOMO) and lowest unoccupied molecular orbital (LUMO) can provide crucial information about a system like stability, excitation energy, etc. Herein, the number and position of fluorine substitutions on the 2-fluorobenzoic acid ring affect the energies of the frontier orbitals (HOMO and LUMO). Furthermore, we will compare the frontier orbitals of these fluorinated

benzoates with those of a vastly used β-diketonate ligand (TTA). The energies of the frontier orbitals differ slightly when calculated with different basis sets. Specifically, the 6-311+G(d,p) basis sets shows consistently lower energies than the 6-31G(d) basis set. All the following observations were conducted using the 6-311+G(d,p) basis sets since the trends are true for both basis sets in most situations.

3.1.2.1 Changing number and position of substituents on fluorobenzoate ligands

The calculated HOMO and LUMO for the compounds in Kalyakina et al. as well as the EuTTA complex are visually represented in Figure A2 and Figure A3. The energies of the frontier orbitals are shown in Table 6 and plotted in Figure 11. Comparing the HOMO and LUMO energies for the complexes synthesized in Kalyakina et al., it was found that the energy decreases as the number of fluorine substituents increases. However, it was also noted that the position of the substituents produces a significant effect on the frontier orbital energies.

HOMO: within the complexes in Kalyakina et al., the highest HOMO energy was calculated for the EuFB6 complex (-0.26743 eV). Overall, the EuTTA complex has the highest energy HOMO (-0.22610 eV) and EuFB8 has the lowest energy HOMO (-0.27204 eV). Specifically, comparing the HOMO for EuFB3 (-0.26064 eV) and the HOMO for EuFB6 (-0.26743 eV), adding a fluorine atom in the ortho position had a small decreasing effect on the HOMO energy (ΔE = -0.00679 eV). Similarly, by comparing the HOMO of EuFB1 (-0.26024 eV), the HOMO of EuFB3 (-0.26064 eV) and the HOMO of EuFB4 (-0.27092 eV), it emerges that adding a fluorine atom in the meta position has an increasing effect on the HOMO energy for the 6-31G(d) basis set but a negligible decreasing effect for the 6-311+G(d,p) basis set ($\Delta E_{6\text{-}31G(d)}$ = +0.00498 eV and $\Delta E_{6\text{-}311+G(d,p)}$ = -0.00040 eV), while adding a fluorine atom in the para position has a strong decreasing effect on the HOMO energy for both basis sets (ΔE = -0.01068 eV). Finally, replacing a fluorine atom in the ortho position with a nitro group like between complexes EuFB9 (-0.28569 eV) and EuFB8 (-0.28758 eV) causes a small decrease in the HOMO energy (ΔE = -0.00189 eV), while replacing a fluorine atom in the ortho position with a chlorine atom like between complexes

EuFB1 (-0.26024 eV) and EuFB2 (-0.26107 eV) causes a small decrease in the HOMO energy (ΔE = -0.00083 eV).

LUMO: overall the highest energy LUMO for fluorobenzoate ligands was calculated for EuFB2 (-0.05766 eV) and the lowest energy LUMO was calculated for EuFB8 (-0.12329 eV). Contrary to the trends seen in the HOMO, the changes in LUMO energy when adding a fluorine atom in the ortho position causes a substantial increase in LUMO energy (ΔE = +0.00757 eV). This effect can be seen when comparing the LUMO energies of the EuFB3 complex (-0.07771 eV) and of the EuFB6 complex (-0.07014 eV). Adding a fluorine atom in the meta position causes a large decrease in LUMO energy (ΔE = -0.01103 eV) like seen between the LUMO levels of EuFB1 (-0.06668 eV) and EuFB3 (-0.07771 eV). Similarly to HOMO energy changes, adding a fluorine in the para position has a decreasing effect on the LUMO energy (ΔE = -0.00434 eV) but the intensity of the change is significantly reduced like seen between the LUMO levels of EuFB1 (-0.06668 eV) and EuFB4 (-0.07102 eV). By comparing the LUMO energies of EuFB9 (-0.09192 eV) and EuFB8 (-0.12329 eV) it can be noted that when changing a fluorine in the ortho position with a nitro group, the LUMO energy significantly decreases (ΔE = -0.03137 eV), while comparing the LUMO of EuFB1 (-0.06668 eV) and EuFB2 (-0.05766 eV) it was noted that the LUMO energy increase (ΔE = +0.00902 eV). Finally, the LUMO energy of EuTTA (-0.09932 eV) falls in between the LUMO of EuFB9 (-0.09192 eV) and EuFB8 (-0.12329 eV).

HOMO-LUMO gap: the largest HOMO-LUMO gap calculated was in EuFB2 (0.20368 eV) for the 6-311+G(d,p) basis set and in EuFB4 (0.19990 eV) for the 6-31G(d) basis set. The lowest energy gap was calculated for EuFB8 in the fluorobenzoate ligands (0.16429 eV) , while EuTTA has the lowest energy gap overall (0.14049 eV). Among the fluorine substituted fluorobenzoate complexes, EuFB3 has the lowest HOMO-LUMO gap (0.18293 eV) due to the opposing effects of the meta substitution which cause the HOMO to increase and the LUMO to decrease making the gap smaller. Adding a fluorine atom in the ortho and para position has negligible effects on the HOMO-LUMO gap since a fluorine ortho modification cause almost insignificant changes and fluorine para modifications decrease both the HOMO

and LUMO levels. Substituting a fluorine atom in the ortho position with a nitro group produces a large decrease in HOMO-LUMO gap like seen between EuFB9 and EuFB8.

Table 6. Calculated HOMO, LUMO energies and HOMO-LUMO gaps for the fluorobenzoate complexes and the TTA complex using both the 6-31G(d) and the 6-311+G(d,p) basis sets.

Complexes	6-31G(g)			6-311+G(d,p)		
	HOMO (eV)	LUMO (eV)	GAP (eV)	HOMO (eV)	LUMO (eV)	GAP (eV)
EuFB1	-0.24936	-0.05621	0.19315	-0.26024	-0.06668	0.19356
EuFB2	-0.25070	-0.05180	0.19890	-0.26134	-0.05766	0.20368
EuFB3	-0.24438	-0.06033	0.18405	-0.26064	-0.07771	0.18293
EuFB4	-0.25408	-0.05397	0.20011	-0.27092	-0.07102	0.19990
EuFB5	-0.25260	-0.06362	0.18898	-0.26846	-0.07632	0.19214
EuFB6	-0.25068	-0.06057	0.19011	-0.26743	-0.07604	0.19139
EuFB7	-0.26127	-0.07153	0.18974	-0.28190	-0.09101	0.19089
EuFB8	-0.27204	-0.11185	0.16019	-0.28758	-0.12329	0.16429
EuFB9	-0.26334	-0.07635	0.18699	-0.28569	-0.09192	0.19377
EuTTA	-0.22610	-0.08469	0.14141	-0.23981	-0.09932	0.14049

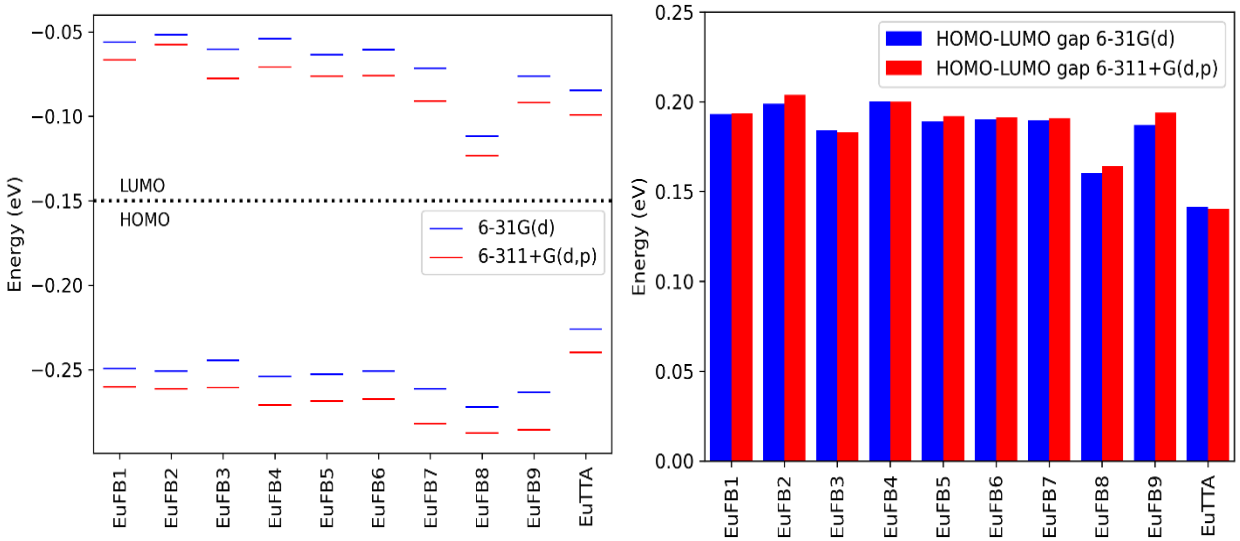

Figure 11. HOMO and LUMO energies (left) and HOMO-LUMO gaps (right) for fluorobenzoate ligands reported in Kalyakina et al. and for EuTTA calculated using both the 6-31G(d) and the 6-311+G(d,p) basis sets.

3.1.2.2 Moving a single fluorine atom around the ring of a benzoate ligand

The calculated HOMO and LUMO energies for the newly modeled compounds are shown in Table **7** and plotted in Figure 12, while the HOMO and LUMO orbitals are visually represented in Figure A4 and Figure A5, respectively.

HOMO: comparing the HOMO energies of the complexes obtained by moving one fluorine atom around the ring of a benzoate ligand showed small diverse changes in energy. Going from one ortho position to the other, from EuFB1o1 with a HOMO energy of -0.26024 eV to EuFB1o2 with a HOMO energy of -0.25570 eV, caused an energy change of -0.00002 eV and +0.00454 eV for the 6-31G(d) and 6-311+G(d,p) basis sets, respectively. Going from EuFB1m1 (-0.25919 eV) to EuFB1m2 (-0.25875 eV) caused an insignificant increase in energy of +0.00044 eV. Further comparing EuFB1o1 (-0.26024 eV) to EuFB1m1 (-0.025919 eV) and EuFB1p (-0.26130 eV), revealed that going from an ortho to a meta position has a minor increase in HOMO energy (ΔE = +0.00105 eV) while going from the ortho to the para position causes a small decrease in energy (ΔE = -0.00106 eV). These results confirm the trends previously seen in the fluorobenzoate complexes, but the changes in energy are negligible compared to the ones seen previously.

LUMO: regarding the LUMO orbitals, going from EuFB1o1 (-0.06668 eV) to EUB1o2 (-0.05983 eV) causes a substantial increase in LUMO energy (ΔE = +0.0685 eV). On the other hand, when going from one meta position (EuFB1m1, -0.06668 eV) to the other (FB1m2, -0.06668 eV) causes a minimal decrease in LUMO energy (ΔE = -0.00001 eV). Finally, when comparing EuFB1o1 (-0.06668 eV), to EuFB1m1 (-0.06624 eV) and EuFB1p (-0.05953 eV) shows that going form a fluorine in the ortho to the meta position causes a small decrease in LUMO energy (ΔE = 0.00044 eV) while going from the ortho to the para position causes a large increase in the LUMO energy (ΔE = +0.00715 eV). These trends match the ones found in the change of HOMO energies in this set of compounds, but only partially match the trends found in the original set of ligands in Kalyakina et al.

HOMO-LUMO gap: the lowest HOMO-LUMO gap (0.19250 eV) was calculated for EuFB1m2, while the highest HOMO-LUMO gap (0.20177 eV) belongs to EuFB1p. When comparing EuB1o1

(0.19356 eV) to EuFB1o2 (0.19587 eV) it was found that the HOMO-LUMO gap increases in energy (ΔE = +0.00231 eV). The opposite trend was observed when going from one meta position (EuFB1m1, 0.19295 eV) to the other (EuFB1m2, 0.19250 eV), where the HOMO-LUMO gap energy had small decrease (ΔE = -0.00045 eV). Finally comparing the HOMO-LUMO gaps of the compounds with ortho (EuFB1o1, 0.19356 eV), meta (EuFB1m1, 0.19295 eV) and para (EuFB1p, 0.20177 eV) fluorine substituents, it was observed that moving from the ortho to the meta position causes the gap to become smaller and decrease the energy (ΔE = -0.00231 eV), while going from the ortho to the para position causes a large increase in the HOMO-LUMO gap (ΔE = +0.00821 eV).

Table 7. HOMO, LUMO energies and HOMO-LUMO gaps for the complexes obtained by moving a fluorine atom around the ring of a benzoate ligand calculated using both the 6-31G(d) and the 6-311+G(d,p) basis sets.

Complexes	**6-31G(d)**			**6-311+G(d,p)**		
	HOMO (eV)	**LUMO (eV)**	**GAP (eV)**	**HOMO (eV)**	**LUMO (eV)**	**GAP (eV)**
EuFB1o1	-0.24936	-0.05621	0.19315	-0.26024	-0.06668	0.19356
EuFB1o2	-0.24938	-0.05608	0.19330	-0.25570	-0.05983	0.19587
EuFB1m1	-0.24526	-0.05092	0.19434	-0.25919	-0.06624	0.19295
EuFB1m2	-0.24498	-0.05099	0.19399	-0.25875	-0.06625	0.19250
EuFB1p	-0.24787	-0.04487	0.20300	-0.26130	-0.05953	0.20177

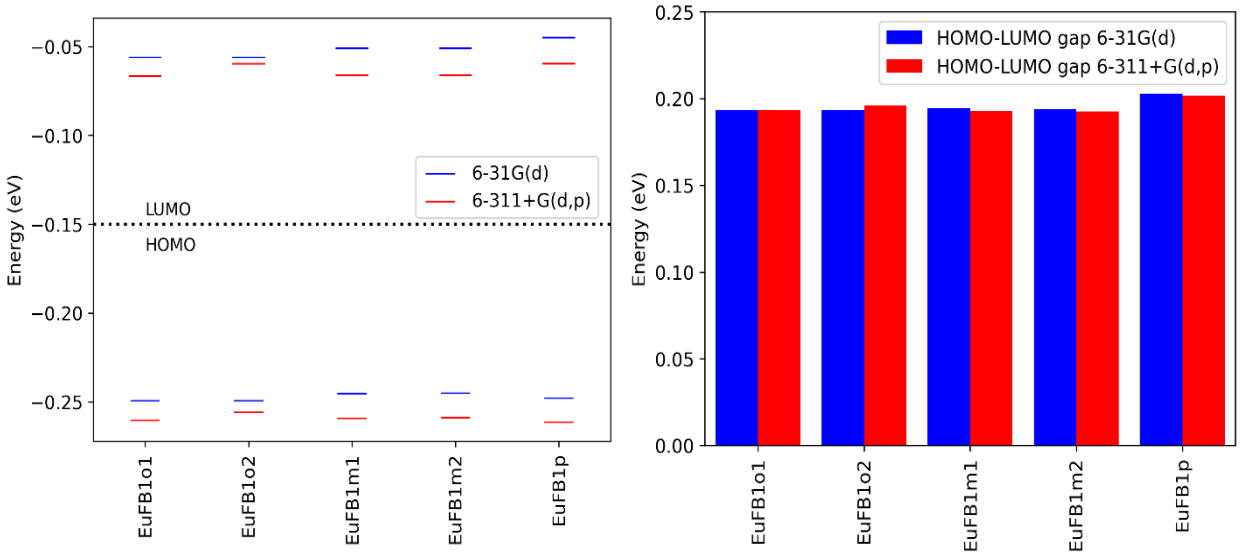

Figure 12. HOMO and LUMO energies (left) and HOMO-LUMO gaps (right) calculated using both the 6-31G(d) and the 6 311+G(d,p) basis sets for the complexes obtained by moving a single fluorine atom around a benzoate ring.

3.1.2.3 Changing the number of coordinated water molecules

The HOMO and LUMO orbitals are shown in Figure A6 and Figure A7, respectively. The HOMO and LUMO energies are reported in Table 8 and plotted along with the HOMO-LUMO gap in Figure 13.

HOMO and LUMO: for all three studied complexes, when going from the dihydrate complex to the monohydrate complex, the HOMO and LUMO energy decrease. The magnitude of the energy change appears to increase with the increase of substituents number. Specifically, ligands with 2 substituents (FB2) having a change of ΔE_{HOMO} = -0.00027 eV and ΔE_{LUMO} = -0.00466 eV, 3 substituents (FB6) having an energy change of ΔE_{HOMO} = -0.00255 eV and ΔE_{LUMO} = -0.00590 eV and 5 substituents (FB9) having an energy change of ΔE_{HOMO} = -0.00665 eV and ΔE_{LUMO} = -0.00860 eV.

HOMO-LUMO gap: the HOMO-LUMO gap shows a similar trend to the individual HOMO and LUMO energies, with the gap decreasing when going from dihydrate to monohydrate complexes. The magnitude of change also changes with the number of substituents, but it shows a trend opposite to the one previously observed where increasing the number of substituents decrease the magnitude of the

change. Ligand FB2 with two substituents shows a change in HOMO-LUMO gap between the dihydrate and monohydrate complexes of -0.00439 eV, ligand FB6 with 3 substituents shows a change of -0.00335 eV and ligand FB9 with 5 substituents show a change of -0.00195 eV.

Table 8. HOMO, LUMO energies and HOMO-LUMO gaps for the monohydrate and dihydrate complexes calculated using both the 6-31G(d) and the 6-311+G(d,p) basis sets.

Complexes	6-31G(d)			6-311+G(d,p)		
	HOMO (eV)	LUMO (eV)	GAP (eV)	HOMO (eV)	LUMO (eV)	GAP (eV)
$EuFB2(H_2O)_2$	-0.25817	-0.05332	-0.20485	-0.26107	-0.05300	-0.20807
$EuFB2(H_2O)$	-0.25070	-0.05180	-0.19890	-0.26134	-0.05766	-0.20368
$EuFB6(H_2O)_2$	-0.24762	-0.05631	-0.19131	-0.26488	-0.07014	-0.19474
$EuFB6(H_2O)$	-0.25068	-0.06057	-0.19011	-0.26743	-0.07604	-0.19139
$EuFB9(H_2O)_2$	-0.26201	-0.06886	-0.19315	-0.27904	-0.08332	-0.19572
$EuFB9(H_2O)$	-0.26334	-0.07635	-0.18699	-0.28569	-0.09192	-0.19377

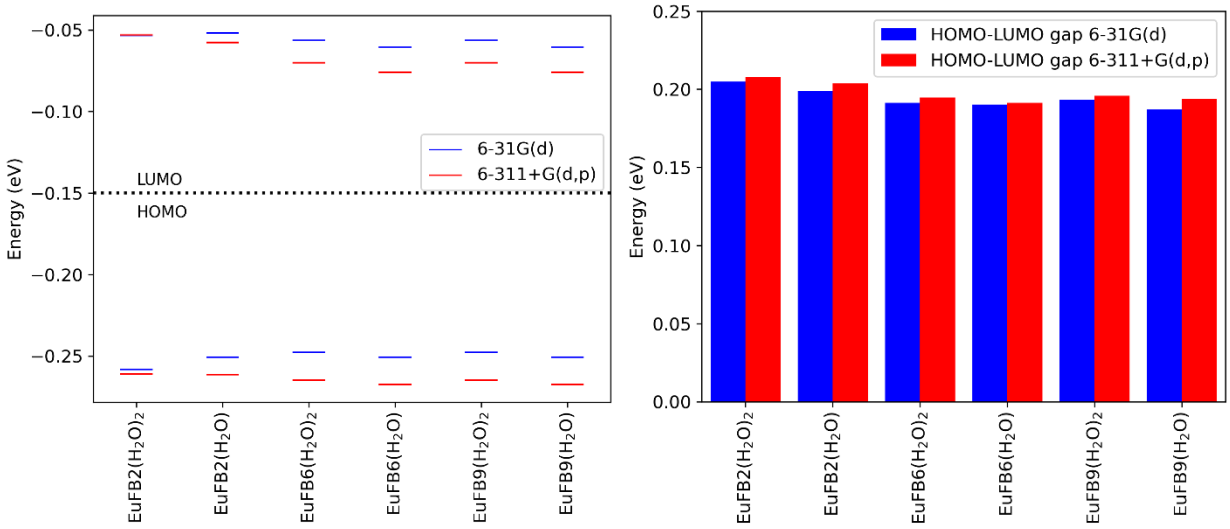

Figure 13. HOMO and LUMO energies (left) and HOMO-LUMO gaps (right) calculated using both the 6-31G(d) and the 6-311+G(d,p) basis sets for the monohydrate and dihydrate complexes.

3.1.2.4 Effects of the changing dihedral angle in the fluorobenzoate ligands

Comparing the various dihedral angles present in the ligands in Kalyakina et al. to the respective HOMO and LUMO energies, the effects of conjugation over the benzene-carboxylate system on those energies can be identified. When the benzene and the carboxylate are on the same plane and the dihedral angle is 0° or 180° the system is totally conjugated, while when the dihedral angle is 90° the system presents no conjugation. No trends between the dihedral angles and HOMO LUMO energies in those europium complexes was found (Figure 14). As the dihedral angle increased from a minimum of 0.889° in EuFB5 to a maximum of 76.796° in EuFB2, the HOMO and LUMO energies did not show any increasing or decreasing trend, but instead remained similar to one another suggesting that conjugation does not significantly contributes to the energies of the frontier orbitals or the HOMO-LUMO gap.

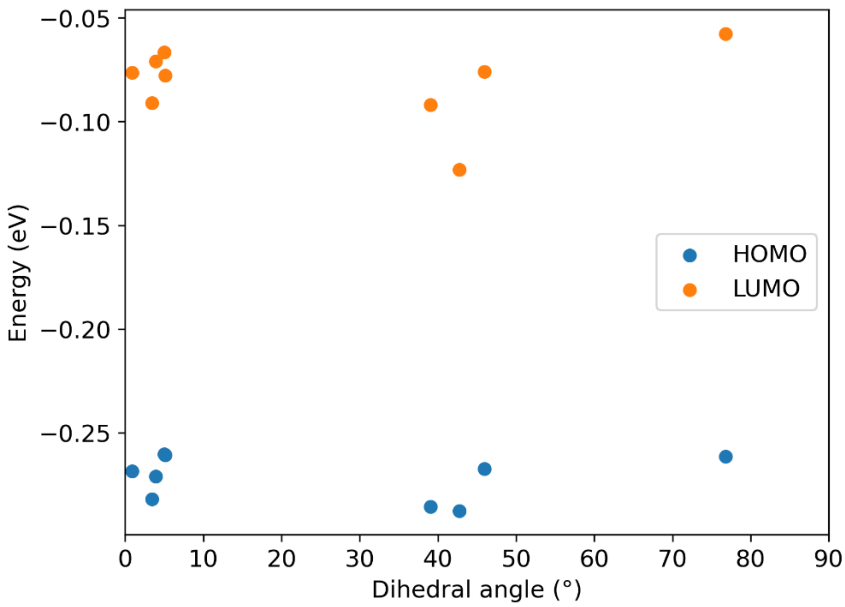

Figure 14. HOMO (blue) and LUMO (orange) energies plotted against the dihedral angles of the complexes in Kalyakina et al.

3.1.3 Absorption Spectra

TD-DFT calculations were performed on the optimized ground state geometries to determine the S_1 and T_1 electronic energy states. Only DFT-calculated absorption bands with a wavelength higher than 225 nm were considered for comparison to experimental values due to absence of experimental data below that cut-off. The DFT-calculated absorption spectra of the complexes are shown in Figure A8 through Figure A16 and the lowest λ_{max} for experimental and Calculated complexes are reported in Table 9.

By comparing the experimental lowest λ_{max} to the DFT-calculated λ_{max}, it was observed that the calculated spectra almost always present absorption bands that are blue shifted by at least 30 nm (and a maximum of 60 nm) from the experimental values. One exception is the spectrum for the EuFB8 complex calculated with the 6-31G(d) basis set, which shows an absorption band that is red shifted by about 20 nm. It was also noted that the DFT-calculated spectra of the EuFB3 and EuFB5 complexes present faint and unresolved bands at 271 and 261 nm, respectively, which more closely match the experimental λ_{max} of the respective complexes. The DFT-calculated lowest λ_{max} for the EuTTA complex also does not agree with the experimental values[63]. The DFT-calculated values are blue shifted by about 20 nm.

Table 9. Experimental and DFT-calculated lowest λ_{max} for the Eu-fluorobenzoate complexes and the EuTTA complex.

Complex	Exp. λ_{max} (nm)	6-31G(d) Calc. λ_{max} (nm)	6-311+G(d,p) Calc. λ_{max} (nm)
EuFB1	272	228	229
EuFB2	272	241	237
EuFB3	280	221	222
EuFB4	272	231	233
EuFB5	272	230	230
EuFB6	267	221	242
EuFB7	270	237	235
EuFB8	280	301	232
EuFB9	263	234	235
EuTTA	340	319	320

The DFT-calculated absorption spectra of the complexes obtained by moving a fluorine substituent across the benzene ring of the ligand to study the effects of these modifications on the absorption bands of the complexes. Negligible variations in the wavelength of the absorption bends were recorded. Between the complexes EuFB1o1 and EuFB1o2, an increase of 5 nm was observed in the band centered at 190 nm, while no change was recorded for the band centered at 229 nm. Comparing EuFB1m1 and EuFB1m2, no increase was recorded for the band at 190 nm and a 3 nm increase was recorded for the band at 229 nm. Finally, when going from EuFB1o1 to EuFB1m1 to EuFB1p an increase of 5 nm was recorded when going from the ortho position to the meta position and an increase of 1 nm was recorded when going from the meta position to the para position for the band at 190 nm. For the band at 229 nm, a 2 nm increase was observed when going from the ortho to the meta position and a 7 nm increase was observed when going from the meta position to the para position.

Table 10. DFT-calculated lowest λ_{max} for the complexes obtained by moving a fluorine substituent around the fluorobenzoate ring.

Complex	**6-31G(d)** **Calc. λ_{max} (nm)**	**6-311+G(d,p)** **Calc. λ_{max} (nm)**
EuFB1o1	228	229
	185	185
EuFB1o2	231	229
	190	190
EuFB1m1	230	231
	185	190
EuFB1m2	229	233
	185	190
EuFB1p	234	238
	185	191

The DFT-calculated spectra of monohydrate and dihydrate complexes were compared to determine the effects that the increase in number of coordinated water molecules has on the UV-Vis spectrum of the complexes. The spectrum of the monohydrate and dihydrate complexes can be found in the appendix (Figure A9, Figure A13, Figure A16, Figure A22-Figure A24) and the calculated absorption bands are reported in Table 11. The DFT-calculated UV-Vis absorption bands of the monohydrate and dihydrate complexes strongly agree with one another: the absorption band centered around 190 nm shows a maximum variation of 3 nm while the band centered at 235 nm shows a larger maximum variation of 15 nm between the monohydrate and dihydrate complexes.

Table 11. DFT-calculated lowest λ_{max} for the monohydrates and dihydrates Eu-fluorobenzoate complexes.

Complex	6-31G(d) Calc. λ_{max} (nm)	6-311+G(d,p) Calc. λ_{max} (nm)
EuFB2$(H_2O)_2$	235	237
	192	197
EuFB2(H_2O)	241	237
	190	196
EuFB6$(H_2O)_2$	239	236
	185	190
EuFB6(H_2O)	224	246
	187	187
EuFB9$(H_2O)_2$	232	237
	186	190
EuFB9(H_2O)	234	235
	189	190

Finally, the S_1 states with the highest oscillator strengths for each modeled complex were investigated to determine which orbitals participate in those transitions. Only S_1 states which present an absorption wavelength of over 200 nm were investigated because excitation at lower wavelengths is difficult to achieve in an experimental setup due to absorption by solvents and because wavelengths lower than 200 nm are rarely used for structural analysis.

3.1.3.1 EuFB1/ EuFB1o1

For complex EuFB1, three major S_1 excited states were calculated (Table 12). The first excited state with absorption at 229.96 nm presented a dominant transition between the HOMO-5 and LUMO orbitals. The second excited state with absorption at 236.9 nm had a dominant transition between the HOMO-3 and LUMO orbitals, while the third excited state (259.67 nm) presented a dominant transition between the HOMO and LUMO+1 orbitals (Figure 15).

Table 12. Major calculated excited states for the EuFB1 complex, including participating orbital transitions and percent contribution.

	6-31G(d)			**6-311+G(d,p)**	
λ_{max} (nm)	**Orbitals**	**Contribution (%)**	**λ_{max} (nm)**	**Orbitals**	**Contribution (%)**
228.3	HOMO-5 → LUMO	67.60	229.96	HOMO-5 → LUMO	43.26
234.7	HOMO-3 → LUMO	78.48	236.9	HOMO-3 → LUMO	52.92
			259.67	HOMO → LUMO+1	34.38

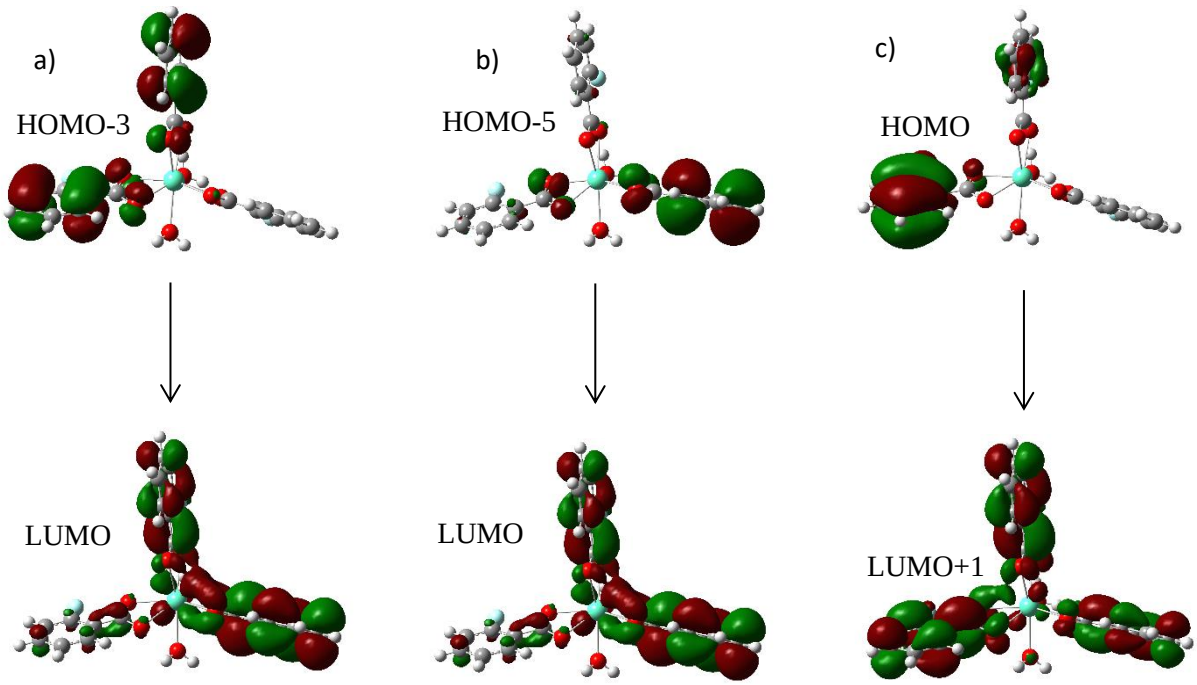

Figure 15. Major transitions in the EuFB1 complex for the 229.96 nm (a), the 236.9 nm (b) and 259.67 nm (c) excited state. Green orbitals are the positive values of the wavefunction, while the red orbitals are the negative values.

3.1.3.2 EuFB2/ EuFB2(H_2O)

Complex EuFB2 presents only one major excited state over 200 nm for the 6-311+G(d,p) (Table 13). The excited state absorbs 237.29 nm and presents a dominant transition between the HOMO-5 and LUMO orbitals (Figure 16).

Table 13. Major calculated excited states for the EuFB2 complex, including participating orbital transitions and percent contribution.

	6-31G(d)			6-311+G(d,p)	
λ_{max} (nm)	**Orbitals**	**Contribution (%)**	**λ_{max} (nm)**	**Orbitals**	**Contribution (%)**
200.65	HOMO-2 → LUMO+3	14.75	237.29	HOMO-5 → LUMO	35.58
239.49	HOMO-3 → LUMO+2	78.47539			
242.05	HOMO-4 → LUMO	44.26			

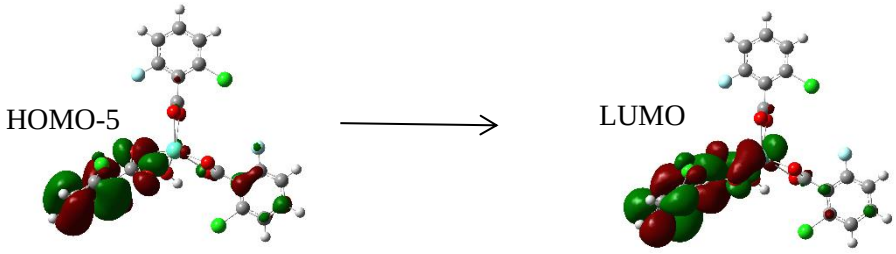

Figure 16. Major transition in the EuFB2 complex for the 237.29 nm excited state. Green orbitals are the positive values of the wavefunction, while the red orbitals are the negative values.

3.1.3.3 EuFB3

Complex EuFB3 presents three major S_1 excited states (Table 14). The first excited state with absorption at 230.42 nm presented a dominant transition between the HOMO-5 and LUMO+1 orbitals. The second excited state (270.66 nm) had a dominant transition between the HOMO-2 and LUMO orbitals, while the third excited state (274.36 nm) presented a dominant transition between the HOMO and LUMO orbitals (Figure 17).

Table 14. Major calculated excited states for the EuFB3 complex, including participating orbital transitions and percent contribution.

	6-31G(d)			**6-311+G(d,p)**	
λ_{max} (nm)	**Orbitals**	**Contribution (%)**	**λ_{max} (nm)**	**Orbitals**	**Contribution (%)**
221.72	HOMO-3 → LUMO+1	55.92	230.42	HOMO-3 → LUMO+1	15.41
226.95	HOMO-4 → LUMO	62.12	270.66	HOMO-2 → LUMO	72.62
255.19	HOMO-2 → LUMO	57.42	274.36	HOMO → LUMO	64.42
271.32	HOMO → LUMO	59.22			
273.52	HOMO-1 → LUMO	72.76			

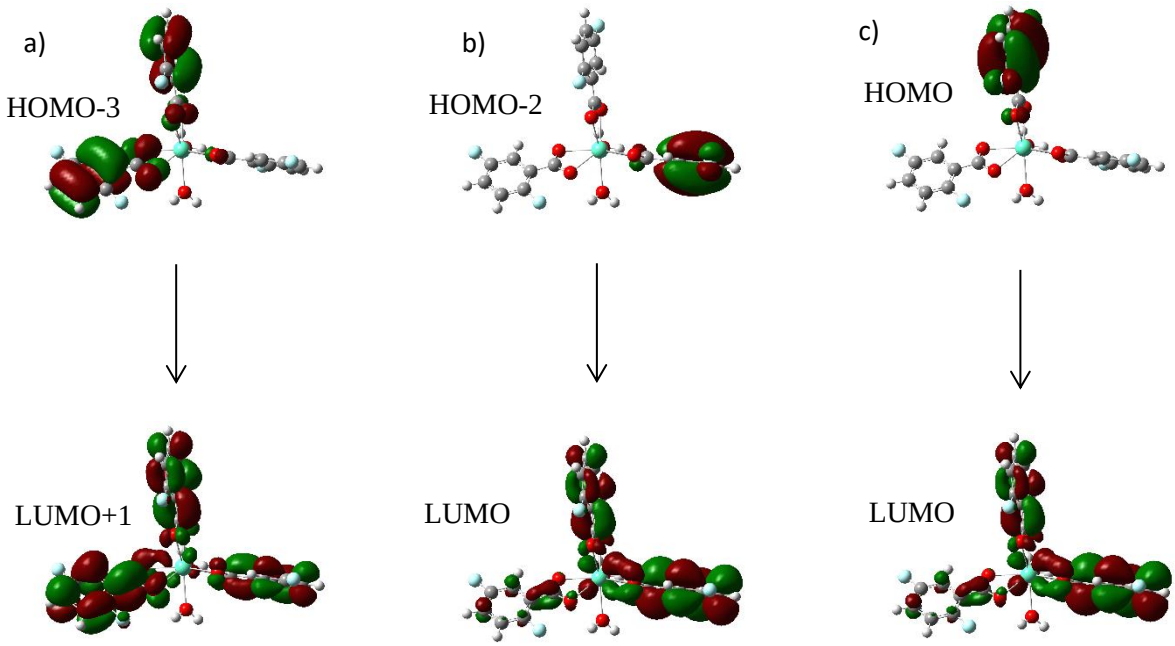

Figure 17. Major transitions in the EuFB3 complex for the 230.42 nm (a), the 270.66 nm (b) and 274.36 nm (c) excited state. Green orbitals are the positive values of the wavefunction, while the red orbitals are the negative values.

3.1.3.4 EuFB4

For complex EuFB4, the only major calculated excited state over 200 nm for the 6-311+G(d,p) absorbs 237.29 nm (Table 15) and presents a dominant transition between the HOMO-2 and LUMO orbitals (Figure 18).

Table 15. Major calculated excited states for the EuFB4 complex, including participating orbital transitions and percent contribution.

	6-31G(d)			6-311+G(d,p)	
λ_{max} (nm)	**Orbitals**	**Contribution (%)**	**λ_{max} (nm)**	**Orbitals**	**Contribution (%)**
228.07	HOMO-4 → LUMO	38.93	234.22	HOMO-2 → LUMO	43.09
245	HOMO-2 → LUMO	37.59			
251.92	HOMO-1 → LUMO	39.40			

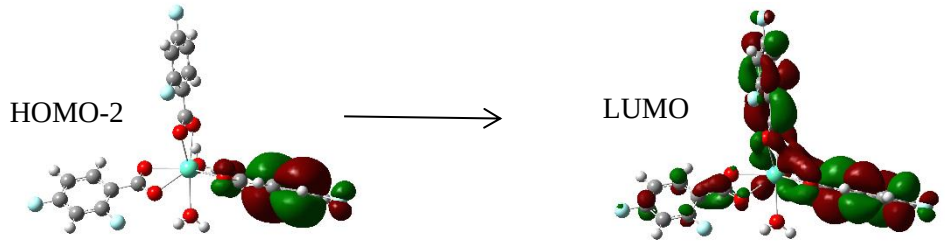

Figure 18. Major transitions in the EuFB4 complex for the 234.22 nm excited state. Green orbitals are the positive values of the wavefunction, while the red orbitals are the negative values.

3.1.3.5 EuFB5

Complex EuFB5 presents three major S_1 excited states (Table 16). The first excited state with absorption at 229.1 nm presented a dominant transition between the HOMO-4 and LUMO orbitals. The second excited state (260.11 nm) had a dominant transitions between the HOMO-1 and LUMO+1 orbitals and between the HOMO-1 and LUMO orbitals, while the third excited state (261.46 nm) presented a dominant transition between the HOMO and LUMO+2 orbitals (Figure 19).

Table 16. Major calculated excited states for the EuFB5 complex, including participating orbital transitions and percent contribution.

	6-31G(d)			**6-311+G(d,p)**	
λ_{max} (nm)	**Orbitals**	**Contribution (%)**	**λ_{max} (nm)**	**Orbitals**	**Contribution (%)**
224.42	HOMO-3 → LUMO+2	52.73	229.1	HOMO-4 → LUMO	20.07
229.27	HOMO-4 → LUMO	61.88	260.11	HOMO-1 → LUMO+1	21.29
231.9	HOMO-3 → LUMO	43.63		HOMO-1 → LUMO	20.29
252.89	HOMO-2 → LUMO	59.27	261.46	HOMO → LUMO+2	41.84
264.97	HOMO-1 → LUMO	53.48			

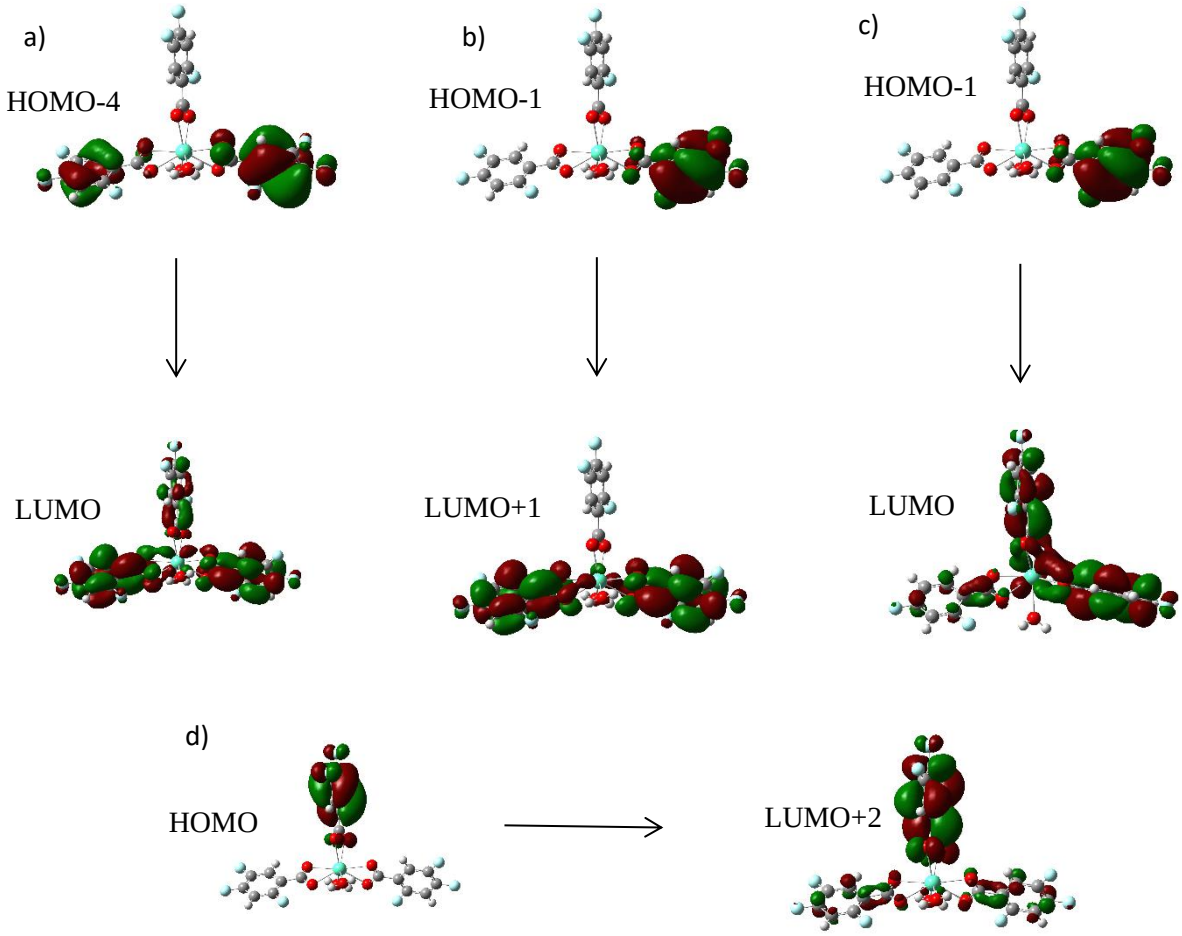

Figure 19. Major transitions in the EuFB5 complex for the 229.1 nm (a), the 260.11 nm (b-c) and 261.46 nm (d) excited state. Green orbitals are the positive values of the wavefunction, while the red orbitals are the negative values.

3.1.3.6 EuFB6/ EuFB6(H_2O)

Complex EuFB6 presents four major S_1 excited states (Table 17). The first excited state with absorption at 217.99 nm presented a dominant transition between the HOMO-5 and LUMO+2 orbitals. The second excited state (220.16 nm) had a dominant transition between the HOMO-6 and LUMO. The third excited state (241,23 nm) presented a dominant transition between the HOMO and LUMO+2 orbitals, while the fourth transition with absorption at 264.23 nm presented a dominant transition between the HOMO-1 and LUMO orbitals (Figure 20).

Table 17. Major calculated excited states for the EuFB6 complex, including participating orbital transitions and percent contribution.

	6-31G(d)			6-311+G(d,p)	
λ_{max} (nm)	Orbitals	Contribution (%)	λ_{max} (nm)	Orbitals	Contribution (%)
219.28	HOMO-7 → LUMO+1	24.14	217.99	HOMO-5 → LUMO+2	28.95
241.16	HOMO-4 → LUMO	29.02	220.16	HOMO-6 → LUMO	32.36
269.14	HOMO → LUMO	74.69	241.23	HOMO-5 → LUMO	24.50
			264.23	HOMO-1 → LUMO	50.20

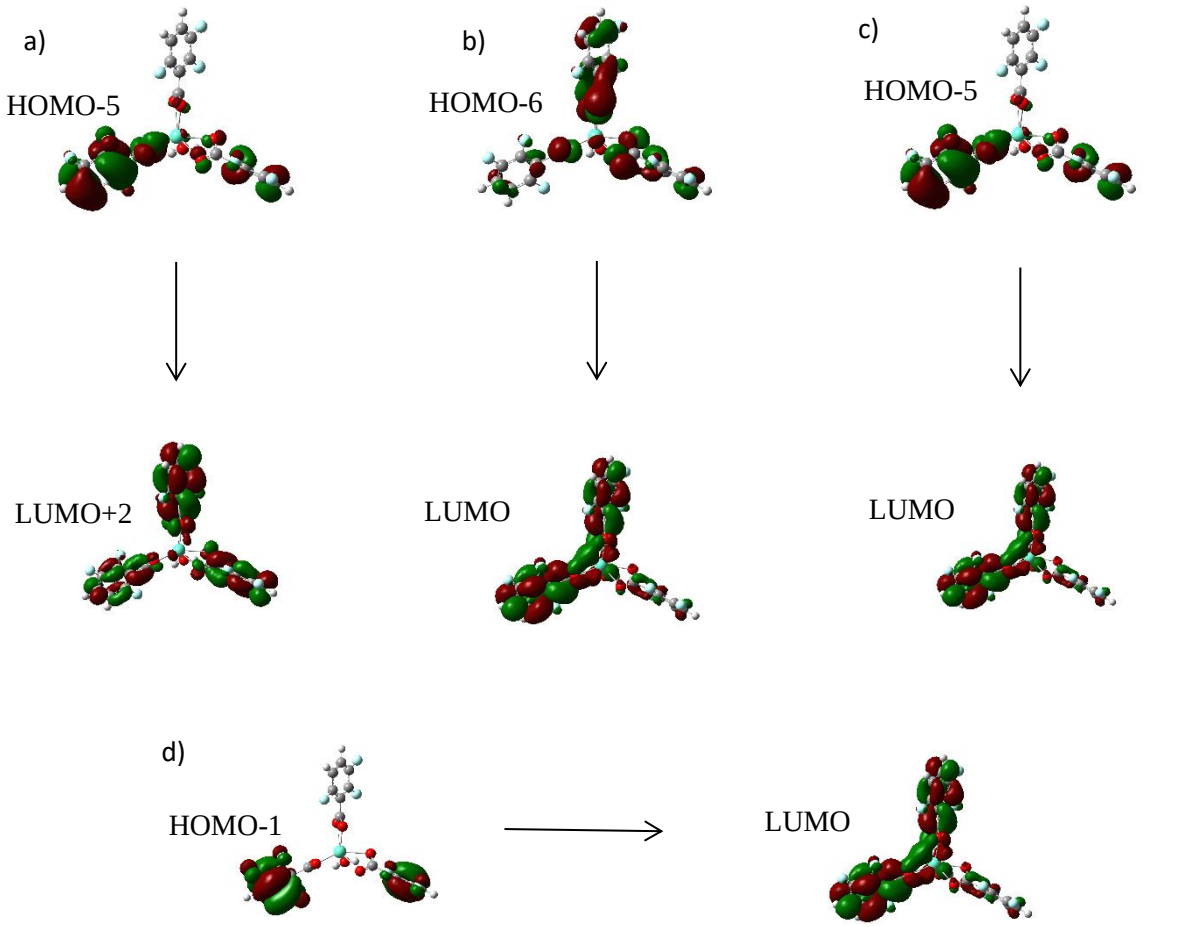

Figure 20. Major transitions in the EuFB6 complex for the 217.99 nm (a), the 220.16 nm (b), the 241.13 nm (c) and the 264.23 nm (d) excited states. Green orbitals are the positive values of the wavefunction, while the red orbitals are the negative values.

3.1.3.7 EuFB7

Complex EuFB7 presents three major S_1 excited states (Table 18). The first excited state with absorption at 234.56 nm presented a dominant transition between the HOMO-3 and LUMO+1 orbitals. The second excited state (234.71 nm) had a dominant transition between the HOMO-5 and LUMO, while the third excited state with absorption at 263.37 nm presented a dominant transition between the HOMO-2 and LUMO orbitals (Figure 21).

Table 18. Major calculated excited states for the EuFB7 complex, including participating orbital transitions and percent contribution.

	6-31G(d)			**6-311+G(d,p)**	
λ_{max} (nm)	**Orbitals**	**Contribution (%)**	**λ_{max} (nm)**	**Orbitals**	**Contribution (%)**
231.12	HOMO-2 → LUMO+2	45.36	234.56	HOMO-3 → LUMO+1	62.47
246.35	HOMO-4 → LUMO	25.90	234.71	HOMO-5 → LUMO	48.16
266.67	HOMO-1 → LUMO	68.19	263.37	HOMO-2 → LUMO	71.42

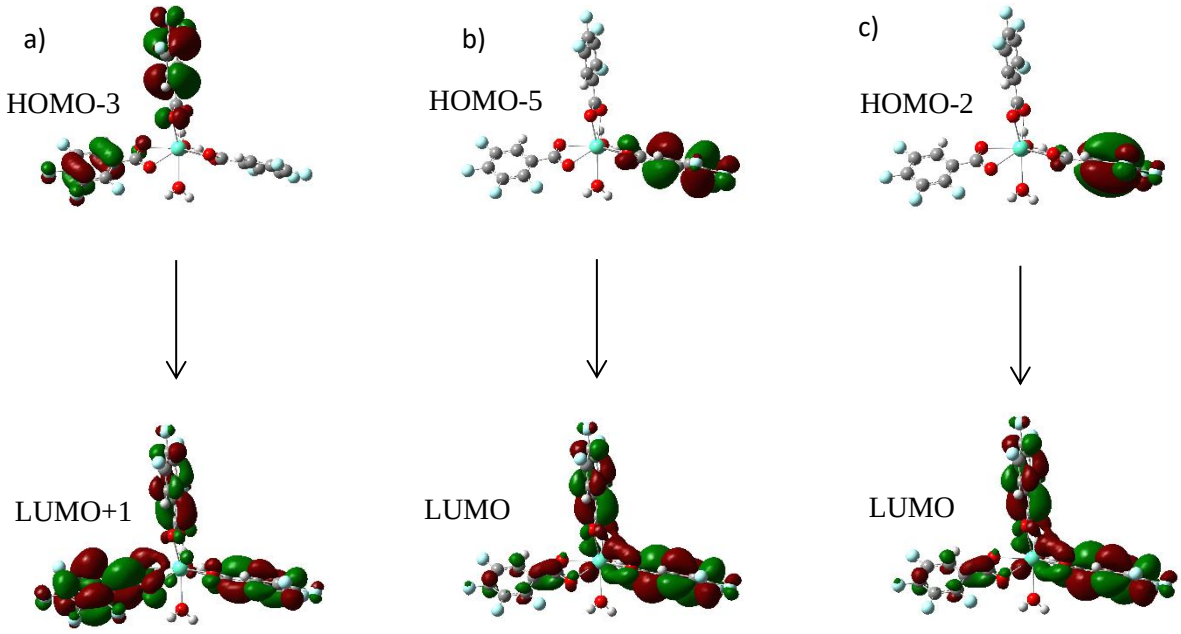

Figure 21. Major transitions in the EuFB7 complex for the 234.56 nm (a), the 234.71 nm (b), and the 263.37 nm (c) excited states. Green orbitals are the positive values of the wavefunction, while the red orbitals are the negative values.

3.1.3.8 EuFB8

Complex EuFB8 presents many S_1 excited states over 200 nm (Table 19). The excited state with absorption at 207.06 nm presented a dominant transition between the HOMO-20 and LUMO+3 orbitals. The next excited state (234.71 nm) had a dominant transition between the HOMO-3 and LUMO+3, while the excited state with absorption at 263.37 nm presented two dominant transitions: one between the HOMO-4 and LUMO+2 and none between the HOMO-6 and LUMO+2 orbitals (Figure 22). The excited state with absorption at 294.98 has a dominant transition between the HOMO-3 and LUMO orbitals. Finally, the excited state with absorption at 323.45 nm presents a dominant transition between the HOMO-5 and LUMO orbitals (Figure 22)

Table 19. Major calculated excited states for the EuFB8 complex, including participating orbital transitions and percent contribution.

	6-31G(d)			6-311+G(d,p)	
λ_{max} (nm)	**Orbitals**	**Contribution (%)**	**λ_{max} (nm)**	**Orbitals**	**Contribution (%)**
202.44	HOMO-9 → LUMO+3	12.69	207.06	HOMO-20 → LUMO+3	23.17
222.61	HOMO-4 → LUMO+4	21.07	231.73	HOMO-3 → LUMO+3	48.45
232.07	HOMO-3 → LUMO+3	28.93	235.19	HOMO-4 → LUMO+2	26.44
260.4	HOMO-5 → LUMO	35.57		HOMO-6 → LUMO+2	26.17
299.17	HOMO → LUMO+2	61.98	294.98	HOMO-3 → LUMO	86.63
326.98	HOMO-3 → LUMO+1	38.48	323.45	HOMO-5 → LUMO	54.81

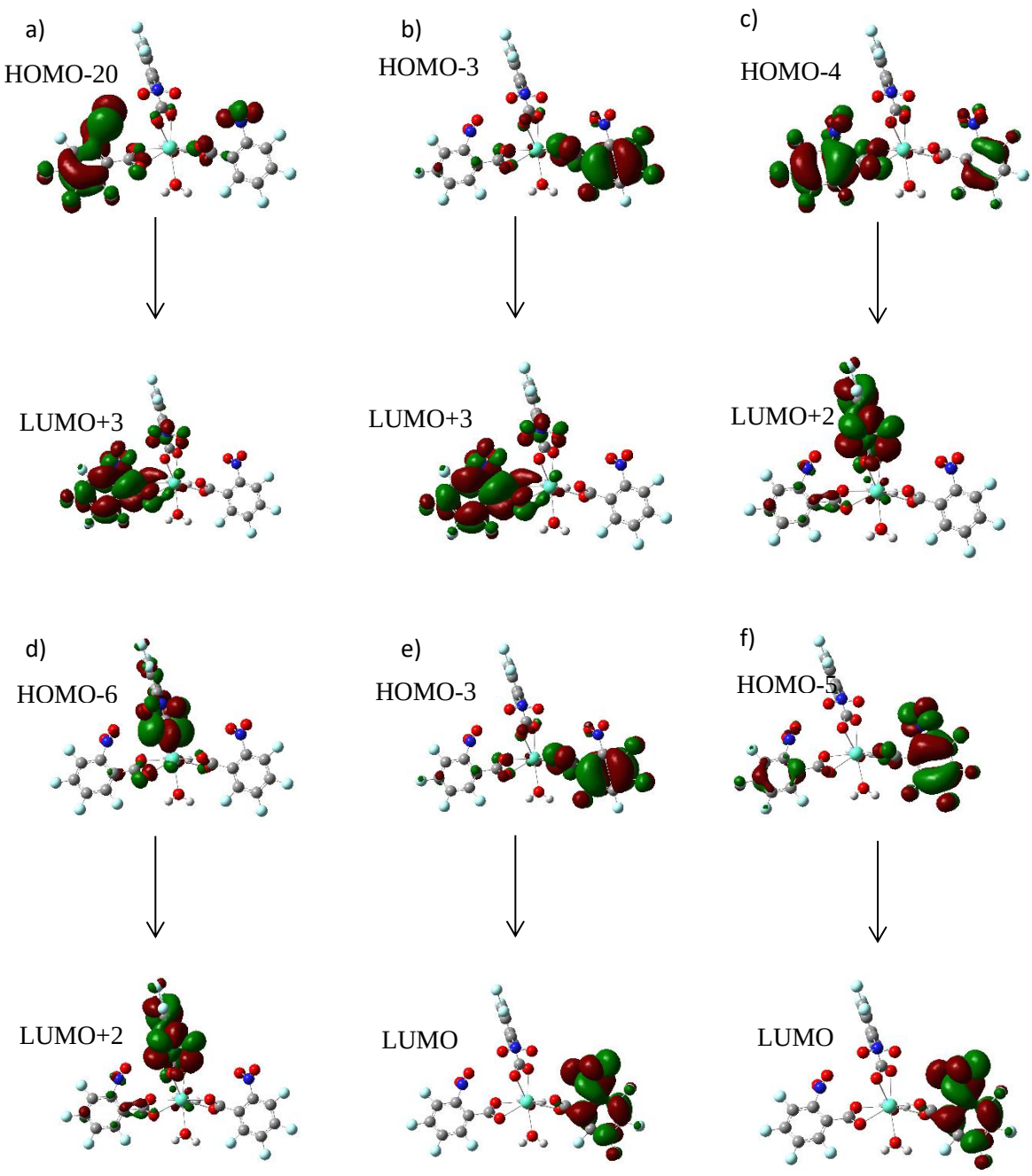

Figure 22. Major transitions in the EuFB8 complex for the 207.06 nm (a), the 231.73 nm (b), the 235.19 nm (c-d), the 295.98 nm (e), and the 323.45 nm (f) excited states. Green orbitals are the positive values of the wavefunction, while the red orbitals are the negative values.

3.1.3.9 EuFB9/ EuFB9(H_2O)

Complex EuFB9 presents three major S_1 excited states (Table 20). The first excited state with absorption at 223.59 nm presented a dominant transition between the HOMO-4 and LUMO+2 orbitals and a second dominant transition between the HOMO-6 and LUMO+1. The second excited state (225.51 nm) had a dominant transition between the HOMO-5 and LUMO+3, while the third excited state with absorption at 244.61 nm presented a dominant transition between the HOMO-3 and LUMO+1 orbitals (Figure 23).

Table 20. Major calculated excited states for the EuFB9 complex, including participating orbital transitions and percent contribution.

	6-31G(d)			**6-311+G(d,p)**	
λ_{max} (nm)	**Orbitals**	**Contribution (%)**	**λ_{max} (nm)**	**Orbitals**	**Contribution (%)**
226.53	HOMO-5 → LUMO+1	21.85	223.59	HOMO-4 → LUMO+2	21.09
245.26	HOMO-4 → LUMO	34.71		HOMO-6 → LUMO+1	20.81
			225.51	HOMO-4 → LUMO+2	29.85
			244.61	HOMO-3 → LUMO+1	23.34

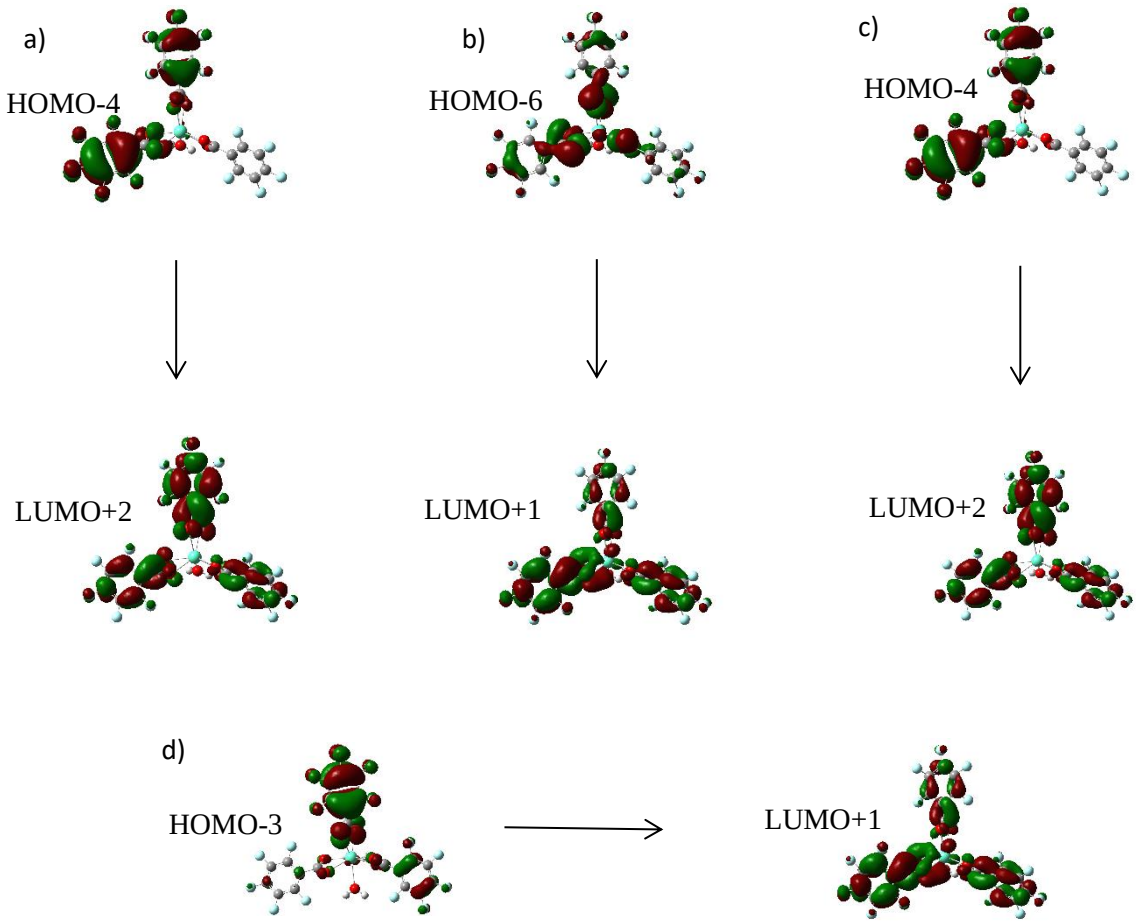

Figure 23. Major transitions in the EuFB9 complex for the 236.25 nm (a), the 241.01 nm (b), and the 246.88 nm (c) excited states. Green orbitals are the positive values of the wavefunction, while the red orbitals are the negative values.

3.1.3.10 EuTTA

Complex EuTTA presents five major S_1 excited states (Table 21). The first excited state with absorption at 208.22 nm presented a dominant transition between the HOMO-3 and LUMO+5 orbitals. The excited state at 265.74 nm has a dominant transition between the HOMO-10 and LUMO. The excited state with absorption at 270.38 nm had a dominant transition between the HOMO-8 and LUMO+1, while the excited state with absorption at 321.92 nm presented a dominant transition between the HOMO and

LUMO+2 orbitals. Finally, the excited state with absorption at 329.72 nm presented a dominant transition between the HOMO-2 and LUMO+1 (Figure 24).

Table 21. Major calculated excited states for the EuTTA complex, including participating orbital transitions and percent contribution.

	6-31G(d)			6-311+G(d,p)	
λ_{max} (nm)	**Orbitals**	**Contribution (%)**	**λ_{max} (nm)**	**Orbitals**	**Contribution (%)**
266.65	HOMO-9 → LUMO+2	16.17	208.22	HOMO-3 → LUMO+5	59.24
273.91	HOMO-4 → LUMO+2	58.29	265.74	HOMO-10 → LUMO	56.46
314.95	HOMO-2 → LUMO	16.06	270.38	HOMO-8 → LUMO+1	30.18
	HOMO-1 → LUMO+1	16.19	321.92	HOMO → LUMO+2	21.52
326.58	HOMO-1 → LUMO+1	39.03	329.72	HOMO-2 → LUMO+1	39.77

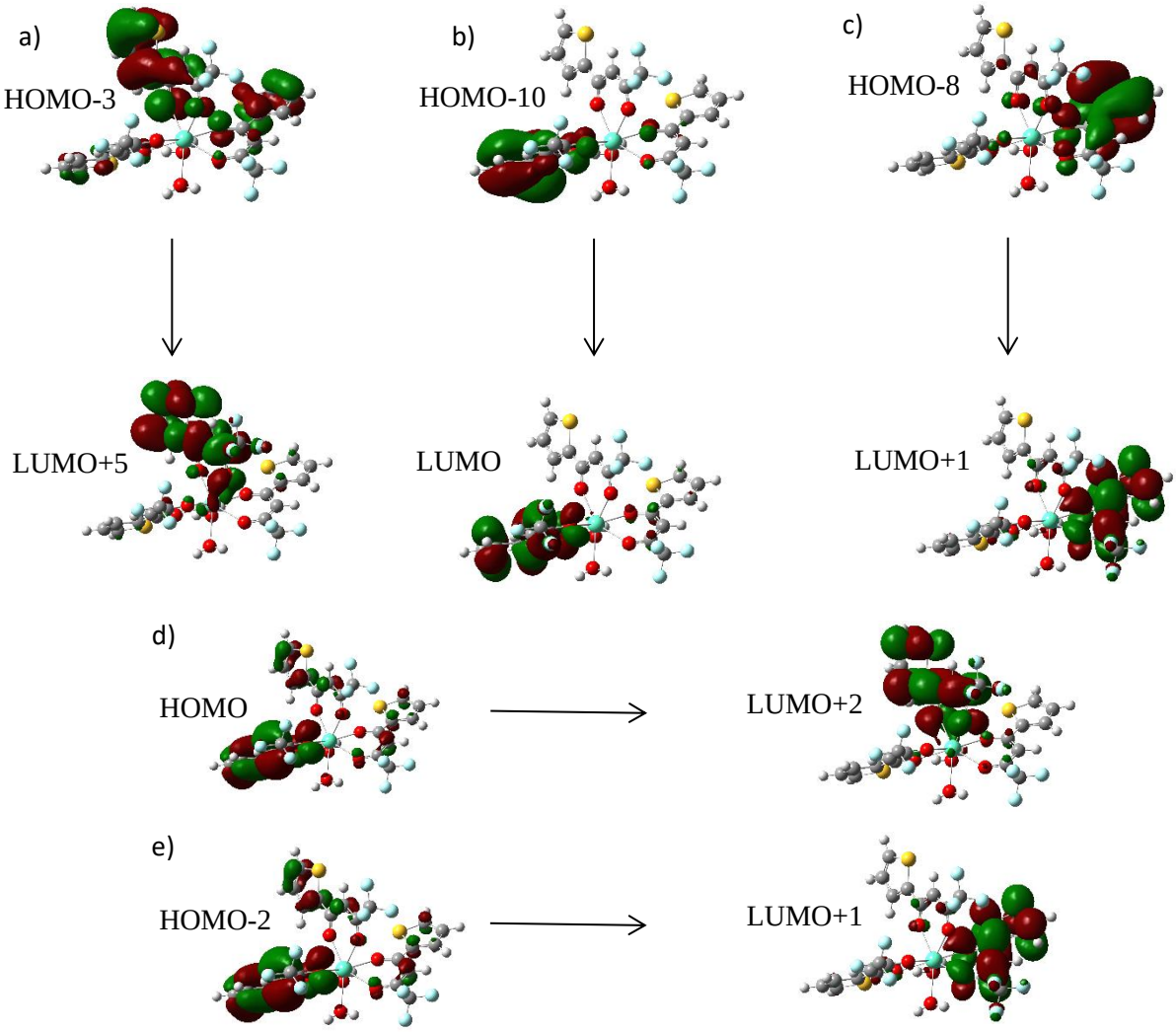

Figure 24. Major transitions in the EuTTA complex for the 208.22 nm (a), the 265.74 nm (b), the 270.38 nm (c), the 321.92 nm (d), and the 329.72 nm (e) excited states. Green orbitals are the positive values of the wavefunction, while the red orbitals are the negative values.

3.1.3.11 EuFB1o2

For complex EuFB1o2, two major S_1 excited states were calculated (Table 22). The first excited state with absorption at 227.77 nm presented a dominant transition between the HOMO-3 and LUMO+2 orbitals. The second excited state with absorption at 228.82 nm had a dominant transition between the HOMO-4 and LUMO orbitals (Figure 25).

Table 22. Major calculated excited states for the EuFB1o2 complex, including participating orbital transitions and percent contribution.

	6-31G(d)			6-311+G(d,p)	
λ_{max} (nm)	**Orbitals**	**Contribution (%)**	**λ_{max} (nm)**	**Orbitals**	**Contribution (%)**
229.89	HOMO-5 → LUMO	42.17	227.77	HOMO-3 → LUMO+2	40.07
232.38	HOMO-4 → LUMO	77.92	228.82	HOMO-4 → LUMO	47.68

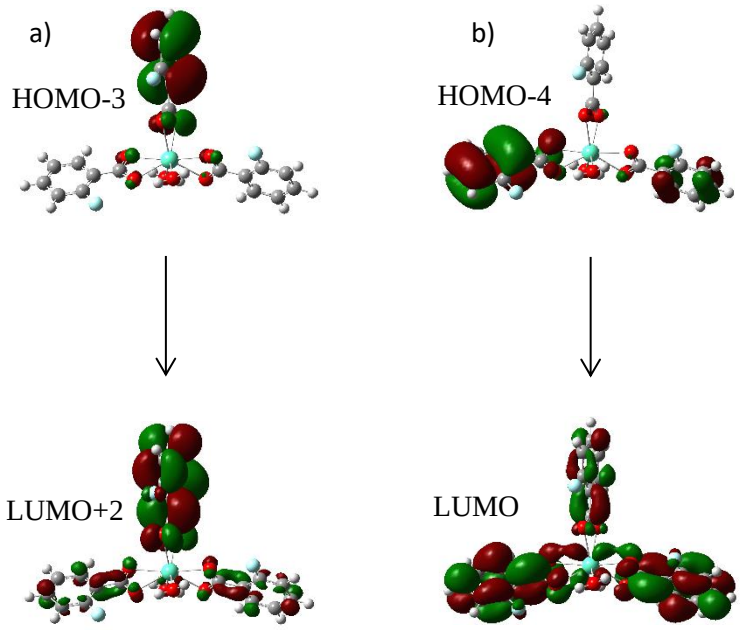

Figure 25. Major transitions in the EuFB1o2 complex for the 227.77 nm (a), and 228.82 nm (b) excited state. Green orbitals are the positive values of the wavefunction, while the red orbitals are the negative values.

3.1.3.12 EuFB1m1

For complex EuFB1m1, two major S_1 excited states were calculated (Table 23). The first excited state with absorption at 230.71 nm presented a dominant transition between the HOMO-3 and LUMO+2

orbitals. The second excited state with absorption at 231.72 nm had a dominant transition between the HOMO-4 and LUMO orbitals (Figure 26).

Table 23. Major calculated excited states for the EuFB1m1 complex, including participating orbital transitions and percent contribution.

	6-31G(d)			6-311+G(d,p)	
λ_{max} (nm)	**Orbitals**	**Contribution (%)**	**λ_{max} (nm)**	**Orbitals**	**Contribution (%)**
228.91	HOMO-4 → LUMO	42.78	230.71	HOMO-3 → LUMO+2	38.03
			231.72	HOMO-4 → LUMO	50.30

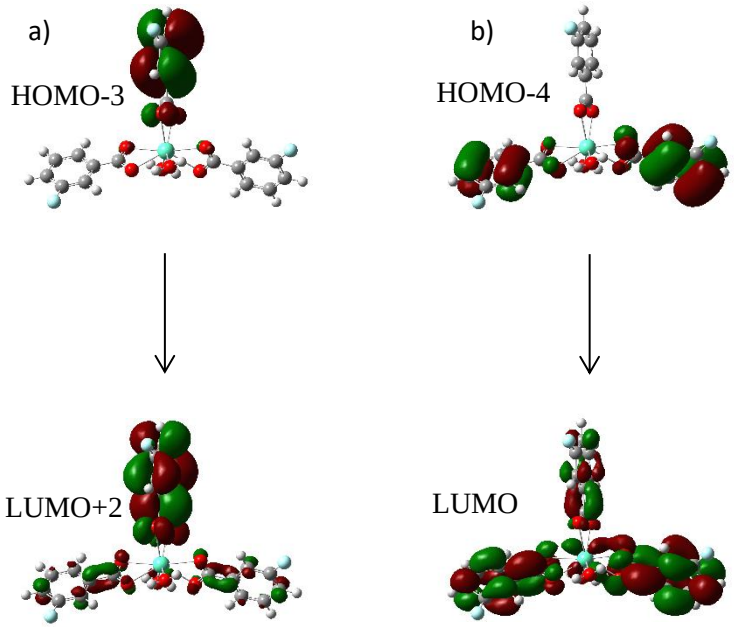

Figure 26. Major transitions in the EuFB1m1 complex for the 227.77 nm (a), and 228.82 nm (b) excited state. Green orbitals are the positive values of the wavefunction, while the red orbitals are the negative values.

3.1.3.13 EuFB1m2

For complex EuFB1m2, one major S_1 excited states were calculated (Table 24). The excited state absorbs at 231.73 nm presented a dominant transition between the HOMO-4 and LUMO orbitals (Figure 27).

Table 24. Major calculated excited states for the EuFB1m2 complex, including participating orbital transitions and percent contribution.

6-31G(d)			6-311+G(d,p)		
λ_{max} (nm)	**Orbitals**	**Contribution (%)**	**λ_{max} (nm)**	**Orbitals**	**Contribution (%)**
228.83	HOMO-4 → LUMO	50.06	231.73	HOMO-4 → LUMO	46.30

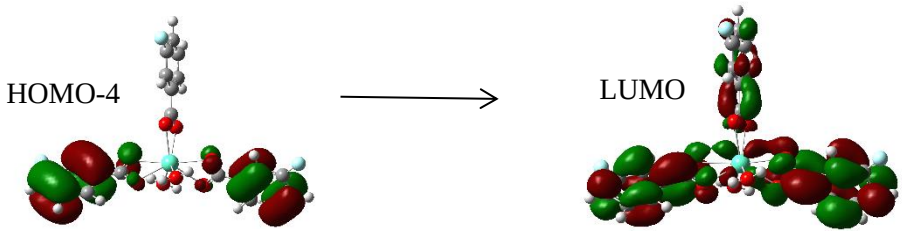

Figure 27. Major transitions in the EuFB1m2 complex for the 231.73 nm excited state. Green orbitals are the positive values of the wavefunction, while the red orbitals are the negative values.

3.1.3.14 EuFB1p

Complex EuFB1p presents two major S_1 excited states (Table 25). The first excited state with absorption at 238,02 nm presented a dominant transition between the HOMO-3 and LUMO orbitals and one dominant transition between the HOMO and LUMO+2 orbitals. The second excited state (239.08 nm) had a dominant transition between the HOMO-2 and LUMO (Figure 28).

Table 25. Major calculated excited states for the EuFB1p complex, including participating orbital transitions and percent contribution.

6-31G(d)			6-311+G(d,p)		
λ_{max} (nm)	Orbitals	Contribution (%)	λ_{max} (nm)	Orbitals	Contribution (%)
235.17	HOMO-1 → LUMO	79.34	238.02	HOMO-2 → LUMO	41.97
				HOMO → LUMO+2	35.77
			239.08	HOMO-2 → LUMO	61.32

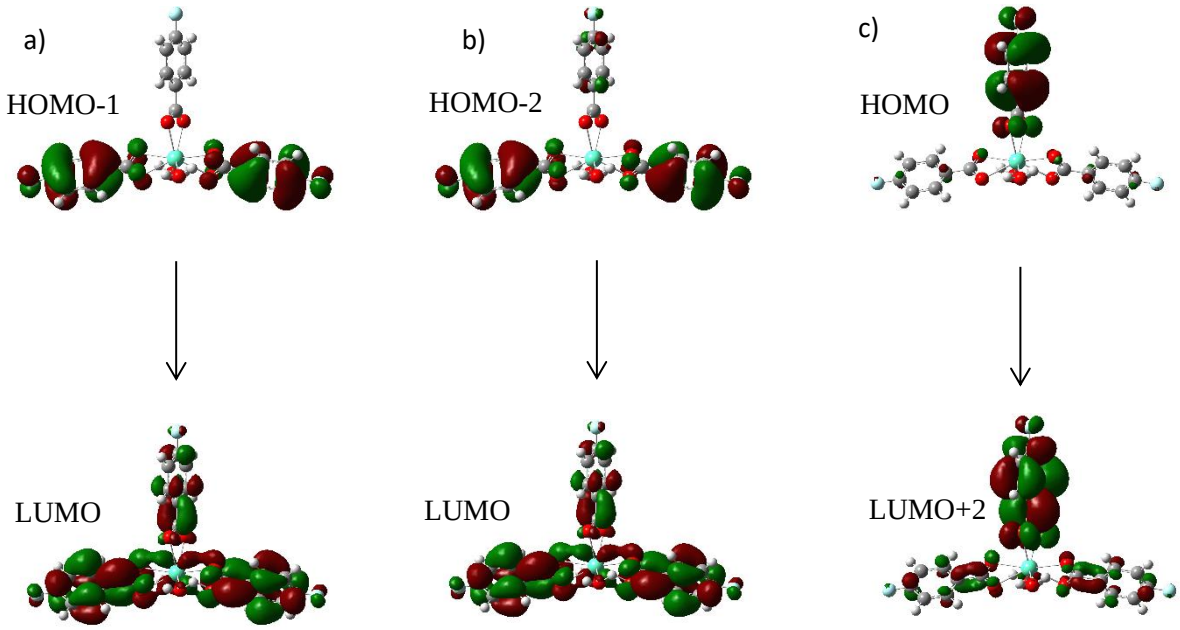

Figure 28. Major transitions in the EuFB1p complex for the 238.02 nm (a-b), and the 239.08 nm (c) excited states. Green orbitals are the positive values of the wavefunction, while the red orbitals are the negative values.

3.1.3.15 EuFB2(H_2O)$_2$

For complex EuFB2(H_2O)$_2$, two major S_1 excited states were calculated (Table 26). The first excited state with absorption at 231.5 nm presented a dominant transition between the HOMO-5 and LUMO orbitals. The second excited state with absorption at 238.94 nm had a dominant transition between the HOMO-2 and LUMO orbitals (Figure 29).

Table 26. Major calculated excited states for the EuFB2$(H_2O)_2$ complex, including participating orbital transitions and percent contribution.

6-31G(d)			6-311+G(d,p)		
λ_{max} (nm)	Orbitals	Contribution (%)	λ_{max} (nm)	Orbitals	Contribution (%)
236.4	HOMO-3 → LUMO	39.06	231.5	HOMO-5 → LUMO	32.22
239.58	HOMO-2 → LUMO	63.17	238.94	HOMO-2 → LUMO	45.86

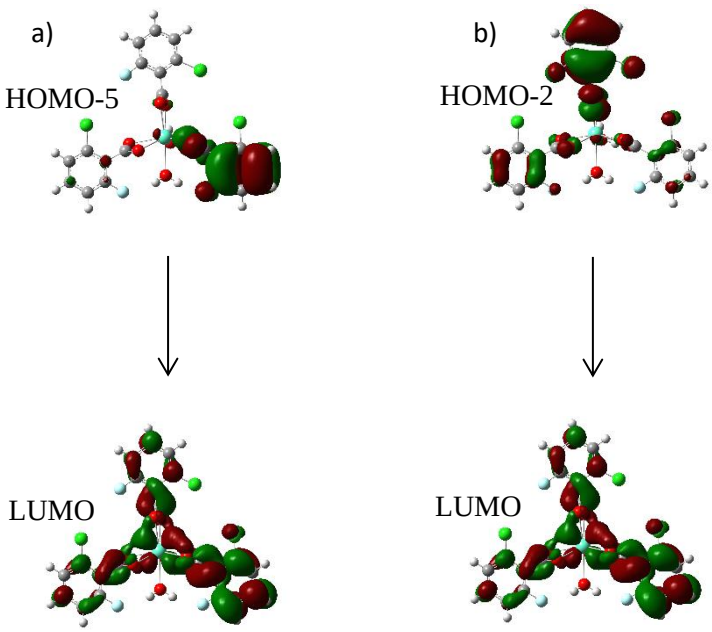

Figure 29. Major transitions in the EuFB2$(H_2O)_2$ complex for the 231.5 nm (a), and 238.94 nm (b) excited state. Green orbitals are the positive values of the wavefunction, while the red orbitals are the negative values.

3.1.3.16 EuFB6$(H_2O)_2$

For complex EuFB6$(H_2O)_2$, three major S_1 excited states were calculated (Table 27). The first excited state with absorption at 219.9 nm presented a dominant transition between the HOMO-6 and LUMO orbitals. The second excited state with absorption at 234.1 nm had a dominant transition between the

HOMO-5 and LUMO orbitals and the third excited state with absorption at 239.66 nm had a dominant transition between the HOMO-3 and LUMO+1 orbitals (Figure 30).

Table 27. Major calculated excited states for the EuFB6$(H_2O)_2$ complex, including participating orbital transitions and percent contribution.

	6-31G(d)			6-311+G(d,p)	
λ_{max} (nm)	**Orbitals**	**Contribution (%)**	**λ_{max} (nm)**	**Orbitals**	**Contribution (%)**
236.51	HOMO-5 → LUMO	45.16	219.9	HOMO-6 → LUMO	30.10
240.34	HOMO-3 → LUMO+2	29.34	234.1	HOMO-5 → LUMO	29.09
			239.66	HOMO-3 → LUMO+1	25.62

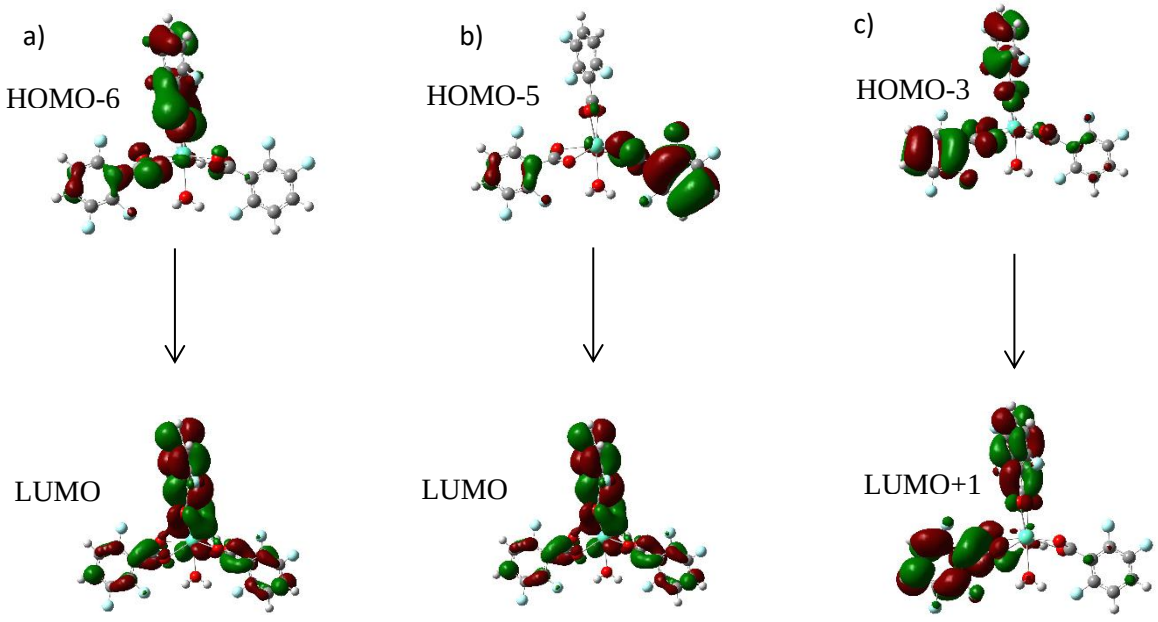

Figure 30. Major transitions in the EuFB6$(H_2O)_2$ complex for the 219.9 nm (a), the 234.1 (b), and the 239.66 nm (c) excited states. Green orbitals are the positive values of the wavefunction, while the red orbitals are the negative values.

3.1.3.17 EuFB9$(H_2O)_2$

Complex EuFB9$(H_2O)_2$ presents three major S_1 excited states (Table 28). The first excited state with absorption at 236.25 nm presented a dominant transition between the HOMO-4 and LUMO orbitals. The

second excited state (241.01 nm) had a dominant transition between the HOMO-5 and LUMO, while the third excited state with absorption at 246.88 nm presented a dominant transition between the HOMO-2 and LUMO orbitals (Figure 31).

Table 28. Major calculated excited states for the EuFB9(H_2O)$_2$ complex, including participating orbital transitions and percent contribution.

	6-31G(d)			6-311+G(d,p)	
λ_{max} (nm)	**Orbitals**	**Contribution (%)**	**λ_{max} (nm)**	**Orbitals**	**Contribution (%)**
223.5	HOMO-4 → LUMO+1	45.84	236.25	HOMO-4 → LUMO	40.69
241.89	HOMO-4 → LUMO	39.13	241.01	HOMO-5 → LUMO	33.43
247.31	HOMO-2 → LUMO	43.19	246.88	HOMO-2 → LUMO	52.53

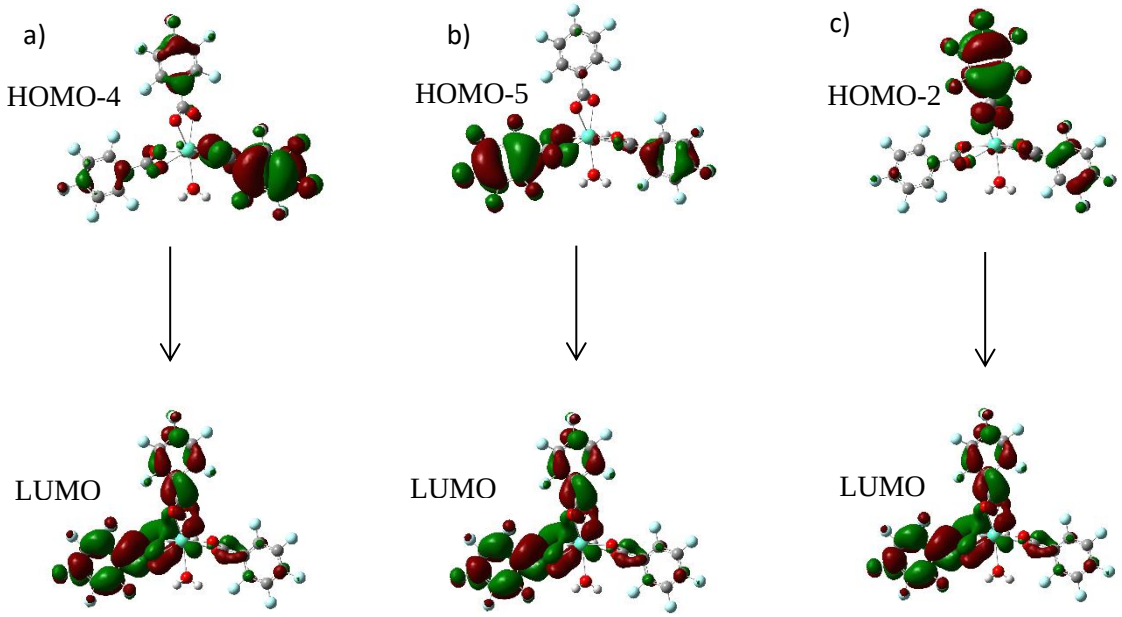

Figure 31. Major transitions in the EuFB9(H_2O)$_2$ complex for the 236.25 nm (a), the 241.01 nm (b), and the 246.88 nm (c) excited states. Green orbitals are the positive values of the wavefunction, while the red orbitals are the negative values.

3.1.4 Singlet, Triplet, ISC and ET

The experimentally determined luminescent quantum yields of the modeled complexes are highly influenced by the nature of the substituents in the benzoic acid ring. Consequently, variations in the luminescent quantum yield can be related to cause variations in the energy gap between the lowest singlet (S_1) and triplet (T_1) levels (ISC) and the energy gap between the lowest triplet levels and the Eu^{3+}-based $^5D_0$ level (ET). The Eu^{3+}-based $^5D_0$ level is constant for all complexes due to the diminished ligand field effects of lanthanide metal-ligand bonding and it has an energy of 17300 cm^{-1} (2.1449 eV)[64–66]. Here, we will explore how the position and number of substituents affect the S_1 and T_1 levels as well as the ISC and ET energy gaps. Overall, minor changes of energies were seen for the T_1 levels, while the S_1 levels showed more pronounced changes in energies. For most of the complexes studied, ET gaps have considerably higher energies than the ISC gap except for EuFB8 and EuTTA which present a higher ISC gap and lower ET gaps.

3.1.4.1 Changing number and position of substituents on fluorobenzoate ligands

The calculated S_1 and T_1 energies for the complexes in Kalyakina et al. and for EuTTA are reported in Table 29 and plotted in Figure 32. Comparing the S_1 and T_1 levels and the ISC and ET gaps from the fluorobenzoate complexes, it was found that they are not related to the degree of fluorination of the ligands but are more effected by the position of the substituents in the benzoic acid ring.

S_1 and T_1: the highest S_1 and T_1 energies belong to the EuFB2 (4.9616 and 3.6278 eV, respectively) while the lowest energies were found in EuTTA (3.3322 eV and 2.4539 eV). For the fluorobenzoate ligands, the lowest energies were found in EuFB8 (3.8221 eV and 2.8321 eV). When adding a fluorine substituent in the ortho position resulted in an increase of S_1 and T_1 energies. This behavior can be observed between EuFB3 (S_1 = 4.5191 eV, T_1 = 3.4943 eV) and EuFB6 (S_1 = 4.6413 eV, T_1 = 3.6130 eV) where it produced energy changes of ΔE_{S1} = +0.1222 eV and ΔE_{T1} = +0.1187 eV. Adding a fluorine substituent in the meta position causes a large decrease in the S_1 energy and a small decrease in the T_1 energy like seen between EuFB1 (S_1 = 4.7388 eV, T_1 = 3.5774 eV) and EuFB3 (S_1 =

4.5191 eV, T_1 = 3.4943 eV) where changes of -0.2197 eV and -0.0831eV can be observed in the S_1 and T_1 levels, respectively. On the other hand, adding a fluorine substituent to the para position causes a significant increase in S_1 energies and small increase in T_1 energies, like seen between EuFB1 (S_1 = 4.7388 eV, T_1 = 3.5774 eV) and EuFB4 (S_1 = 4.8968 eV, T_1 = 3.6015 eV). Between these two complexes, it can be observed a change in S_1 energies of +0.1580 eV and a change in T_1 energies of +0.0241 eV. Comparing complexes EuFB1 (S_1 = 4.7388 eV, T_1 = 3.5774 eV) and EuFB2 (S_1 = 4.9616 eV, T_1 = 3.6278 eV), it was found that adding a chlorine substituent in the ortho position causes similar effects to a fluorine substituent (ΔE_{S1} = +0.2228 eV and ΔE_{T1} = +0.0504 eV) but with different magnitude. With a chlorine substituent the change in S_1 energy is almost doubled and the change in T_1 is halved compared to the changes with a fluorine substituent. Finally, when a nitro group is substituted to fluorine in the ortho position like between compounds EuFB9 (S_1 = 4.6840 eV, T_1 = 3.5798 eV) and EuFB8 (S_1 = 3.8221 eV, T_1 = 2.8321 eV), it was observed significant decrease in the energy of both $S_1$and T_1 levels (-0.8619 eV and 0.7473 eV, respectively). Both in the case of EuFB8 and EuTTA, their S_1 energies are comparable with the T_1 energies of the other complexes, while their T_1 levels are closer to $^5D_0$ level of europium.

ISC and ET gaps: the highest ISC and ET gaps were calculated for EuFB2 (1.1614 and 1.14325 eV, respectively), while the lowest overall ISC and ET gaps were collected for EuTTA (0.8783 and 0.3090 eV). The trends for ISC and ET gaps follow the same trends as S_1 and T_1. For the fluorobenzoate ligands, the lowest ISC and ET gaps were recorded for EuFB8, and they have energies of 0.9900 and 0.3672 eV, respectively. By comparing the EuFB3 (ISC = 1.0248 eV, ET = 1.3494 eV) and EuFB6 (ISC = 1.0283 eV, ET = 1.4681 eV) complexes, it was found that adding a fluorine substituent in the ortho position causes an increase in energy for both ISC and ET gaps, +0.0035 eV and +0.1187eV, respectively. Adding a fluorine substituent to the meta position causes a large decrease in the energies of ISC and ET gaps. This can be seen when comparing complexes EuFB1 (ISC = 1.1614 eV, ET = 1.4325 eV) and EuFB3 (ISC = 1.0248 eV, ET = 1.3494 eV), where changes of -0.1366 eV for ISC and -0.0831 eV for ET. Adding a fluorine substituent to the para position causes an energy increase of +0.0241 eV for ISC and +0.1339 eV for ET in complexes EuFB1 (ISC = 1.1614 eV, ET = 1.4325 eV) and EuFB3 (ISC = 1.2953

eV, ET = 1.4566 eV). When changing a fluorine with a chlorine in the ortho position like in complexes EuFB1 (ISC = 1.1614 eV, ET = 1.4325 eV) and EuFB2 (ISC = 1.3338 eV, ET = 1.4566 eV) it was found that the ISC energy increases by 0.1724 eV and ET increases by 0.0504 eV. Finally, when changing an ortho fluorine substituent with a nitro group like between complexes EuFB9 (ISC = 1.1046 eV, ET = 1.4345 eV) and EuFB8 (ISC = 0.9900 eV, ET = 0.3090 eV), it was found that both ISC and ET gaps show a large decrease in energy (-0.1146 eV and -1.1255 eV, respectively).

Table 29. S_1, T_1 energies, ISC and ET gaps for the fluorobenzoate complexes and the EuTTA complex using both the 6-31G(d) and the 6-311+G(d,p) basis sets.

Complexes	**6-31G(d)**				**6-311+G(d,p)**			
	S_1 (eV)	**T_1 (eV)**	**ISC (eV)**	**ET (eV)**	**S_1 (eV)**	**T_1 (eV)**	**ISC (eV)**	**ET (eV)**
EuFB1	4.7415	3.5573	1.1842	1.4124	4.7388	3.5774	1.1614	1.4325
EuFB2	4.8345	3.5875	1.2470	1.4426	4.9616	3.6278	1.3338	1.4829
EuFB3	4.5329	3.4646	1.0683	1.3197	4.5191	3.4943	1.0248	1.3494
EuFB4	4.9216	3.5947	1.3269	1.4498	4.8968	3.6015	1.2953	1.4566
EuFB5	4.6791	3.4921	1.1870	1.3472	4.7419	3.5391	1.2028	1.3942
EuFB6	4.6066	3.5950	1.0116	1.4501	4.6413	3.6130	1.0283	1.4681
EuFB7	4.6493	3.4890	1.1603	1.3441	4.6743	3.5195	1.1548	1.3746
EuFB8	3.7867	2.7371	1.0496	0.5922	3.8221	2.8321	0.9900	0.6872
EuFB9	4.6109	3.5508	1.0601	1.4059	4.6840	3.5794	1.1046	1.4345
EuTTA	3.3466	2.4478	0.8988	0.3029	3.3322	2.4539	0.8783	0.3090

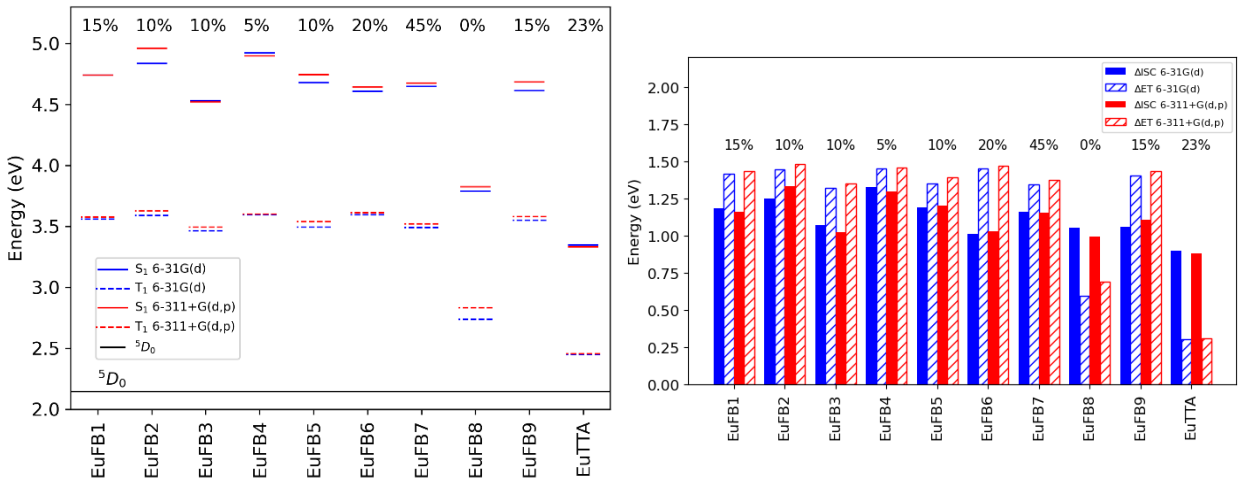

Figure 32. S_1 and T_1 energies (left), ISC and ET gaps (right) for fluorobenzoate ligands reported in Kalyakina et al. and for EuTTA calculated using both the 6-31G(d) and the 6-311+G(d,p) basis sets.

3.1.4.2 Moving a single fluorine atom around the ring of a benzoate ligand

The calculated S_1 and T_1 energies along with the ISC and ET gaps for this new set of complexes are listed in Table 30 and plotted in Figure 33. Contrary to the previous set of complexes, it was noticed that the same trends observed in the changes of S_1 and T_1 were shared by the change in ISC and ET gaps.

When moving the fluorine substituent from one ortho position to the other, such as in complexes EuFB1o1 and EuFB1o2, it was found that all energies increased but with different magnitudes. For the S_1 and T_1 energies, changes of +0.0470 eV and +0.0094 eV were recorded, respectively. For the ISC and ET gaps the recorded changes were +0.0376 eV and +0.0099 eV, respectively. Comparing complexes EuFB1m1 and EuFB1m2, it was found that moving one fluorine substituent from one meta position to the other causes negligible changes in energies for S_1 and T_1 levels as well as the ISC and ET gaps. Specifically, the S_1 levels presented a change of -0.0039 eV, the T_1 level presented a change of -0.0013 eV, the ISC gap showed a change of -0.0026 eV and the ET gap showed a changed of -0.0013 eV. Finally, when moving the fluorine substituent from the ortho to the meta and then to the para position, the S_1 and the ISC gaps increased, while the T_1 and ET gap decreased. When going from the ortho

(EuFB1o1) to the meta position (EuFB1m1), changes of +0.0037 and +0.0468 eV were observed for the S_1 level and ISC gap, respectively. For the T_1 level and the ET gap, changes of -0.0431 and -0.0485 eV were observed. When going from the ortho to the para position (EuFB1p), changes of +0.2505 and +0.3184 eV for the S_1 level and ISC gap as well as changes of -0.0679 eV for both the T_1 level and the ET gap were recorded.

Table 30. S_1, T_1 energies and ISC, ET gaps for the complexes obtained by moving a fluorine atom around the ring of a benzoate ligand calculated using both the 6-31G(d) and the 6-311+G(d,p) basis sets.

Complexes	6-31G(d)				6-311+G(d,p)			
	S_1 (eV)	**T_1 (eV)**	**ISC (eV)**	**ET (eV)**	**S_1 (eV)**	**T_1 (eV)**	**ISC (eV)**	**ET (eV)**
EuFB1o1	4.7415	3.5573	1.1842	1.4124	4.7388	3.5774	1.1614	1.4325
EuFB1o2	4.7342	3.5572	1.1770	1.4123	4.7858	3.5868	1.1990	1.4419
EuFB1m1	4.7761	3.5162	1.2599	1.3713	4.7425	3.5343	1.2082	1.3894
EuFB1m2	4.7724	3.5149	1.2575	1.3700	4.7386	3.5330	1.2056	1.3881
EuFB1p	5.0825	3.5405	1.5420	1.3956	4.9893	3.5095	1.4798	1.3646

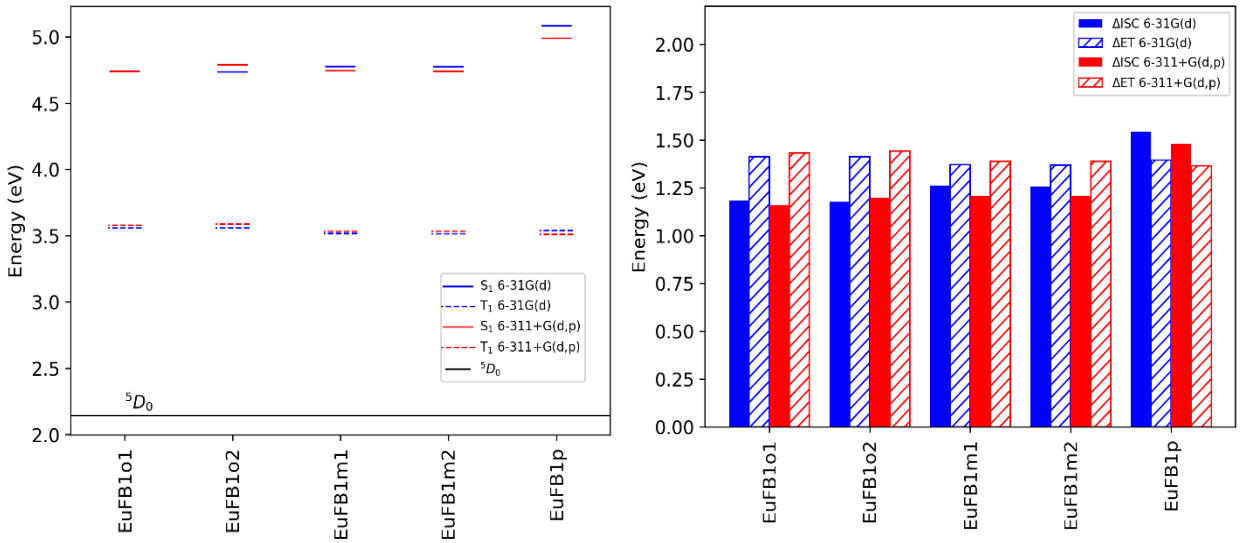

Figure 33. S_1 and T_1 energies (left), ISC and ET gaps (right) calculated using both the 6-31G(d) and the 6-311+G(d,p) basis sets for the complexes obtained by moving a single fluorine atom around a benzoate ring.

3.1.4.3 Changing the number of coordinated water molecules

The energies of the S_1 and the T_1 energy levels as well as the energies of the ISC and ET gaps are reported in Table 31 and plotted in Figure 34. For this class of compounds, the changes in energies seem to be influenced by the number of fluorine substituents. Specifically, the smaller the number of substituents, the smaller the magnitude of the change, while a higher number of substituents causes more drastic change in energies. Between EuFB2$(H_2O)_2$ and EuFB2(H_2O) which contain two substituents, the S_1 and T_1 energies showed a change of -0.0135 eV and -0.0092 eV, respectively, while changes of -0.0043 and -0.0092 eV were observed for ISC and ET gaps. Comparing EuFB6$(H_2O)_2$ and EuFB6(H_2O) which contains e substituents , changes in the S_1 and T_1 energies of -0.0266 eV and +0.0002 eV changes in ISC and ET of -0.0268 eV and +0.0002 eV were recorded. Finally, when comparing complexes with five substituents (EuFB9$(H_2O)_2$ and EuFB9(H_2O)), the energies changes observed corresponded to -0.0685 eV for the S_1 levels, -0.0163 eV for the T_1 level, -0.0522 eV for the ISC gap and -0.0163 eV for the ET gap.

Table 31. S_1, T_1 energies and ISC, ET gaps for the monohydrate and dihydrate complexes calculated using both the 6-31G(d) and the 6-311+G(d,p) basis sets.

Complexes	**6-31G(d)**				**6-311+G(d,p)**			
	S_1 (eV)	**T_1 (eV)**	**ISC (eV)**	**ET (eV)**	**S_1 (eV)**	**T_1 (eV)**	**ISC (eV)**	**ET (eV)**
EuFB2$(H_2O)_2$	4.9195	3.5945	1.3250	1.4496	4.9751	3.6370	1.3381	1.4921
EuFB2(H_2O)	4.8345	3.5875	1.2470	1.4426	4.9616	3.6278	1.3338	1.4829
EuFB6$(H_2O)_2$	4.6296	3.5981	1.0315	1.4532	4.6679	3.6128	1.0551	1.4679
EuFB6(H_2O)	4.6066	3.5950	1.0116	1.4501	4.6413	3.6130	1.0283	1.4681
EuFB9$(H_2O)_2$	4.6532	3.563	1.0902	1.4181	4.7525	3.5957	1.1568	1.4508
EuFB9(H_2O)	4.6109	3.5508	1.0601	1.4059	4.6840	3.5794	1.1046	1.4345

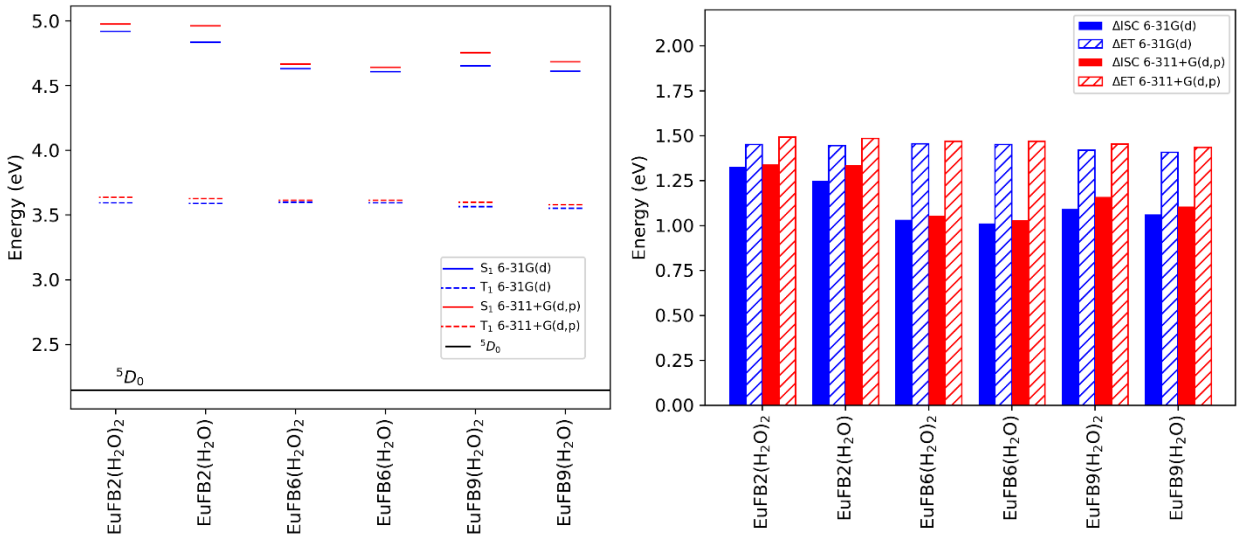

Figure 34. S_1 and T_1 energies (left) and ISC and ET gaps (right) calculated using both the 6-31G(d) and the 6-311+G(d,p) basis sets for the monohydrate and dihydrate complexes.

3.1.4.4 Effects of the changing dihedral angle in the fluorobenzoate ligands

Comparing the DFT-calculated dihedral angles the fluorobenzoate ligands in Kalyakina et al. to the respective S_1 and T_1 energies, the effects of conjugation over the benzene-carboxylate system on those energies can be identified. Similarly to the HOMO and LUMO energies, no trends between the dihedral angles and S_1 and T_1 energies in those europium complexes was found (Figure 35). As the dihedral angle increased from 0.889° (EuFB5) to 76.796° (EuFB2), the S_1 and T_1 energies remained similar to one another suggesting that conjugation does not significantly contributes to the energies of the singlet and triplet energies and therefore the ISC and ET gaps.

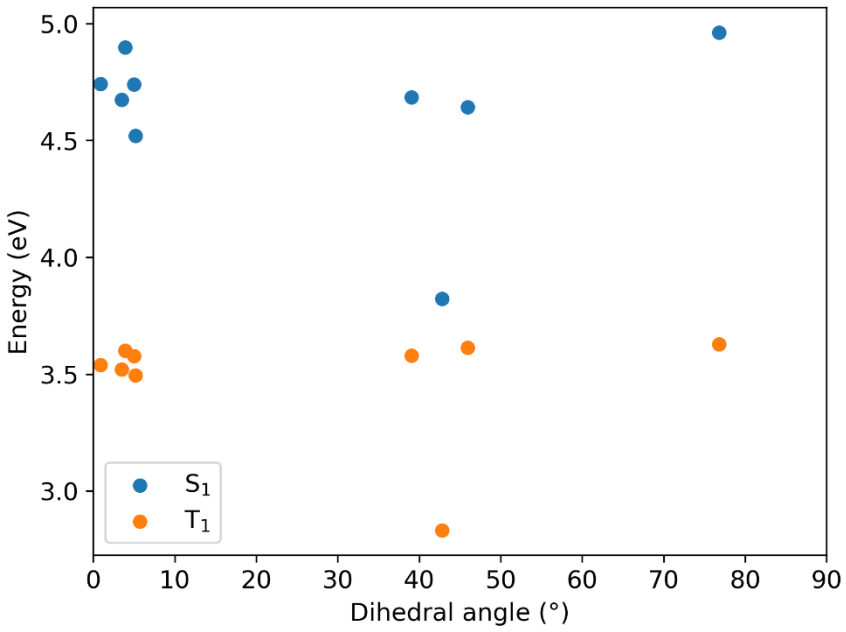

Figure 35. S_1 (blue) and T_1 (orange) energies plotted against the dihedral angle of the complexes in Kalyakina et al.

3.1.5 ISC, ET, Dihedral Angles and Luminescent Quantum Yield

Previous studies have shown that luminescent quantum yields of Eu^{3+} metal complexes are strongly related to the triplet state energies of the ligands[67]. This suggests that the luminescent quantum yield, while as a function of both ISC and ET gaps, is more sensitive to change in ET than ISC. Furthermore, an empirical rule indicated that ET gap must be larger than 0.43 and ISC gap must be larger than 0.65 eV[68]. The calculated energy gaps are reported in Table A1 and plotted in Figure 36. In Kalyakina et al, the highest recorded quantum yield (Φ = 45%) belonged to the EuFB9 complex, for that reason we assume that the ISC (1.1548 eV) and ET (1.3746 eV) gaps of this complex are close to the optimal values for efficient energy transfer. Comparing the ET gap of EuFB7 (Φ = 45%) to the ET gaps of the other modeled complexes, it was observed that the small increase (+0.0196 eV) in ET energy of EuFB5 (Φ = 10%) and the small decreases (-0.0252 eV) in ET energy of EuFB3 (Φ = 10%) cause decrease of over 30% of the luminescent quantum yield. Comparable results can be seen when the ISC between complexes are extremely similar to one another, and the ET energies are considerably different like in

complex EuFB1 and EuFB7. The low luminescent quantum yield of EuFB1 (Φ=15%, ISC = 1.1614eV, ET = 1.4325 eV) compared to EuFB7 (Φ = 45%, ISC = 1.1548 eV, ET = 1.3746 eV) can be attributed to the larger ET gap, since the difference between ISC gaps for both compounds is minimal (ΔISC = -0.0066 eV). Two processes can be speculated to take part in the decrease of luminescent quantum yield. One takes part when the ET gap is larger than the ideal value and, in this case, the large energy difference between the T^1 state of the ligand and the $^5D_0$ level of the Eu^{3+} causes the energy to preferentially decay through non-radiative pathways. Opposite, when the ET gap is smaller than ideal, energy back transfer can happen between the $^5D_0$ level and the T_1 excited electronic state. An example of this last mechanism could be the complex EuFB8, where the extremely small ET gap could cause energy back transfer[69,70] and prevent emission from happening.

However, it was also observed that in some of the studied complexes when the ET gaps were significantly different from the ideal values, a discrete luminescent quantum yield was still observed. For example, in EuFB6 (Φ = 20%, ISC = 1.0283 eV, ET = 1.4681 eV) the ET gap shows a significant increase (+0.0935 eV) compared to the ET of EuFB7, but the complex still retains a luminescent quantum yield of 20%. Similarly, EuFB2 has an ET gap larger then EuFB3 (+0.1.335 eV) but maintains the same luminescent quantum yield (Φ = 10%). This suggests that while the luminescent quantum yield of Eu^{3+} complexes is extremely sensitive to changes in ET, other variable such as the ISC gap cannot be ignored when describing the energy transfer efficiency of these complexes.

Comparing the dihedral angles of the complexes to the respective quantum yields it was noticed that while the dihedral angle is low (<10°) a large variation in luminescent quantum yield was recorded (from 45% to 5%). As the dihedral angle increases, both the variation in luminescent quantum yield and the luminescent quantum yields themselves decrease (Figure 37). This suggests that, while dihedral angles do not directly affect the ISC and ET gaps, they could affect the efficiency of the energy transfer, whit high dihedral angles significantly reducing the efficiency and therefore the luminescent quantum yields.

Finally, taking into consideration the luminescent quantum yield of the EuTTA complex (Φ = 23%) as well as its ISC and ET gaps (0.8783 eV and 0.3090 eV, respectively) and comparing it to the ones of the EuFB7 complex (Φ = 45%, ISC = 1.1548 eV, ET = 1.3746 eV), it can be inferred that different ideal ISC and ET values exist for each category of ligands. Benzoate ligands (FB7) and β-diketonate ligands (TTA) have vastly different structures and binding modalities that each have their own specific energy transfer characteristic and therefore each would require different ideal ISC and ET gaps.

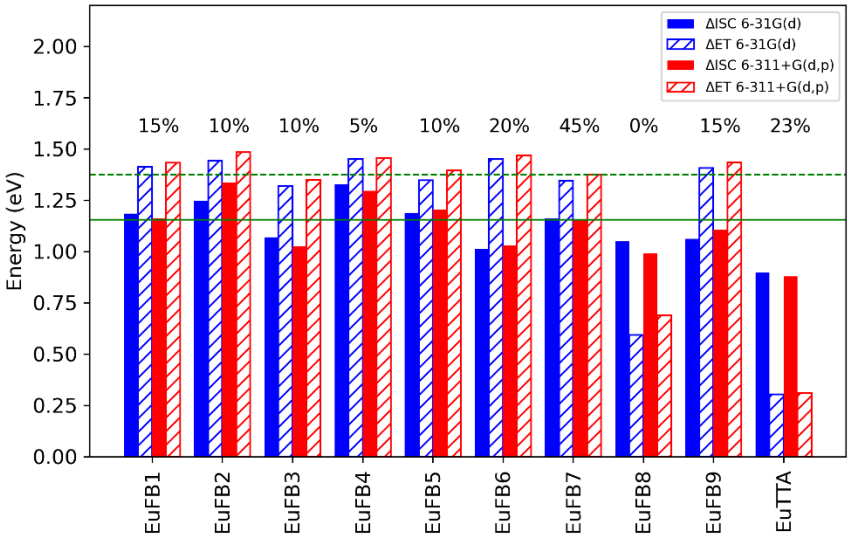

Figure 36. Calculated ISC and ET energy gaps for the complexes in Kalyakina et al. with experimental quantum yields. The solid and dashed green lines represent the ideal values for ISC and ET as seen in the FB7 complex.

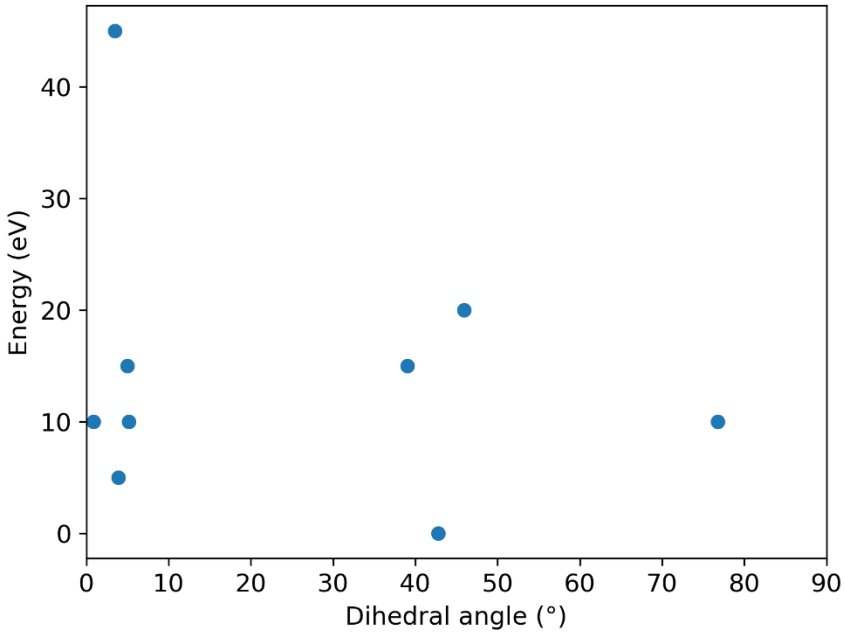

Figure 37. Experimental quantum yield plotted against the dihedral angle of the complexes in Kalyakina et al.

3.2 Experimental Studies

3.2.1 Synthesis of the Nanoparticles

Our synthetic method followed a thermal decomposition approach to make nanoparticles. Ca-EDTA and Eu-EDTA precursors were formed during the reaction between $CaCl_2$, $EuCl_3$ and Na_2EDTA in solution. Based on our previous studies, a pH of 6 is ideal for this process[32]. When the precursor metal EDTA complexes are heated using microwave radiation, the complexes decompose slowly releasing Ca^{2+}, Eu^{3+} into the aqueous solution. Microwave radiation also induces the release of F^- ions from $NaBF_4$ allowing the nucleation and the precipitation reaction to proceed. At the same time, the free EDTA molecules in the solution act as a surfactant and coordinate to the surface-bound unsaturated metal ions in the nanoparticles. The slow release of metal ions and the presence of a surfactant both help control the growth of the nanoparticles. The reaction successfully produced 10% Eu:CaF_2 nanoparticles in both scales. The

small-scale reactions had a yield of 58.74 ± 0.01 mg while large-scale reaction had a yield of 399.17 ± 0.01 mg.

3.2.2 Size, Morphology and Composition

The powder X-ray diffraction pattern of 10% Eu:CaF_2 nanoparticles synthesized using small-scale reaction (Figure 38) shows four distinct peaks that are consistent with body-centered cubic crystal structure of CaF_2[32,35,71]. The diffraction pattern of large-scale 10% Eu:CaF2 show three distinct peaks with the fourth one missing due to low signal intensity and high signal-to-noise ratio. The crystallite size for the Eu-doped nanoparticles obtained from the Scherrer equation using the peak at 46.8° was calculated to be 6.9 nm for small scale reactions and 10.8 nm for the large-scale reaction. Compared to undoped nanoparticles, the Eu-doped nanoparticles exhibit a peak downward shift of -0.02° for the peak centered at 28.1° and -0.19° for the peak centered at 46.8° which is consistent with previous studies[32]. This results and previous studies[32,36], show that europium doping does not significantly change the crystal structure of CaF_2.

DLS size distribution for small scale reaction (Figure 39a) revealed that the small-scale nanoparticles were homogeneous in size with an average particle size of 80.2 ± 0.1 nm and PdI of 0.11 ± 0.03, while the large-scale nanoparticles (Figure 39b) had an average particle size of 472 ± 8 nm and a PdI of 0.24 ± 0.01. SEM imaging of the nanoparticles prepared using the small-scale reaction (Figure 40) shows that the nanoparticles have a smaller size of about 40 nm compared to the DLS measurements. The higher particle sizes measured using DLS compared to SEM could be explained by the nanoparticles forming agglomerates when dispersed in water.

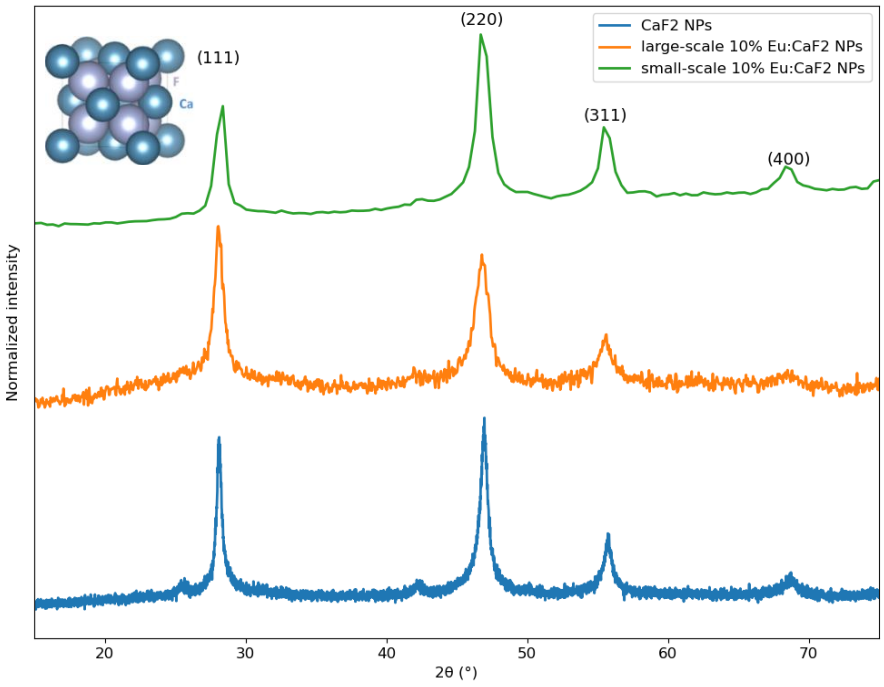

Figure 38. Powder XRD pattern of undoped CaF_2 (blue), large-scale 10% Eu:CaF_2 (orange) and small-scale 10% Eu:CaF_2 (green) nanoparticles. For CaF_2 peaks appear at 28.12°, 46.97°, 55.76° and 68.83°. For both small and large scale 10% Eu:CaF_2 peaks appear at 28.14°, 46.78°, 55.50° and 68.41°.

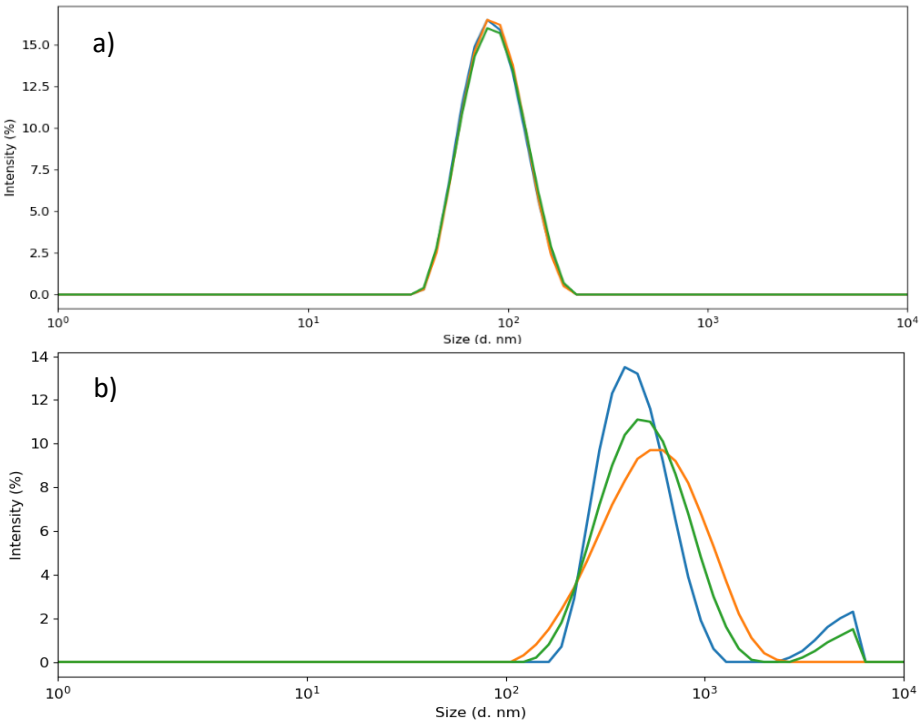

Figure 39. Size distribution obtained using DLS of a) small-scale and b)large-scale Eu:CaF2 nanoparticles. The small-scale reaction had an average particle size of 80.2 ± 0.1 nm and PdI value of 0.11 ± 0.03, while the large-scale reaction had an average particle size of 472 ± 8 nm and a PdI value of 0.24 ± 0.01.

The difference between the crystallite size (6.9 nm for small-scale and 10.8 nm for large-scale reactions) and the particle size (80.2 nm for small-scale and 472 nm for large-scale reactions) suggests that the synthesized nanoparticles are composed of small crystalline spheres fused together. This is further supported by SEM imaging (Figure 40). The small-scale nanoparticles have a flour-like shape: they are round and have small protrusion on the surface which can be explained by the irregular arrangement of the small crystalline subunits. In Figure 40b, the oriented-dark field image shows both bright and dark spots in the same nanoparticle. This is an indication that the mutliple crystalline subunits of different orientations are present in the same nanoparticle further supporting the idea that the nanoparticles are composed of smaller crystalline subunits. EDS mapping (Figure 41), confirms the theoretical elemental

composition of the nanoparticles and shows the homogeneous distrubution of Ca, Eu and F elements throughtout the nanoparticles.

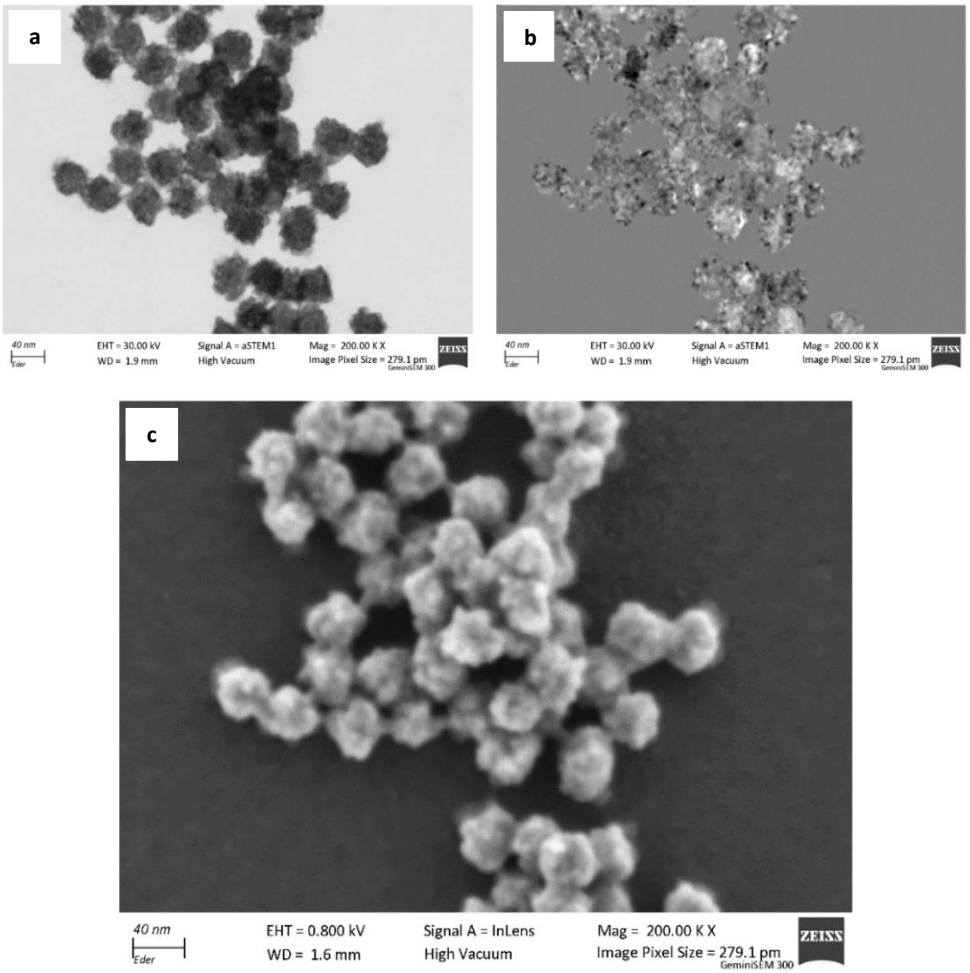

Figure 40. SEM images of small-scale Eu:CaF2 nanoparticles in a) bright-field mode, b) oriented dark field mode and c) surface topography mode. The nanoparticle size is around 40-50 nm in diameter with flour-like shape.

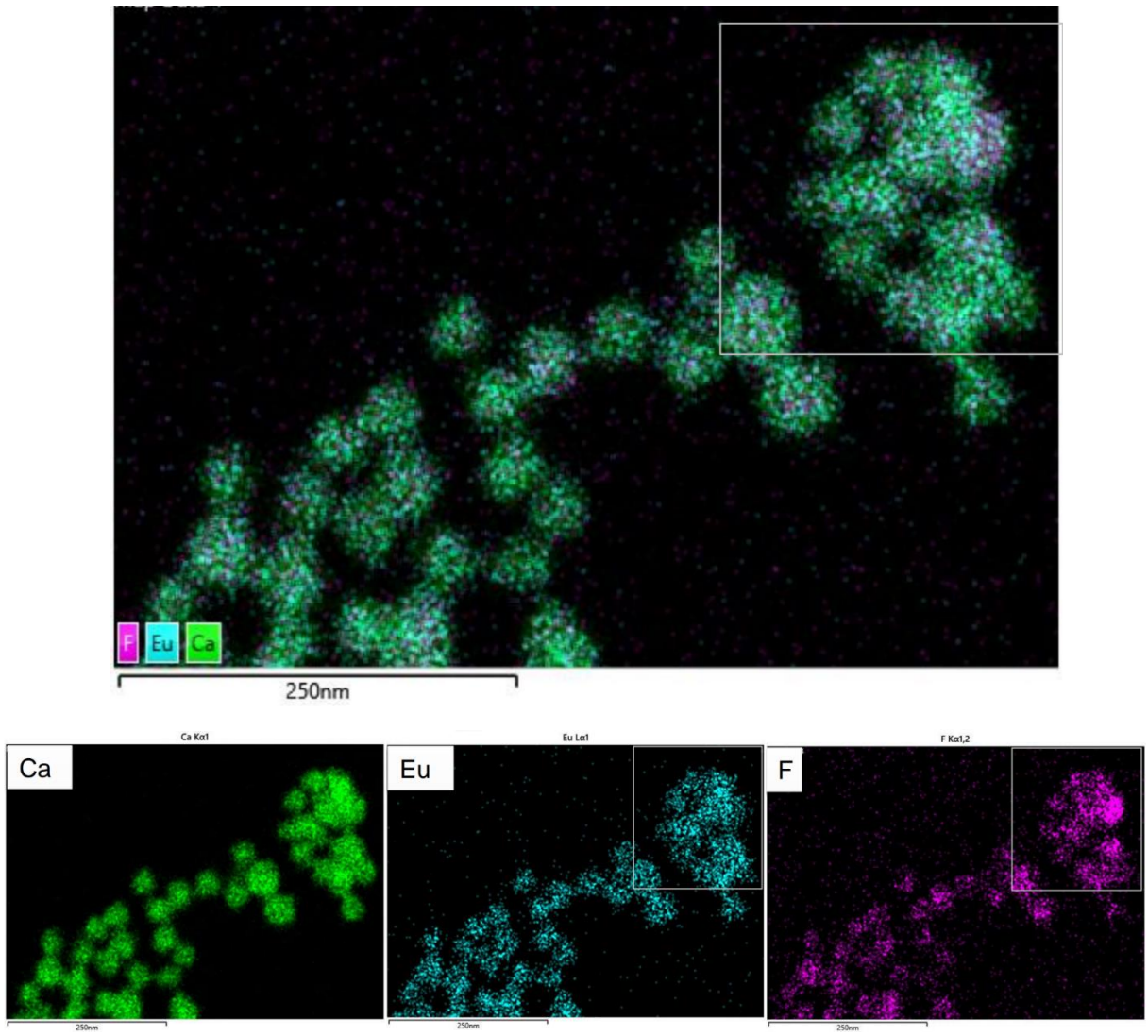

Figure 41. EDS mapping of Eu:CaF_2 nanoparticles with layered image (top) and individual elemental mapping for Ca, Eu and F elements (bottom).

3.2.3 Ligand Exchange

FT-IR analysis of the nanoparticles and their surface coatings (Figure 42) revealed that the coating exchange reaction was successful in replacing some EDTA molecules with TTA molecules. The surface of the uncoated nanoparticles presents evidence of EDTA: the band at 1602 cm^{-1} corresponds to the asymmetric stretching mode of COO^- [72] and the absorption at 1414 cm^{-1} correspond to the symmetric stretching mode of COO^- [72], these bands can be found at 1608 and 1393 cm^{-1} in the free EDTA spectrum,

respectively. The TTA coated nanoparticles present evidence of TTA. The absorption at 792 cm^{-1} correspond to the out-of-plane bending mode of CH_{α} coupled with the out-of-plane ring deformation of the thiophene group[73], which appears at 802 cm^{-1} in the free TTA spectrum. The large band between 1098-1056 cm^{-1} in the TTA coated nanoparticles was assigned to the ring breathing mode of the ring that forms when the β-diketonate ion chelates to europium[73]. The band at 1112 cm^{-1} in the uncoated nanoparticles could not be assigned to any EDTA or metal-EDTA vibrations. The difference in frequencies and shapes between the bands in the reference spectra and the nanoparticle spectra can be attributed to effects of metal chelation to EDTA and TTA[72].

As the TTA coating ratio increases, the bands at 1602-1591 and 1414 cm^{-1} (Figure 43a) decrease in absorbance while the band at 792 cm-1 (Figure 43b) increases. This suggests that as TTA coating ratios increase, more EDTA is displaced by the TTA in solution. This can be further supported by the appearance of a shoulder in the bands at 1602-1591 cm^{-1} as TTA increases. The increasing shoulder appears at a frequency of 1624 cm^{-1}, which corresponds to the antisymmetric stretching mode of C=C-C=O in TTA[73] (1633 cm^{-1} in the TTA reference spectrum).

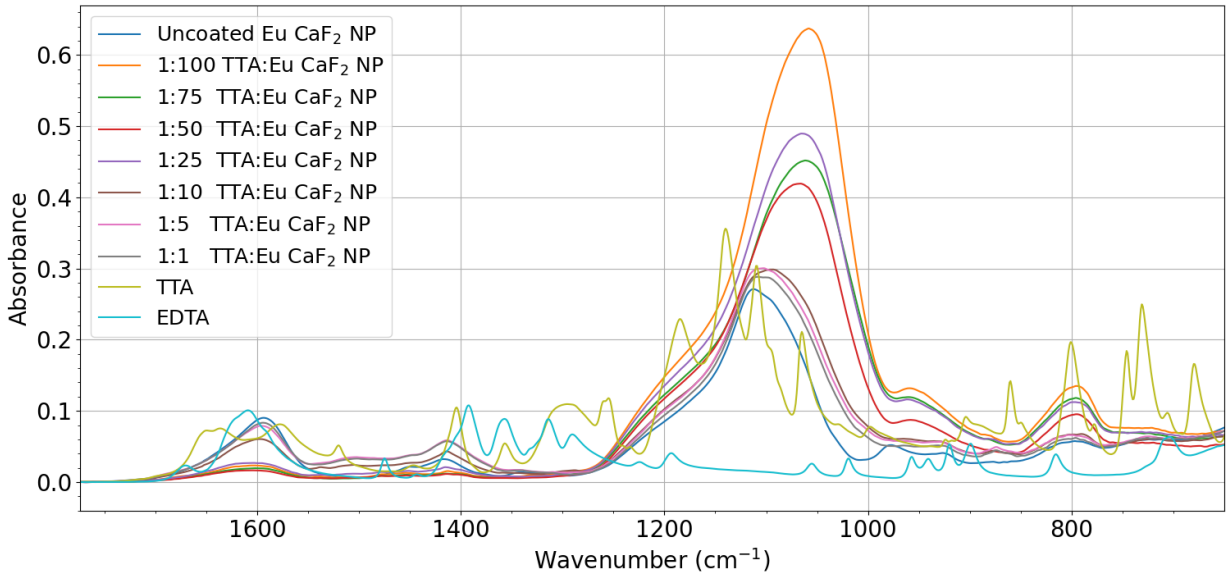

Figure 42. FT-IR spectra of uncoated 10% Eu:CaF2 nanoparticles, coated Eu:CaF_2 nanoparticles and reference spectra of Na_2EDTA and TTA.

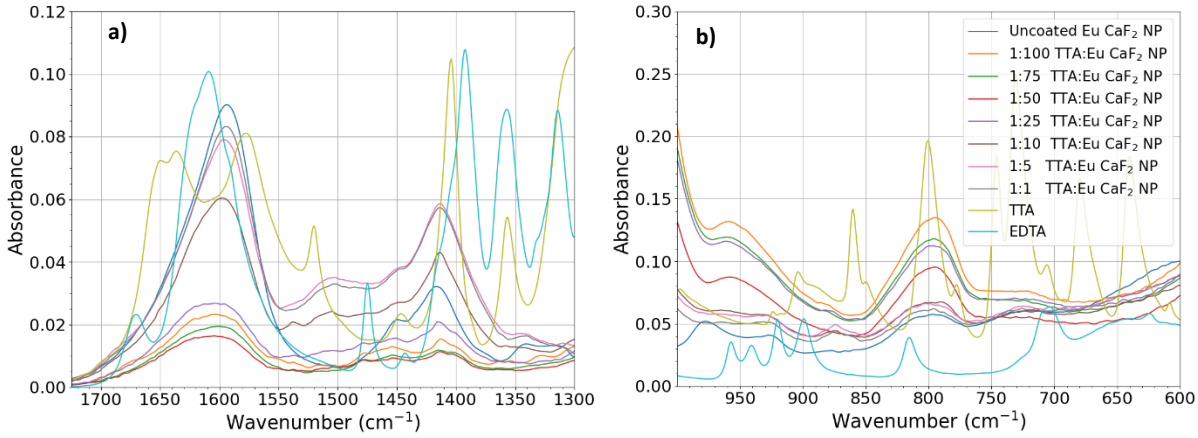

Figure 43. Magnification of the FT-IR spectra between a) 1750-1300 cm^{-1} and b) 1000-600 cm^{-1}. Both figures share the same legend. Decreasing bands at 1602-1591 cm^{-1}, corresponding to COO^- antisymmetric stretch, and at 1414 cm^{-1}, corresponding to COO^- symmetric stretch, suggest the decrease in EDTA at the surface of the nanoparticles as the TTA ratio increases. The appearance of the shoulder at 1624 cm^{-1}, corresponding to antisymmetric stretch of C=C-C=O, suggests the increase of TTA on the surface of the nanoparticles. The increase of the band at 792 cm^{-1} which corresponds to the out-of-plane bending mode of CH_α coupled with the out-of-plane ring deformation of the thiophene group suggests the increase of TTA on the surface of the nanoparticle.

UV-Vis absorption spectra of TTA, uncoated nanoparticles and TTA-coated nanoparticles were compared. The spectrum of free TTA (Figure A25) shows a maximum absorption peak (λ_{max}) at 316 nm with a second band at 207 nm. The former band seems to be composed of multiple unresolved bands at 268, 297 and 354 nm. The uncoated nanoparticles showed no absorption until the far-UV as seen in previous studies[32]. The absorption spectrum of TTA-coated nanoparticles shown reveals a λ_{max} at 341 nm and a second absorption peak at 258 nm (Figure 44). The blue shift in λ_{max} observed in TTA-coated nanoparticles compared to free TTA is consistent with the red shift that happens when a ligand is coordinated to a metal-center[74,75]. The presence of this peak further supports the idea that a successful surface functionalization process was performed.

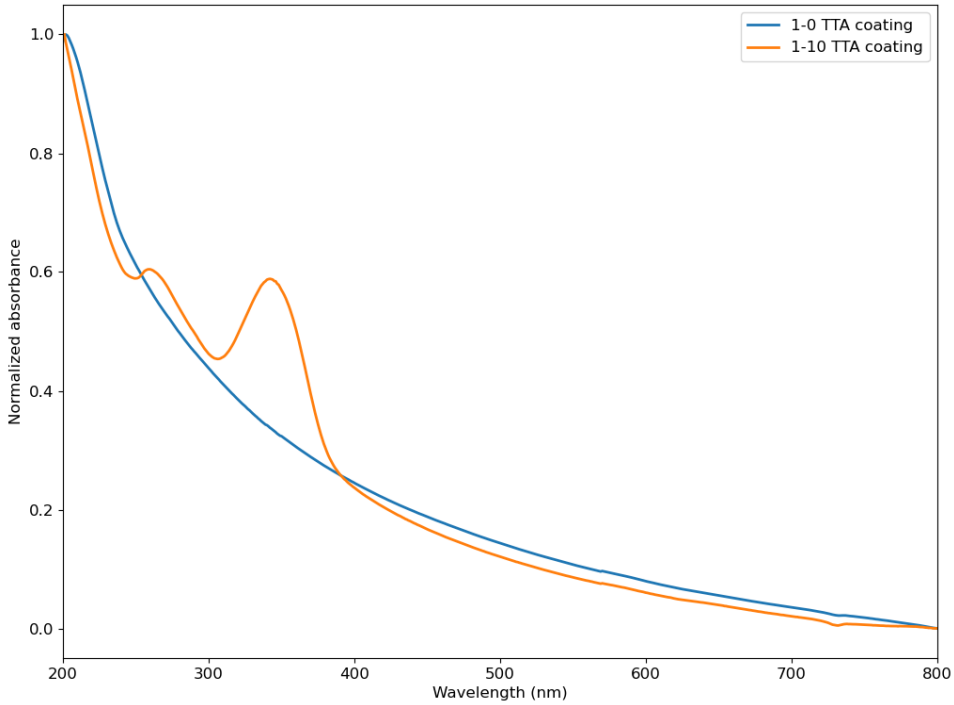

Figure 44. Absorption spectrum of uncoated Eu:CaF_2 nanoparticles (blue) compared to TTA coated Eu:CaF_2 nanoparticles (orange). The spectra were normalized to be within 0 and 1.

3.2.4 Luminescent Quantum Yield Studies

The emission spectrum of the TTA-coated nanoparticles was collected using indirect excitation at 341 nm (Figure 45). The TTA-coated nanoparticles show a sharp emission band at 613 nm which is consistent with the $^5D_0 \rightarrow {}^7F_2$ electronic transition of Eu^{3+} ions confirming the Eu-centered luminescence. Other emissions bands with relatively low intensities can be seen at 535, 580, 593 and 652 nm which correspond to the $^5D_1 \rightarrow {}^7F_0$, $^5D_0 \rightarrow {}^7F_0$, $^5D_0 \rightarrow {}^7F_1$, and $^5D_0 \rightarrow {}^7F_3$ electronic transitions, respectively. The luminescent quantum yield was calculated using Equation 2 for as-synthesized and coated nanoparticles and is reported in Table 32, more details on absorption and emission of each nanoparticle coating can be found in Table A2. Two nanoparticle sizes (470 nm and 150-170 nm) were studied to determine the effects of size on luminescent quantum yield. Uncoated nanoparticles (150-170 nm) present a higher luminescent quantum yield than those observed for the uncoated nanoparticles with a particle size of 470 nm, 2.3 ± 0.2% and 1.6 ± 0.1% respectively.

For 470 nm coated nanoparticles, the 1-10 (nanoparticles-to-TTA) mass ratio have the highest luminescent quantum yield (11.8 ± 0.2%), which corresponds to over a 7-fold increment over the uncoated nanoparticles (1.6 ± 0.1%). For nanoparticles with particle size of 470 nm, coating ratios lower than 1-10 (nanoparticles-to-TTA) present diminished luminescent quantum yields due to uncomplexed Eu^{3+} ions which decrease the maximum total emission. The low luminescent quantum yields could also be attributed to low Förster resonance energy transfer (FRET) [76] efficiency. FRET states that energy transfer can happen between separate electronic systems through a nonradiative transfer of electronic excitation energy. The rate constant of this energy transfer mechanism is inversely proportional to the sixth power of the distance between the two systems. For this reason, the longer distances between Eu^{3+} ions and the TTA sensitizers that arise from the absorption of small quantities of TTA cause low luminescent quantum yield. Coating ratios higher than 1-10 (nanoparticle-to-TTA) also present diminished luminescent quantum yields and this could be related to Ca-TTA complexes forming on the surface or due to the presence of a second coating sphere. In both cases the absorbance of the nanoparticles would increase but the emission would not, therefore decreasing the luminescent quantum yield. For 150-170 nm nanoparticles, the highest luminescent quantum yield was calculated to be 23.7 ± 0.2% for 1-50 (nanoparticle-to-TTA) ratio, which is over a 10-fold increase compared to the value (2.3 ± 0.2%) observed for the uncoated nanoparticles. The 1-50 (nanoparticle-to-TTA) coating ratio also presents a higher luminescent quantum yield than the value for $Eu(TTA)_3(H_2O)_2$ (23%), which was used as reference for the luminescent quantum yield calculations. The difference in optimal TTA coating ratios, and luminescent quantum yields between the two particle sizes can be attributed to the increase in Eu ions on the surface of the nanoparticles. The smaller nanoparticles have higher surface area and therefore they have a higher chance for Eu ions to be on the surface. The higher amount of Eu ions on the surface necessitates more TTA to saturate the Eu binding sites.

Eu^{3+}-based nanoparticles can also be directly excited through the $f \rightarrow f$ electronic transitions. However, direct excitation requires high power light sources due to the Laporte forbidden nature of the $f \rightarrow f$ electronic transitions. On the other hand, ligand-based indirect excitation provides the opportunity

to use a low power and low-cost excitation sources (Figure 46). This would make their use in potential clinical applications more likely and more cost/time effective. The possible applications could include biomedical assay platforms with high signal-to-noise ratio and rapid detection. This method could also be further developed for biological imaging protocols.

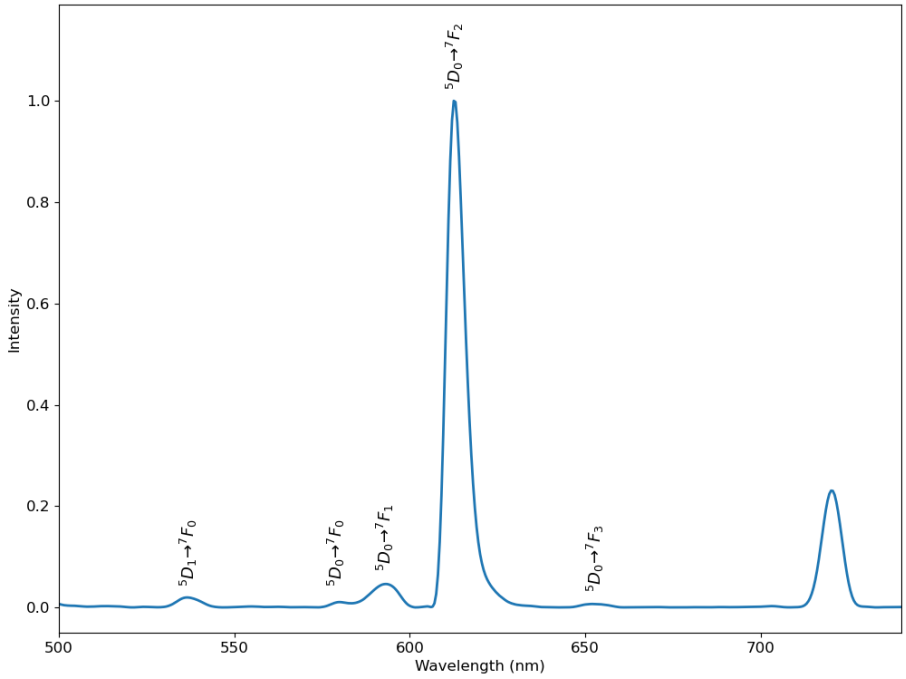

Figure 45. Emission spectrum of 10% Eu:CaF_2 nanoparticles coated with TTA (1-10 nanoparticle-to-TTA mass ratio). The characteristic emissions peak of Eu^{3+} ion can be seen at 613 nm corresponding to the $^5D_0 \rightarrow {}^7F_2$ transition. Other characteristic emissions bands of Eu^{3+} ions with relatively lower intensities can be seen at 535, 580, 593 and 652 nm which correspond to the $^5D_1 \rightarrow {}^7F_0$, $^5D_0 \rightarrow {}^7F_0$, $^5D_0 \rightarrow {}^7F_1$, and $^5D_0 \rightarrow {}^7F_3$ electronic transitions, respectively. The spectrum was normalized to be within 0 and 1.

Table 32. Calculated luminescent quantum yield values for uncoated and coated nanoparticles at different sizes.

Coating Ratio	NP size = 470 nm		NP size = 150-170 nm	
	Avg QY (%)	ST Dev (%)	Avg QY (%)	ST Dev (%)
1-1	4.2	0.5	3.0	0.1
1-5	9.2	0.2	3.2	0.1
1-10	11.8	0.2	4.91	0.08
1-25	5.85	0.04	18.0	0.2
1-50	9.1	0.3	23.7	0.2
1-75	3.3	0.2	17.1	0.3
1-100	6.0	0.2	11.7	0.2

Figure 46. TTA-coated Eu:CaF_2 nanoparticles under a low power and low-cost benchtop UV lamp (365nm). The nanoparticles show a bright red emission.

3.2.5 Epifluorescent Microscopy and Imaging

Preliminary studies to improve water dispersibility of the nanoparticles were conducted on 470 nm nanoparticles coated with TTA and ethylene glycol, tetraethylene glycol or PEG8000. The uncoated and coated nanoparticles were subjected to DLS size measurement to determine if nanoparticles aggregated in water. Uncoated nanoparticles showed an average size of 472 nm while the nanoparticles coated in ethylene glycol and tetraethylene glycol had an average value of around 4000 nm suggesting that they are aggregating in solution. Nanoparticles coated with PEG8000 had an average size of about 700 nm

suggesting very low aggregation. For this reason, PEG8000 was chosen to coat nanoparticles for imaging studies. The presence of PEG8000 on the surface of the nanoparticles was confirmed with FT-IR (Figure 47). The absorption bands at 2928 cm^{-1} and 2873 cm^{-1} in the coated nanoparticle spectrum corresponds to the antisymmetric and symmetric of CH_2[77] which appear at 2898 cm^{-1} and 2858 cm^{-1} in the spectrum of the free PEG8000. The absorption band at 1513 cm^{-1} in the coated nanoparticles spectrum correspond to the scissoring mode of CH_2[77] which appears at 1473 cm^{-1} in the reference PEG spectrum. Finally, the band at 933 cm^{-1} in the coated nanoparticle spectrum matches the band at 947 cm^{-1} which corresponds to the mixing of the CO and CC stretching modes[77]. The band at 792 cm^{-1} corresponding to the out-of-plane bending mode of CH_α coupled with the out-of-plane ring deformation of the thiophene group suggests TTA is still present on the surface of the nanoparticles.

Epifluorescent microscopy (Figure 48) showed that the TTA/PEG8000-coated nanoparticles are visible under 365 nm and could be used for biomedical imaging. In Figure 48, it is believed that the smaller and stronger signals could be individual nanoparticles or small agglomeration of nanoparticles, while the amorphous weak signals are currently unidentified.

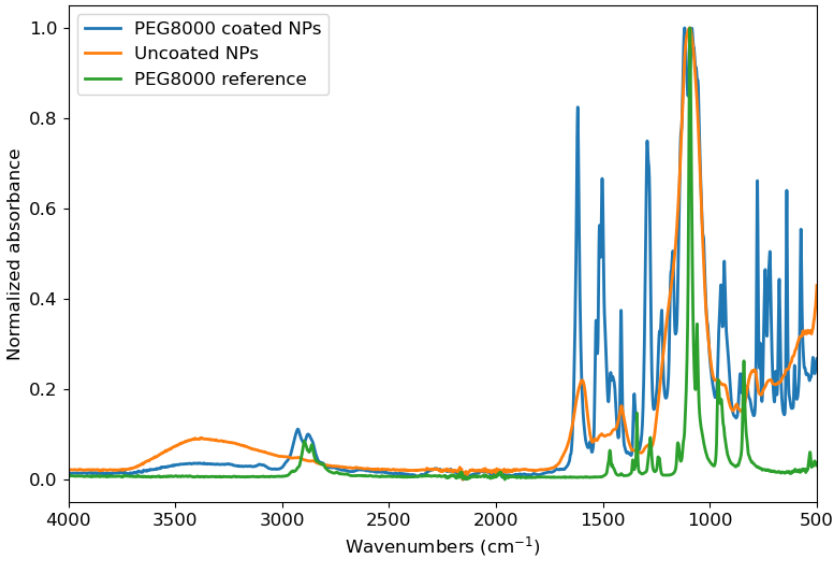

Figure 47. FTIR spectra of TTA-PEG8000-coated nanoparticles, uncoated nanoparticles and free PEG8000.

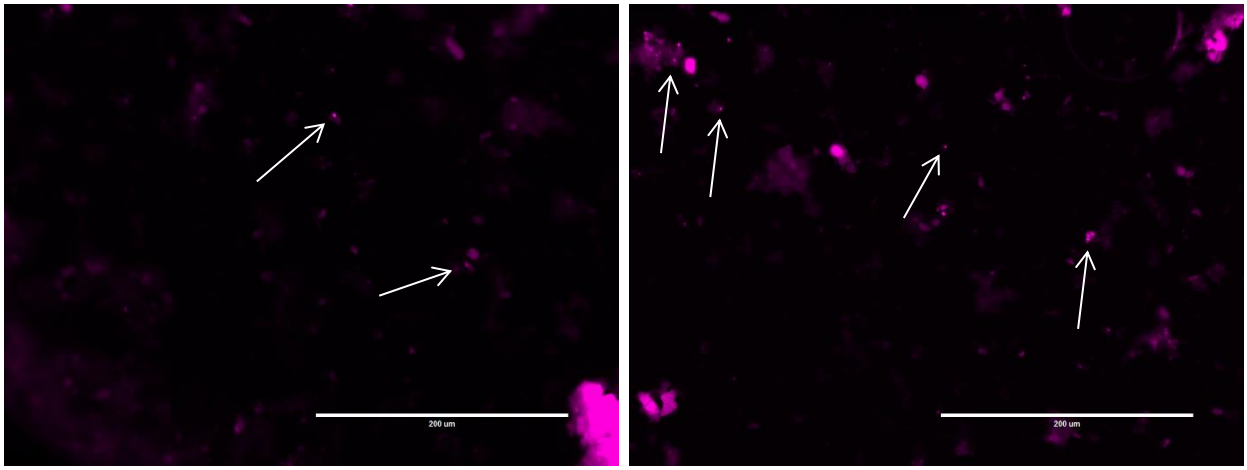

Figure 48. Epifluorescent images of TTA/PEG8000-coated nanoparticles. The dots highlighted with arrows are thought to be nanoparticles or cluster of nanoparticles, while the amorphous material with less signal is currently unidentified. Scale bar is 200 μm. Image courtesy of Dr. Youker.

CHAPTER FOUR: CONCLUSION AND FUTURE DIRECTIONS

4.1 Conclusions

In conclusion, computational studies revealed that both the 6-31G(d) and 6-311+G(d,p) basis sets can be used to accurately model these complexes. On average, monohydrate complexes present shorter ligand-metal bonds then dihydrate complex and could have higher quantum yield than the dihydrate complexes due to more efficient Dexter energy transfer and less non-radiative decay pathways. Trends between position of fluorine substituents and energies of the HOMO and LUMO levels as well as the S_1 and T_1 excited electronic states were identified. It was also observed that conjugation or lack thereof across the benzene and carboxylate group does not affect the above-mentioned energies. The optimal energies for the ISC and ET gaps were identified to be 1.1548 eV and 1.3746 eV, respectively. It was observed that luminescent quantum yield in Eu^{3+} complexes is extremely sensitive to changes in energy of the ET gap. Even so, other variables such as the ISC gap and the conjugation across the benzene and carboxylate bond cannot be ignored when describing the luminescent efficiency of fluorobenzoate Eu^{3+} complexes. In fact, it was found that while the degree of conjugation of the ligand did not play a significant role in the energies of the frontier orbitals or the energies of the excited S_1 and T_1 levels, it could play a role in aiding efficient energy transfer between the ligand and the Eu^{3+} metal center. Comparing the ideal ISC and ET gaps found in these studies to the ones of the EuTTA complex, it was hypothesized that the higher quantum yield of the EuTTA complex is caused by difference in ideal gaps energies for the different ligand classes.

Both synthesis scales were successful in synthesizing Eu:CaF_2. The small-scale reaction produced 58.74 ± 0.01 mg of nanoparticles with an average size of 40 nm (measured through SEM), while the large-scale reaction produced 399.17 ± 0.01 mg of nanoparticles with an average size of 472 ± 8 nm (measured through DLS). Powder XRD reveals that crystal structure of the nanoparticles corresponds to the cubic face-centered structure of pure CaF_2 suggesting that europium doping does not significantly alter the crystal structure of the nanoparticles. The crystalline size was 6.95 nm and 10.8 nm for the small-

and large-scale synthesis respectively, suggesting that the nanoparticles are an aggregation of crystalline spheres. This is further supported by the oriented dark-field TEM image. FT-IR spectroscopy showed that the coating exchange reaction was successful for both TTA and PEG8000. The UV-Vis spectrum of Eu:CaF_2 revealed an absorption band at 341 nm. The emission spectrum of the nanoparticles shows the characteristic emission of Eu^{3+} ions with a bright orange luminescence at 613 nm. The optimal coating ratio and highest luminescent quantum yield were dependent on the size of the nanoparticles. Large nanoparticles with diameter of 470 nm, showed a maximum luminescent quantum yield of 11.8% at a coating ration of 1-10 (nanoparticle-to-TTA), while the smaller nanoparticles showed a maximum luminescent quantum yield of 23.7% at a coating ratio of 1-50 (nanoparticles-to-TTA). Preliminary epifluorescent imaging of the nanoparticles shows great promise for the use of these nanoparticles in future biomedical imaging.

4.2 Future work

Future work might include:

- Expanding the theoretical calculations to more benzoate ligand with different electron withdrawing and electron donating groups to develop methods to predict changes in frontier orbitals energies and S_1 and T_1 levels as well as luminescent quantum yields;
- Conducting more rigorous studies of the effects of dihedral angles (and therefore conjugation) in benzoate system on luminescent quantum yield and energy transfer efficiency;
- Further decreasing the size of the TTA-coated nanoparticles to increase luminescent quantum yield and cellular uptake;
- Optimizing PEG8000 coating ratios to improve water dispersibility without significantly reducing the luminescent quantum yield of the nanoparticles;
- Studying cellular uptake efficiency in human live cells (HEK293 and HUVEC cells) to develop cellular imaging protocols;
- Increasing specificity of the nanoparticles for certain cells for selective cancer imaging.

REFERENCES

(1) Lewars, E. G. *Computational Chemistry*; Springer Netherlands: Dordrecht, 2011. https://doi.org/10.1007/978-90-481-3862-3.

(2) Foresman, J. B.; Frisch, A. *Exploring Chemistry with Electronic Structure Methods*, Second.; Gaussian, Inc: Wallingford, 1996.

(3) Becke, A. D. Density Functional Thermochemistry. III. The Role of Exact Exchange. *J. Chem. Phys* **1993**, *98* (7), 5648–5652. https://doi.org/10.1063/1.464913.

(4) Stephens, P. J.; Devlin, F. J.; Chabalowski, C. F.; Frisch, M. J. Ab Initio Calculation of Vibrational Absorption and Circular Dichroism Spectra Using Density Functional Force Fields. *J, Phys. Chem.* **1994**, *98* (45), 11623–11627.

(5) Wilk A N, L.; Nusair, D. M. Accurate Spin-Dependent Electron Liquid Correlation Energies for Local Spin Density Calculations: A Critical Analysis1. *Can. J. Phys.* **1980**, *58*, 1200–1211.

(6) Lee, C.; Yang, eitao; Parr, R. G. Development of the Colic-Salvetti Correlation-Energy Formula into a Functional of the Electron Density. *Phys. Rev.* **1988**, *37* (2), 785–789.

(7) Jain, P. K.; ElSayed, I. H.; El-Sayed, M. A. Au Nanoparticles Target Cancer. *Nano Today* **2007**, *2* (1), 18–29. https://doi.org/10.1016/S1748-0132(07)70016-6.

(8) Gao, C.; Lyu, F.; Yin, Y. Encapsulated Metal Nanoparticles for Catalysis. *Chem. Rev.* **2021**, *121*, 834–881. https://doi.org/10.1021/acs.chemrev.0c00237.

(9) Mukherjee, A.; Majumdar, S.; Servin, A. D.; Pagano, L.; Dhankher, O. P.; White, J. C. Carbon Nanomaterials in Agriculture: A Critical Review. *Front. Plant Sci.* **2016**, *7* (172). https://doi.org/10.3389/fpls.2016.00172.

(10) Nazari, A.; Riahi, S. Improvement Compressive Strength of Concrete in Different Curing Media by Al2O3 Nanoparticles. *Mater. Sci. Eng. A* **2011**, *528* (3), 1183–1191. https://doi.org/10.1016/J.MSEA.2010.09.098.

(11) Mansoori, G. A. *Principles of Nanotechnology: Molecular-Based Study of Condensed Matter in Small Systems*; World Scientific, 2005.

(12) Poothanari, M. A.; Pottathara, Y. B.; Thomas, S. Chapter 8 - Carbon Nanostructures for Electromagnetic Shielding Applications. In *Industrial Applications of Nanomaterials: Micro and Nano Technologies*; Elsevier, 2019; pp 205–223. https://doi.org/10.1016/B978-0-12-815749-7.00008-6.

(13) Zhang, Q.; O'Brien, S.; Grimm, J. Biomedical Applications of Lanthanide Nanomaterials, for Imaging, Sensing and Therapy. *Nanotheranostics* **2022**, *6* (2), 184–194. https://doi.org/10.7150/ntno.65530.

(14) Zhou, J.; Leaño, J. L.; Liu, Z.; Jin, D.; Wong, K.; Liu, R.; Bünzli, J. G. Impact of Lanthanide Nanomaterials on Photonic Devices and Smart Applications. *Small* **2018**, *14*, 1801882. https://doi.org/10.1002/smll.201801882.

(15) Dong, H.; Du, S.-R.; Zheng, X.-Y.; Lyu, G.-M.; Sun, L.-D.; Li, L.-D.; Zhang, P.-Z.; Zhang, C.; Yan, C.-H. Lanthanide Nanoparticles: From Design toward Bioimaging and Therapy. *Chem. Rev.* **2015**, *115* (19), 10725–10815. https://doi.org/10.1021/acs.chemrev.5b00091.

(16) Starck, M.; Pal, R.; Parker, D. Structural Control of Cell Permeability with Highly Emissive Europium(III) Complexes Permits Different Microscopy Applications. *Chem. Eur. J.* **2016**, *22* (2), 570–580. https://doi.org/10.1002/chem.201504103.

(17) Bui, A. T.; Grichine, A.; Duperray, A.; Lidon, P.; Riobé, F.; Andraud, C.; Maury, O. Terbium(III) Luminescent Complexes as Millisecond-Scale Viscosity Probes for Lifetime Imaging. *J. Am.*

Chem. Soc. **2017**, *139* (23), 7693–7696. https://doi.org/10.1021/JACS.7B02951/ASSET/IMAGES/LARGE/JA-2017-02951E_0005.JPEG.

(18) Leif, R. C.; Vallarino, L. M.; Becker, M. C.; Yang, S. Increasing the Luminescence of Lanthanide Complexes. *Cytom. Part A* **2006**, *8*, 767–778. https://doi.org/10.1002/cyto.a.20321.

(19) Lima, P. P.; Nolasco, M. M.; Paz, F. A. A.; Ferreira, R. A. S.; Longo, R. L.; Malta, O. L.; Carlos, L. D. Photo−Click Chemistry to Design Highly Efficient Lanthanide β-Diketonate Complexes Stable under UV Irradiation. *Chem. Mater* **2013**, *25*, 586–598. https://doi.org/10.1021/cm303776x.

(20) Wang, X.; Chang, H.; Xie, J.; Zhao, B.; Liu, B.; Xu, S.; Pei, W.; Ren, N.; Huang, L.; Huang, W. Recent Developments in Lanthanide-Based Luminescent Probes. *Coord. Chem. Rev.* **2014**, *273–274*, 201–212. https://doi.org/10.1016/J.CCR.2014.02.001.

(21) Kuroda, Y.; Sugou, K.; Sasaki, K. Nonameric Porphyrin Assembly: Antenna Effect on Energy Transfer. *J. Am. Chem. Soc.* **2000**, *122* (32), 7833–7834. https://doi.org/10.1021/JA001506K/SUPPL_FILE/JA001506K_S.PDF.

(22) Su, Y.; Zhang, D.; Jia, P.; Gao, W.; Li, Y.; He, J.; Wang, C.; Zheng, X.; Yang, Q.; Yang, C. Bonded-Luminescent Foam Based on Europium Complexes as a Reversible Copper (II) Ions Sensor in Pure Water. *Eur. Polym. J.* **2019**, *112*, 461–465. https://doi.org/10.1016/J.EURPOLYMJ.2019.01.034.

(23) Yang, C.; Liu, S.; Xu, J.; Li, Y.; Shang, M.; Lei, L.; Wang, G.; He, J.; Wang, X.; Lu, M. Efficient Red Emission from Poly(Vinyl Butyral) Films Doped with a Novel Europium Complex Based Terpyridyl as Ancillary Ligand: Synthesis, Structural Elucidation by Sparkle/RM1 Calculation, and Photophysical Properties. *Poly. Chem.* **2015**, *00*, 1–11. https://doi.org/10.1039/x0xx00000x.

(24) Binnemans, K. Lanthanide-Based Luminescent Hybrid Materials. *Chem. Rev.* **2009**, *109*, 4283–4374. https://doi.org/10.1021/cr8003983.

(25) Kalyakina, A. S.; Utochnikova, V. V.; Bushmarinov, I. S.; Le-Deygen, I. M.; Volz, D.; Weis, P.; Schepers, U.; Kuzmina, N. P.; Bräse, S. Lanthanide Fluorobenzoates as Bio-Probes: A Quest for the Optimal Ligand Fluorination Degree. *Chem. Eur. J.* **2017**, *23* (59), 14944–14953. https://doi.org/10.1002/chem.201703543.

(26) Da Costa, O. M. M. M.; De Azevedo, W. M. Highly Luminescent Metal Organic Framework Eu(TMA)(H2O)4 Materials Prepared by Laser Ablation Technique in Liquid. *J. Lumin.* **2016**, *170*, 648–653. https://doi.org/10.1016/j.jlumin.2015.09.004.

(27) Hasegawa, M.; Iwasawa, D.; Kawaguchi, T.; Koike, H.; Saso, A.; Ogata, S.; Ishii, A.; Ohmagari, H.; Iwamura, M.; Nozaki, K. Chiroptical Spectroscopic Studies on Lanthanide Complexes with Valinamide Derivatives in Solution. *Chempluschem* **2020**, *85* (2), 294–300. https://doi.org/10.1002/cplu.201900692.

(28) Ogata, S.; Komiya, H.; Goto, N.; Tanabe, R.; Sugimoto, K.; Kawaguchi, S.; Goto, K.; Hatanaka, M.; Ishii, A.; Hasegawa, M. Strong Luminescent Europium Complexes Induced by the Unprecedented Anti-Chelate Effect of Acyl Groups on a N6-Hexadentate Ligand. *Chem. Lett.* **2019**, *48* (6), 593–596. https://doi.org/10.1246/cl.190140.

(29) Lima, N. B. D.; Gonçalves, S. M. C.; Júnior, S. A.; Simas, A. M. A Comprehensive Strategy to Boost the Quantum Yield of Luminescence of Europium Complexes. *Sci. Rep.* **2013**, *3* (2395). https://doi.org/10.1038/srep02395.

(30) Li, L.-L.; Zhang, R.; Yin, L.; Zheng, K.; Qin, W.; Selvin, P. R.; Lu, Y. Biomimetic Surface Engineering of Lanthanide-Doped Upconversion Nanoparticles as Versatile Bioprobes. *Angew. Chem.* **2012**, *124* (25), 6225–6229. https://doi.org/10.1002/ANGE.201109156.

(31) Liu, J.; Artizzu, F.; Zeng, M.; Pilia, L.; Geiregat, P.; Van Deun, R. Dye-Sensitized Er 3+-Doped CaF 2 Nanoparticles for Enhanced near-Infrared Emission at 1.5 Mm. *Photonics Res.* **2021**, *9* (10), 2037–2045. https://doi.org/10.1364/PRJ.433192.

(32) Davis, A. D. Microwave-Assisted Synthesis of Europium-Doped Calcium Fluoride Nanoparticles for Potential Biomedical Applications, Western Carolina University, Cullowhee, 2019.

(33) Mizumoto, Y.; Aoyama, T.; Kakinuma, Y. Basic Study on Ultraprecision Machining of Single-Crystal Calcium Fluoride. *Procedia Eng.* **2011**, *19*, 264–269. https://doi.org/10.1016/J.PROENG.2011.11.110.

(34) Liu, G.; Sun, Z.; Fu, Z.; Ma, L.; Wang, X. Temperature Sensing and Bio-Imaging Applications Based on Polyethylenimine/CaF 2 Nanoparticles with Upconversion Fluorescence. *Talanta* **2017**, *169*, 181–188. https://doi.org/10.1016/j.talanta.2017.03.054.

(35) Pandurangappa, C.; Lakshminarasappa, B. N.; Nagabhushana, B. M. Synthesis and Characterization of CaF2 Nanocrystals. *J. Alloys Compd.* **2010**, *489* (2), 592–595. https://doi.org/10.1016/J.JALLCOM.2009.09.118.

(36) Labéguerie, J.; Gredin, P.; Mortier, M.; Patriarche, G.; De Kozak, A. Synthesis of Fluoride Nanoparticles in Non-Aqueous Nanoreactors. Luminescence Study of Eu3+:CaF2. *Z. Anorg. Allg. Chem.* **2006**, *632* (8–9), 1538–1543. https://doi.org/10.1002/zaac.200600074.

(37) Kuzmanoski, A.; Pankratov, V.; Feldmann, C. Energy Transfer of the Quantum-Cutter Couple Pr3+–Mn2+ in CaF2:Pr3+, Mn2+ Nanoparticles. *J. Lumin.* **2016**, *179*, 555–561. https://doi.org/10.1016/j.jlumin.2016.07.040.

(38) Vallet, V.; Fischer, A.; Szabó, Z.; Grenthe, I. The Structure and Bonding of Y, Eu, U, Am and Cm Complexes as Studied by Quantum Chemical Methods and X-Ray Crystallography. *Dalton Trans.* **2010**, *39* (33), 7666. https://doi.org/10.1039/b926508b.

(39) Malta, O. L.; Brito, H. F.; Menezes, J. F. S.; Gonçalves e Silva, F. R.; De Mello Donegá, C.; Alves, S. Experimental and Theoretical Emission Quantum Yield in the Compound

Eu(Thenoyltrifluoroacetonate)3.2(Dibenzyl Sulfoxide). *Chem. Phys. Lett.* **1998**, *282*, 233–238. https://doi.org/10.1016/S0009-2614(97)01283-9.

(40) Molina, C.; Dahmouche, K.; Messaddeq, Y.; Ribeiro, S. J. L.; Silva, M. A. P.; De Zea Bermudez, V.; Carlos, L. D. Enhanced Emission from Eu(III) β-Diketone Complex Combined with Ether-Type Oxygen Atoms of Di-Ureasil Organic-Inorganic Hybrids. *J. Lumin.* **2003**, *104*, 93–101. https://doi.org/10.1016/S0022-2313(02)00684-1.

(41) Frisch, M. J.; Trucks, G. W.; Schlegel, H. B.; Scuseria, G. E.; Robb, M. A.; Cheeseman, J. R.; Scalmani, G.; Barone, V.; Petersson, G. A.; Nakatsuji, H.; Li, X.; Caricato, M.; Marenich, A.; Bloino, J.; Janesko, B. G.; Gomperts, R.; Mennucci, B.; Hratchian, H. P.; Ortiz, J. V.; Izmaylov, A. F.; Sonnenberg, J. L.; Williams-Young, D.; Ding, F.; Lipparini, F.; Egidi, F.; Goings, J.; Peng, B.; Petrone, A.; Henderson, T.; Ranasinghe, D.; Zakrzewski, V. G.; Gao, J.; Rega, N.; Zheng, G.; Liang; Hada, M.; Ehara, M.; Toyota, K.; Fukuda, R.; Hasegawa, J.; Ishida, M.; Nakajima, T.; Honda, Y.; Kitao, O.; Nakai, H.; Vreven, T.; Throssell, K.; Montgomery, J. A. J.; Peralta, J. E.; Ogliaro, F.; Bearpark, M.; Heyd, J. J.; Brothers, E.; Kudin, K. N.; Staroverov, V. N.; Keith, T.; Kobayashi, R.; Normand, J.; Raghavachari, K.; Rendell, A.; Burant, J. C.; Iyengar, S. S.; Tomasi, J.; Cossi, M.; Millam, J. M.; Klene, M.; Adamo, C.; Cammi, R.; Ochterski, J. W.; Martin, R. L.; Morokuma, K.; Farkas, O.; Foresman, J. B.; Fox, D. J. Gaussian 09. Gaussian, Inc.: Wallingford CT 2016.

(42) Perrin, L.; Maron, L.; Eisenstein, O. A DFT Study of SiH 4 Activation by Cp 2 LnH. *Inorg. Chem.* **2002**, *41*, 4355–4362. https://doi.org/10.1021/ic011275y.

(43) Maron, L.; Eisenstein, O.; Alary, F.; Poteau, R. Modeling C5H5 with Atoms or Effective Group Potential in Lanthanide Complexes: Isolobality Not the Determining Factor. *J. Phys. Chem. A* **2002**, *106*, 1797–1801. https://doi.org/10.1021/jp013693u.

(44) Maron, L.; Eisenstein, O. DFT Study of H-H Activation by Cp 2 LnH D0 Complexes. *J. Am. Chem. Soc.* **2001**, *123*, 10361039. https://doi.org/10.1021/ja0033483.

(45) Maron, L.; Perrin, L.; Eisenstein, O. CF4 Defluorination by Cp2 Ln–H: A DFT Study. *Dalton Trans.* **2003**, No. 22, 4313–4318. https://doi.org/10.1039/B308433G.

(46) Ma, L.; Yang, L.-L.; Wang, Y.-G.; Zhou, X.-P.; Xu, X.-Y. Microwave-Assisted Preparation of Nearly Monodisperse Flower-like CaF2 Microspheres. *Ceram. Int.* **2013**, *5*, 5973–5977.

(47) Maron, L.; Eisenstein, O. Do f Electrons Play a Role in the Lanthanide-Ligand Bonds? A DFT Study of Ln(NR 2) 3 ; R) H, SiH 3. *J. Phys. Chem.* **2000**, *104*, 7140–7143. https://doi.org/10.1021/jp0010278.

(48) Ruščić, B.; Goodman, G. L.; Berkowitz, J. Photoelectron Spectra of the Lanthanide Trihalides and Their Interpretation. *J. Chem. Phys* **1983**, *78*, 5443. https://doi.org/10.1063/1.445473.

(49) Dolg, M.; Stoll, H.; Savin, A.; Preuss, H. Energy-Adjusted Pseudopotentials for the Rare Earth Elements. *Theor. Chim. Acta* **1989**, *75*, 173–194.

(50) Dolg, M.; Fulde, P.; Küchle, W.; Neumann, C.-S.; Stoll, H. Ground State Calculations of Di-π-Cyclooctatetraene Cerium. *J. Chem. Phys* **1991**, *94*, 3011. https://doi.org/10.1063/1.459824.

(51) Francl, M. M.; Pietro, W. J.; Hehre, W. J.; Binkley, J. S.; Gordon, M. S.; DeFrees, D. J.; Pople, J. A. Self-Consistent Molecular Orbital Methods. XXIII. A Polarization-Type Basis Set for Second-Row Elements. *J. Chem. Phys.* **1982**, *77* (3654). https://doi.org/10.1063/1.444267.

(52) McLean, A. D.; Chandler, G. S. Contracted Gaussian Basis Sets for Molecular Calculations. I. Second Row Atoms, Z=11–18. *J. Chem. Phys.* **1980**, *72* (10), 5639–5648. https://doi.org/10.1063/1.438980.

(53) Scherrer, P. Bestimmung Der Größe Und Der Inneren Struktur von Kolloidteilchen Mittels Röntgenstrahlen. *Gött. Nachr. Math. Phys.* **1918**, *2*, 98–100.

(54) Press, W. H.; Teukolsky, S. A.; Vetterling, W. T.; Flannery, B. P. Chapter 4: Integration of Functions. In *Numerical Recipes in FORTRAN : The Art of Scientific Computing*; Cambridge University Press, 1992; Vol. 1, pp 123–158.

(55) Shi, M.; Li, F.; Yi, T.; Zhang, D.; Hu, H.; Huang, C. Tuning the Triplet Energy Levels of Pyrazolone Ligands to Match the 5D0 Level of Europium(III). *Inorg. Chem.* **2005**, *44* (24), 8929–8936. https://doi.org/10.1021/IC050844P/SUPPL_FILE/IC050844PSI20050621_031036.PDF.

(56) Zurita, J. L.; De Soria, M. L. G.; Postigo, M. A.; Katz, M. Vapor-Liquid Equilibrium for the n-Pentane-Dichloromethane System at 298.15 K. *J. Chem. Eng. Data* **1986**, *31*, 389–390.

(57) Iloukhani, H.; Almasi, M. Densities, Viscosities, Excess Molar Volumes, and Refractive Indices of Acetonitrile and 2-Alkanols Binary Mixtures at Different Temperatures: Experimental Results and Application of the Prigogine-Flory-Patterson Theory. *Thermochim. Acta* **2009**, *495*, 139–148. https://doi.org/10.1016/J.TCA.2009.06.015.

(58) De Silva, C. R.; Maeyer, J. R.; Wang, R.; Nichol, G. S.; Zheng, Z. Adducts of Europium β-Diketonates with Nitrogen p,P′-Disubstituted Bipyridine and Phenanthroline Ligands: Synthesis, Structural Characterization, and Luminescence Studies. *Inorg. Chim. Acta* **2007**, *360* (11), 3543–3552. https://doi.org/10.1016/J.ICA.2007.04.049.

(59) Dexter, D. L. A Theory of Sensitized Luminescence in Solids. *J. Chem. Phys.* **1953**, *21*, 836–850. https://doi.org/10.1063/1.1699044.

(60) Mara, M. W.; Tatum, D. S.; March, A. M.; Doumy, G.; Moore, E. G.; Raymond, K. N. Energy Transfer from Antenna Ligand to Europium(III) Followed Using Ultrafast Optical and X-Ray Spectroscopy. *J. Am. Chem. Soc.* **2019**, *141* (28), 11071–11081. https://doi.org/10.1021/JACS.9B02792/ASSET/IMAGES/MEDIUM/JA-2019-02792A_M004.GIF.

(61) Hasegawa, M.; Ohmagari, H.; Tanaka, H.; Machida, K. Luminescence of Lanthanide Complexes: From Fundamental to Prospective Approaches Related to Water- and Molecular-Stimuli. *J. Photochem. Photobiol. C: Photochem. Rev.* **2022**, *50*. https://doi.org/10.1016/J.JPHOTOCHEMREV.2022.100484.

(62) Brink, G. O. Absorption Spectrum of the Fourth Overtone of the OH Stretch in Gaseous Methanol. *J. Mol. Spectrosc.* **1984**, *103* (2), 295–299. https://doi.org/10.1016/0022-2852(84)90056-0.

(63) Liang, L.; Zhang, N.; Cao, R.; Wang, S.; Liu, S.; Yu, Z.; Liu, Q.; Wang, J.; Li, Z.; Jiang, T. Enhanced Red Emissions of Europium (III) Chelates in RNA–OTMA Complexes. *Coatings* **2022**, *12* (1467). https://doi.org/10.3390/coatings12101467.

(64) Dar, W. A.; Ganaie, A. B.; Iftikhar, K. Synthesis and Photoluminescence Study of Two New Complexes [Sm(Hfaa)3(Impy)2] and [Eu(Hfaa)3(Impy)2] and Their PMMA Based Hybrid Films. *J. Lumin.* **2018**, *202*, 438–449. https://doi.org/10.1016/j.jlumin.2018.05.032.

(65) Sudarlin; Abdulkadir Martoprawiro, M. Theoretical Study of the Electron-Withdrawing and Donating Groups Effects on Luminescent Properties of the Europium Complexes with Substituted 1,10 Phenanthroline. *J. Phys. Conf. Ser.* **2019**, *1277* (012025). https://doi.org/10.1088/1742-6596/1277/1/012025.

(66) Freire, R. O.; Albuquerque, R. Q.; Junior, S. A.; Rocha, G. B.; De Mesquita, M. E. On the Use of Combinatory Chemistry to the Design of New Luminescent Eu3+ Complexes. *Chem. Phys. Lett.* **2005**, *405* (1–3), 123–126. https://doi.org/10.1016/j.cplett.2005.02.022.

(67) Latva, M.; Takalob, H.; Mukkala, V. M.; Matachescu, C.; Rodríguez-Ubis, J. C.; Kankare, J. Correlation between the Lowest Triplet State Energy Level of the Ligand and Lanthanide(III) Luminescence Quantum Yield. *J. Lumin.* **1997**, *75*, 149–169. https://doi.org/10.1016/S0022-2313(97)00113-0.

(68) Steemers, F. J.; Verboom, W.; Reinhoudt, D. N.; Van Der Tol, E. B.; Verhoeven, J. W. New Sensitizer-Modified Calix[4]Arenes Enabling Near-UV Excitation of Complexed Luminescent Lanthanide Ions. *J. Am. Chem. Soc* **1995**, *117*, 9408–9414.

(69) Phillip Lacovara. Energy Transfer and Upconversion in Ytterbium:YAG and Ytterbium:Erbium:YAG - ProQuest, Boston College, 1992. https://www.proquest.com/openview/fc46f9961700d9204356006ba88da4ce/1?cbl=18750&diss=y&pq-origsite=gscholar&parentSessionId=vICUY%2Ff4u5kFytXEKX15uUBNFS4zxdHUNigIQlxDtbA%3D (accessed 2023-03-30).

(70) Pacheco, D.; Di Bartolo, B. Energy Transfer and Fluorescence Characteristics of Erbium-Doped Ytterbium Aluminum Garnet. *J Lumin* **1976**, *14* (3), 19–39. https://doi.org/10.1016/S0022-2313(76)90112-5.

(71) Wang, L.; Wang, B.; Wang, X.; Liu, W. Tribological Investigation of CaF2 Nanocrystals as Grease Additives. *Trib. Int.* **2007**, *40* (7), 1179–1185. https://doi.org/10.1016/J.TRIBOINT.2006.12.003.

(72) Mitra, S.; Werling, K.; Berquist, E. J.; Lambrecht, D. S.; Garrett-Roe, S. CH Mode Mixing Determines the Band Shape of the Carboxylate Symmetric Stretch in Apo-EDTA, Ca 2+ −EDTA, and Mg 2+ −EDTA. *J. Phys. Chem. A* **2021**, *125*, 4867–4881. https://doi.org/10.1021/acs.jpca.1c03061.

(73) Nekoei, A.-R.; Faramarz Tayyari, S.; Vakili, M.; Holakoei, S.; Hossein Hamidian, A.; Erik Sammelson, R. Conformation and Vibrational Spectra and Assignment of 2-Thenoyltrifluoroacetone. *J. Mol. Struct.* **2009**, *932*, 112–122. https://doi.org/10.1016/j.molstruc.2009.05.045.

(74) De Silva, C. R.; Maeyer, J. R.; Dawson, A.; Zheng, Z. Adducts of Lanthanide β-Diketonates with 2,4,6-Tri(2-Pyridyl)-1,3,5-Triazine: Synthesis, Structural Characterization, and Photoluminescence Studies. *Polyhedron* **2007**, *26* (6), 1229–1238. https://doi.org/10.1016/J.POLY.2006.10.049.

(75) De Silva, C. R.; Wang, R.; Zheng, Z. Highly Luminescent Eu(III) Complexes with 2,4,6-Tri(2-Pyridyl)-1,3,5-Triazine Ligand: Synthesis, Structural Characterization, and Photoluminescence Studies. *Polyhedron* **2006**, *25*, 3449–3455. https://doi.org/10.1016/j.poly.2006.06.032.

(76) Förster, T. Transfer Mechanisms of Electronic Excitation Energy. *Radiat. Res. Suppl.* **1960**, *2*, 326–339.

(77) Rubinson, K. A.; Meuse, C. W. Deep Hydration: Poly(Ethylene Glycol) Mw 2000-8000 Da Probed by Vibrational Spectrometry and Small-Angle Neutron Scattering and Assignment of ΔG° to Individual Water Layers. *Polymer (Guildf)* **2013**, *54*, 709–723. https://doi.org/10.1016/j.polymer.2012.11.016.

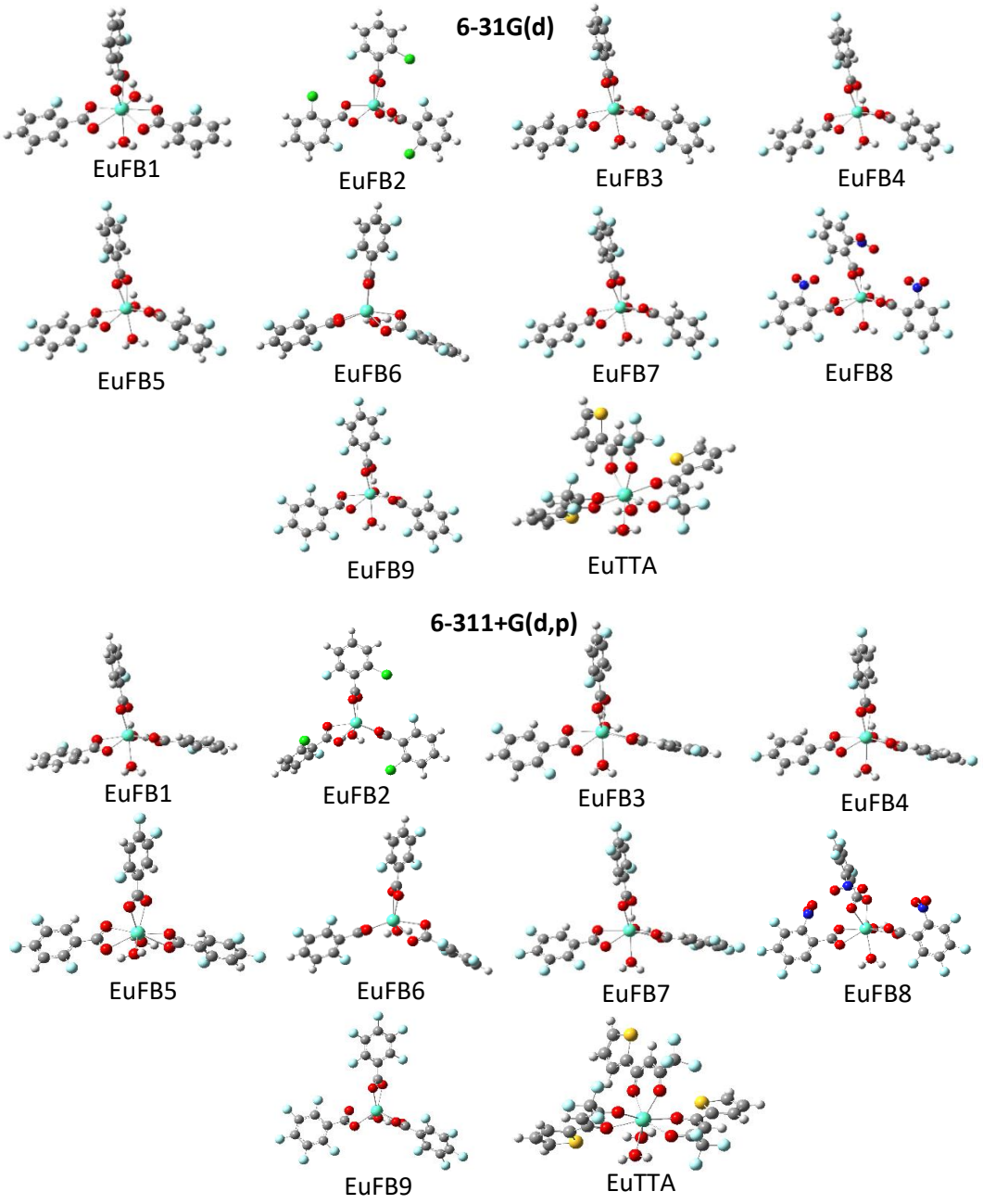

Figure A1. Optimized geometries obtained by DFT calculations using 6-31G(d) and 6-311+G(d,p) basis sets of the studied compounds with structures reported in Kalyakina et al and Vallet et al. In gray are the C atoms, in white are the H atoms, in red are the O atoms, in light blue are the F atoms, in dark blue are the N atoms, in green are the Cl atoms and in blue-green are the Eu atoms.

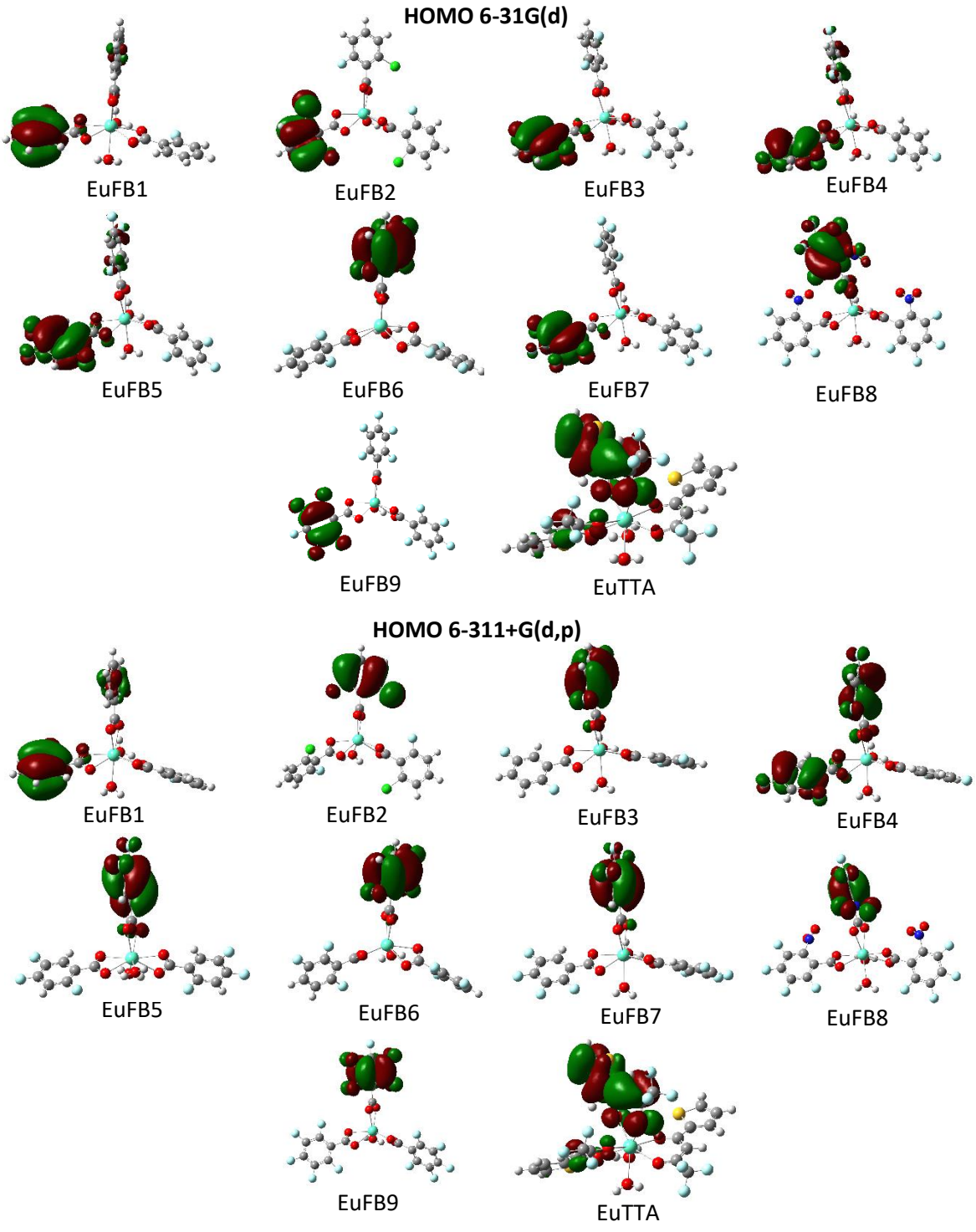

Figure A2. HOMO orbitals as calculated for the 6-31G(d) and 6-311+G(d,p) basis sets for the complexes originally treated in Kalyakina et al. and for the EuTTA complex. Green orbitals are the positive values of the wavefunction, while the red orbitals are the negative values.

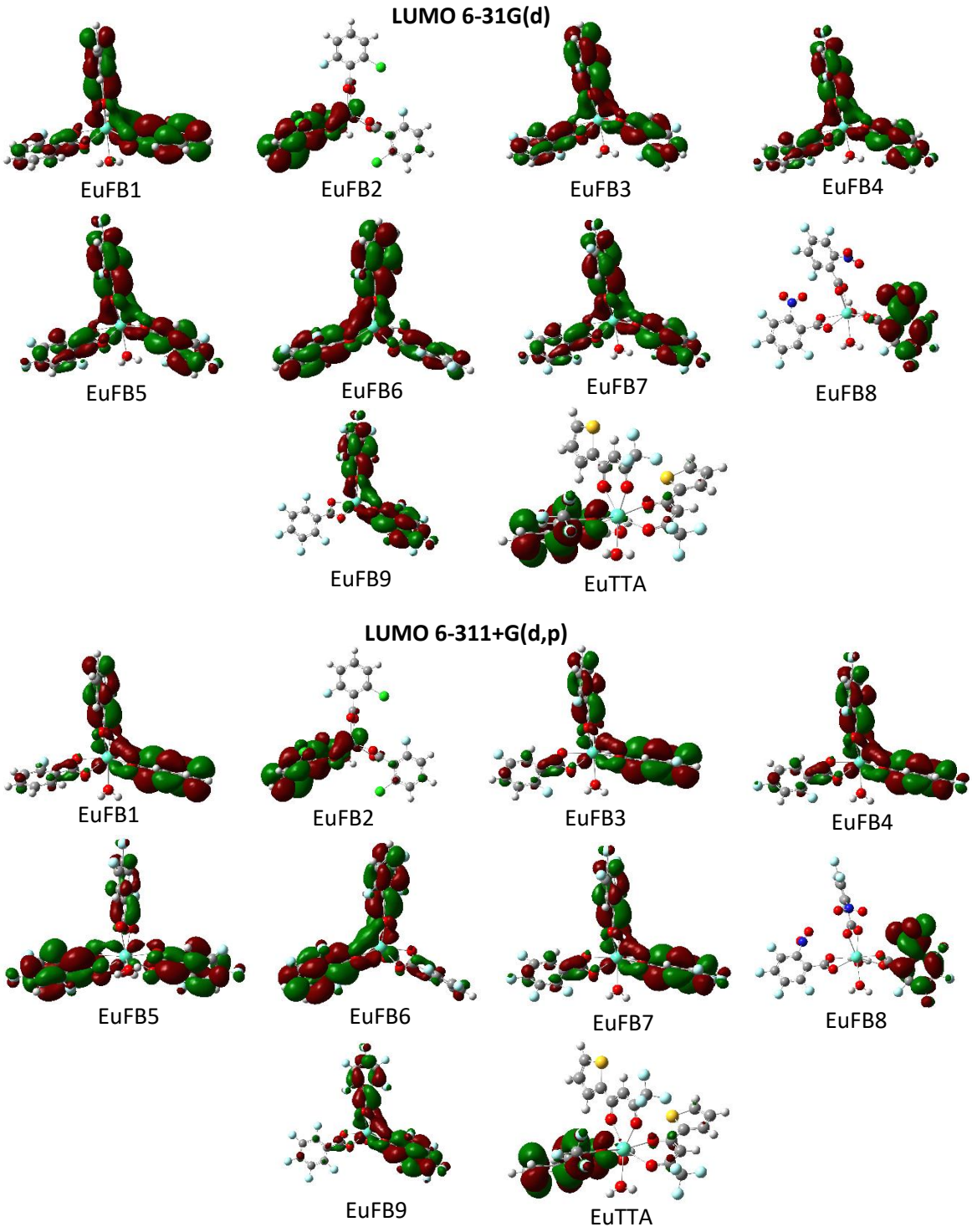

Figure A3. LUMO orbitals as calculated for the 6-31G(d) and 6-311+G(d,p) basis sets for the complexes originally treated in Kalyakina et al. and for the EuTTA complex. Green orbitals are the positive values of the wavefunction, while the red orbitals are the negative values.

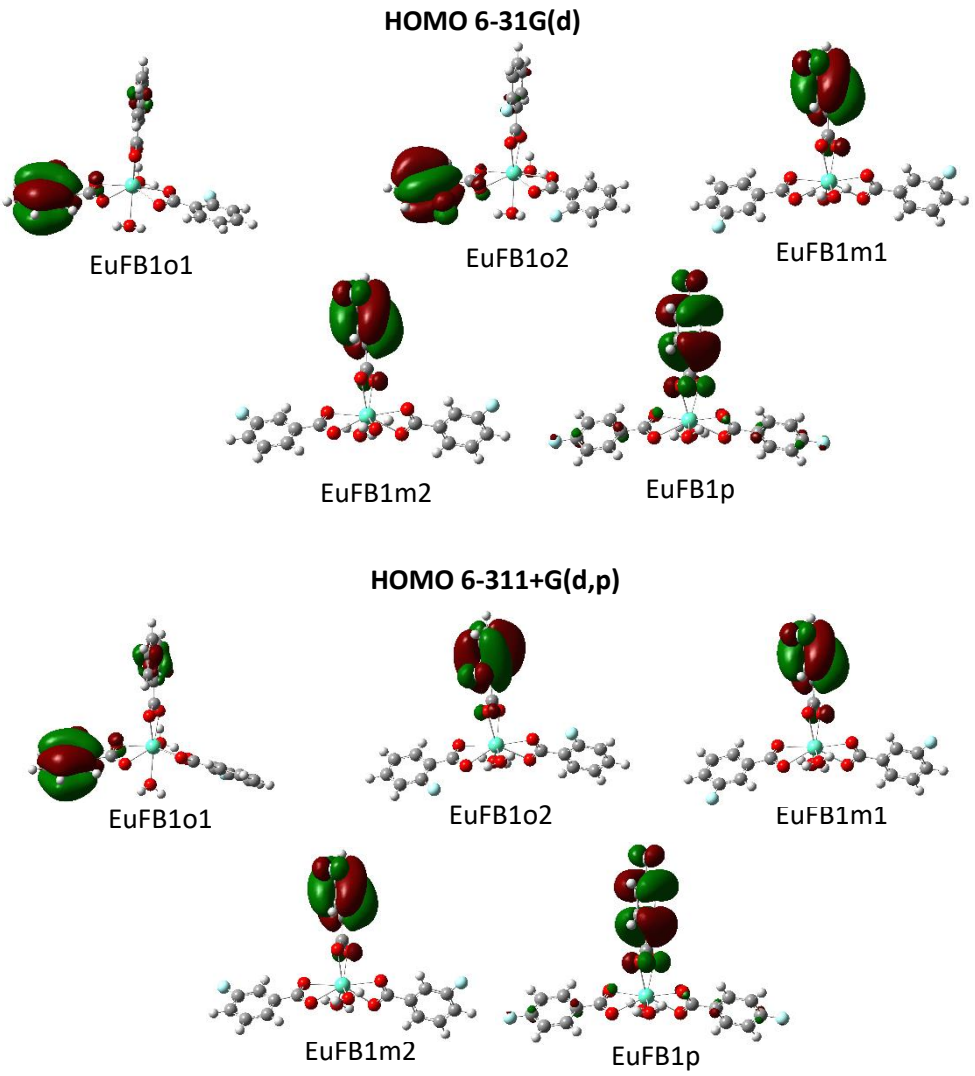

Figure A4. HOMO orbitals as calculated for the 6-31G(d) and 6-311+G(d,p) basis sets for the complexes obtained by moving a single fluorine atom around the ring of a benzoate ligand. Green orbitals are the positive values of the wavefunction, while the red orbitals are the negative values.

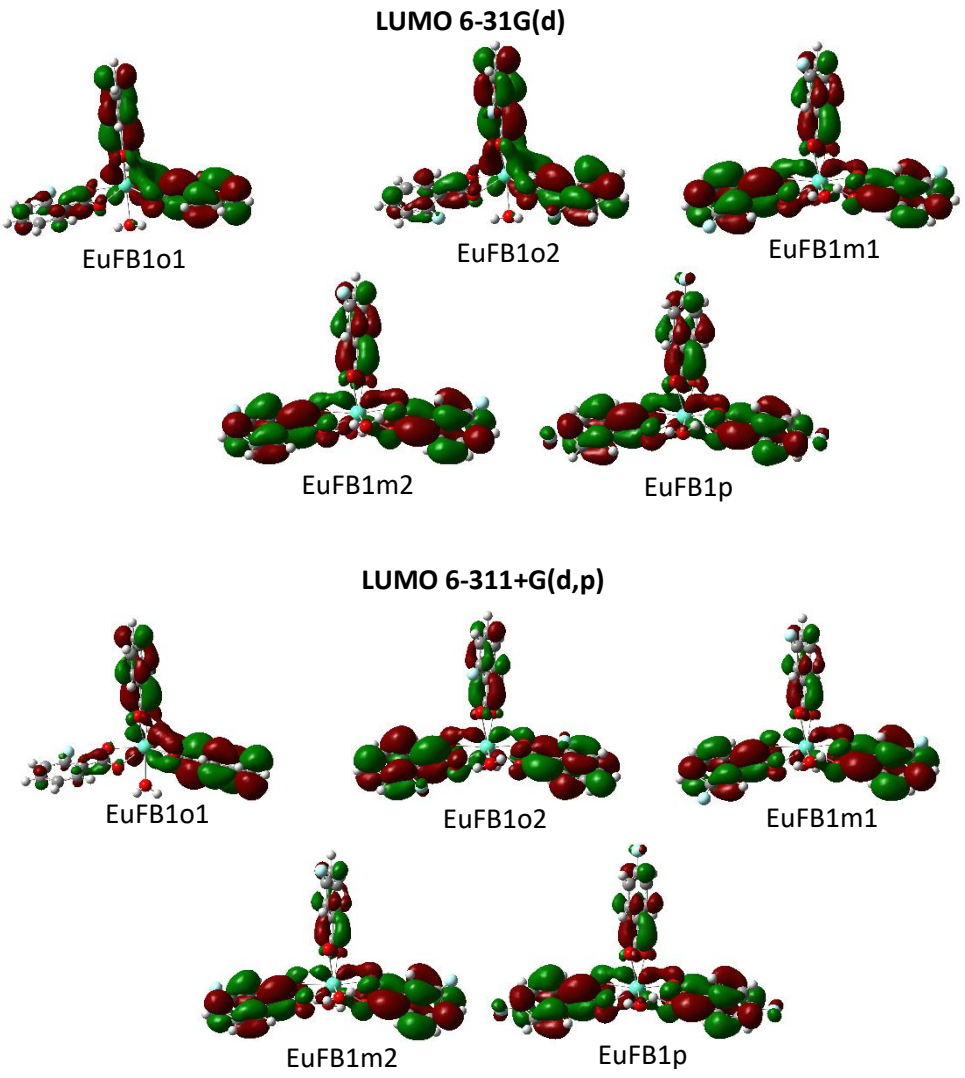

Figure A5. LUMO orbitals as calculated for the 6-31G(d) and 6-311+G(d,p) basis sets for the complexes obtained by moving a single fluorine atom around the ring of a benzoate ligand. Green orbitals are the positive values of the wavefunction, while the red orbitals are the negative values.

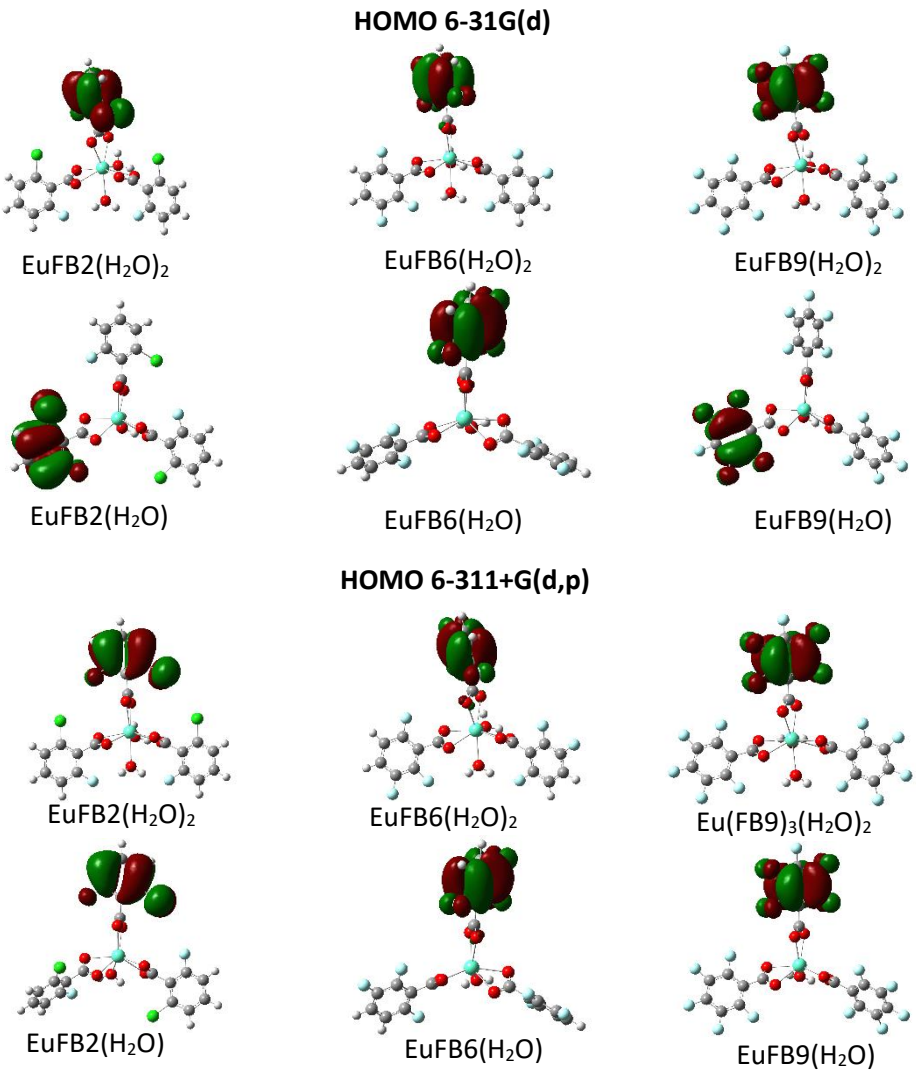

Figure A6. HOMO orbitals as calculated for the 6-31G(d) and 6-311+G(d,p) basis sets for the dihydrate and monohydrate complexes. Green orbitals are the positive values of the wavefunction, while the red orbitals are the negative values.

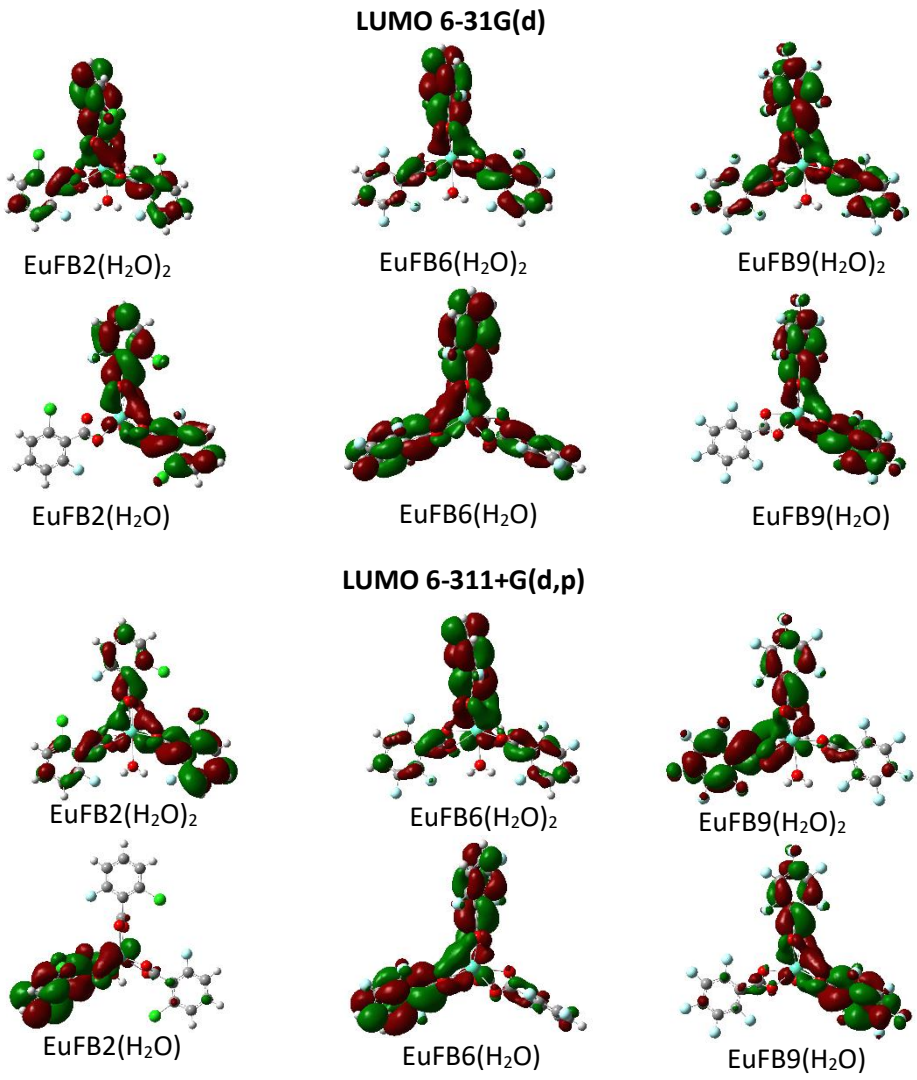

Figure A7. LUMO orbitals as calculated for the 6-31G(d) and 6-311+G(d,p) basis sets for the dihydrate and monohydrate complexes. Green orbitals are the positive values of the wavefunction, while the red orbitals are the negative values.

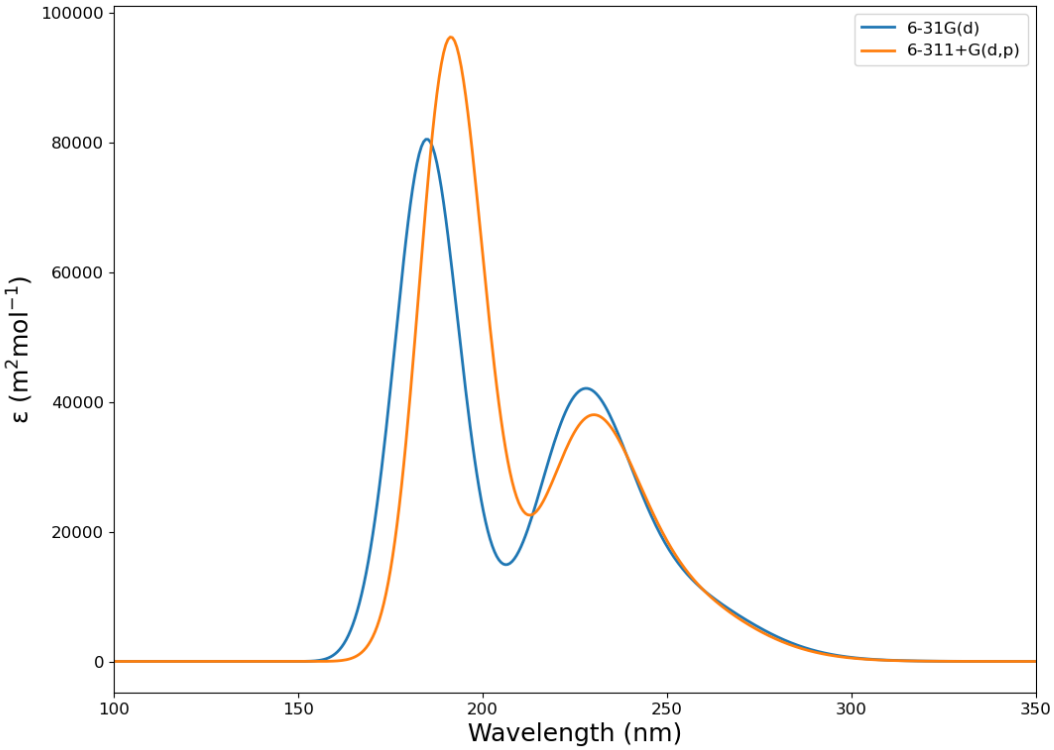

Figure A8. DFT-calculated absorption spectra of the EuFB1/EuFB1o1 complex using the 6-31G(d) basis set (top) and the 6-311+G(d,p) basis set (bottom).

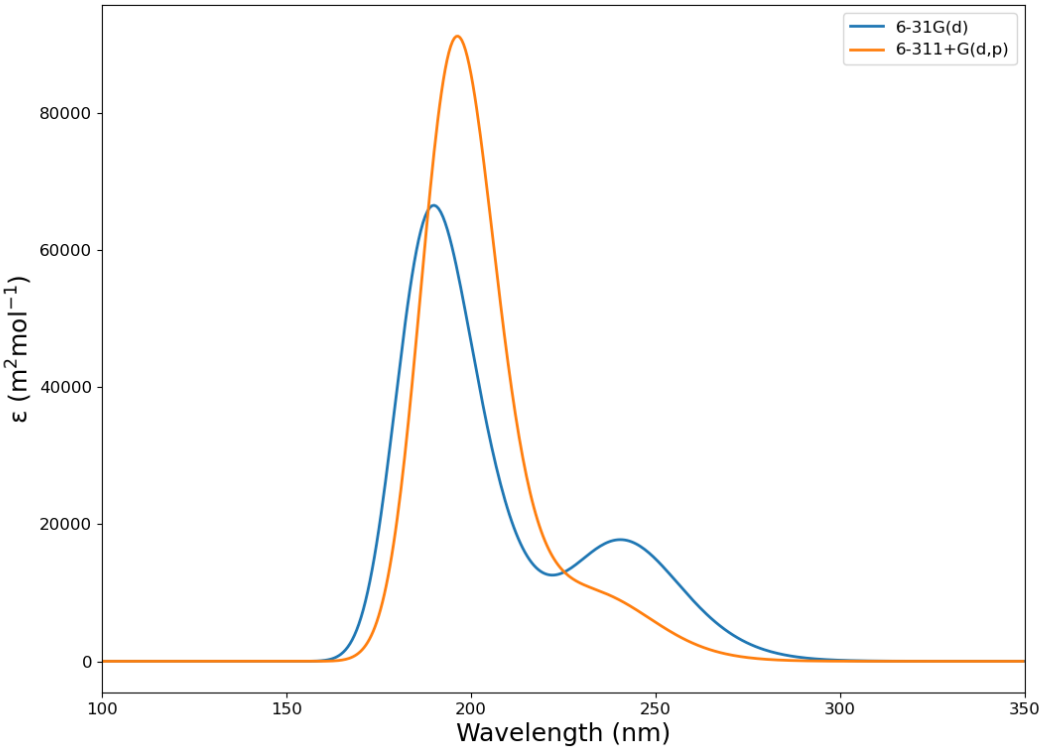

Figure A9. DFT-calculated absorption spectra of the EuFB2/EuFB2(H_2O) complex using the 6-31G(d) basis set (top) and the 6-311+G(d,p) basis set (bottom).

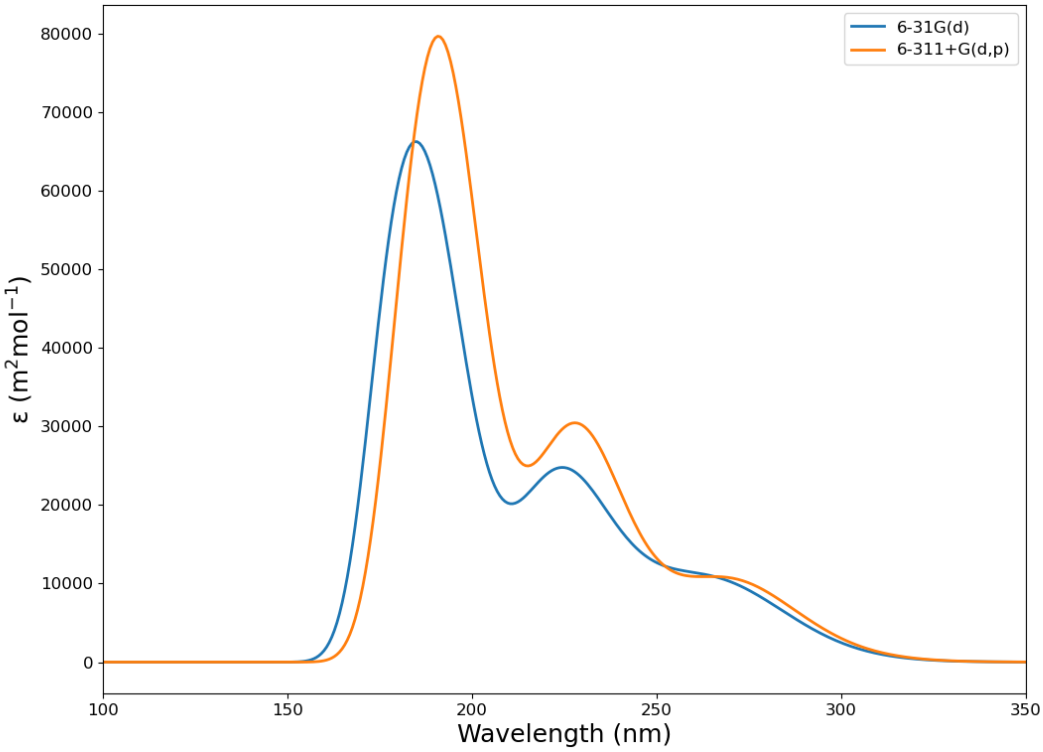

Figure A10. DFT-calculated absorption spectra of the EuFB3 complex using the 6-31G(d) basis set (top) and the 6-311+G(d,p) basis set (bottom).

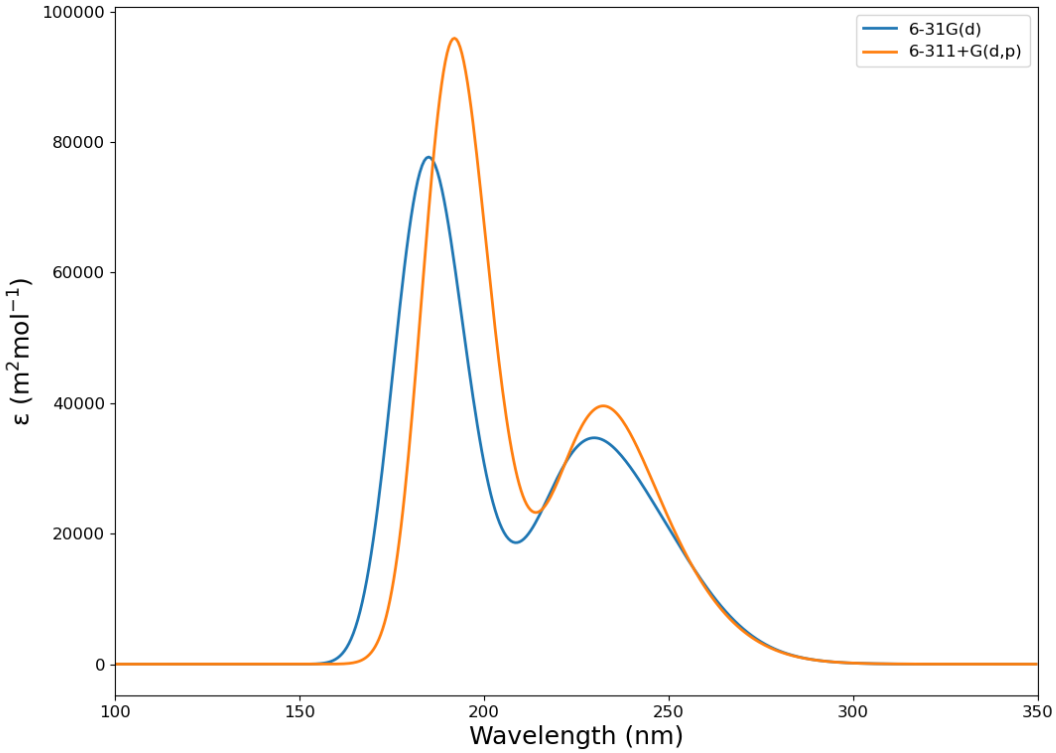

Figure A11. DFT-calculated absorption spectra of the EuFB4 complex using the 6-31G(d) basis set (top) and the 6-311+G(d,p) basis set (bottom).

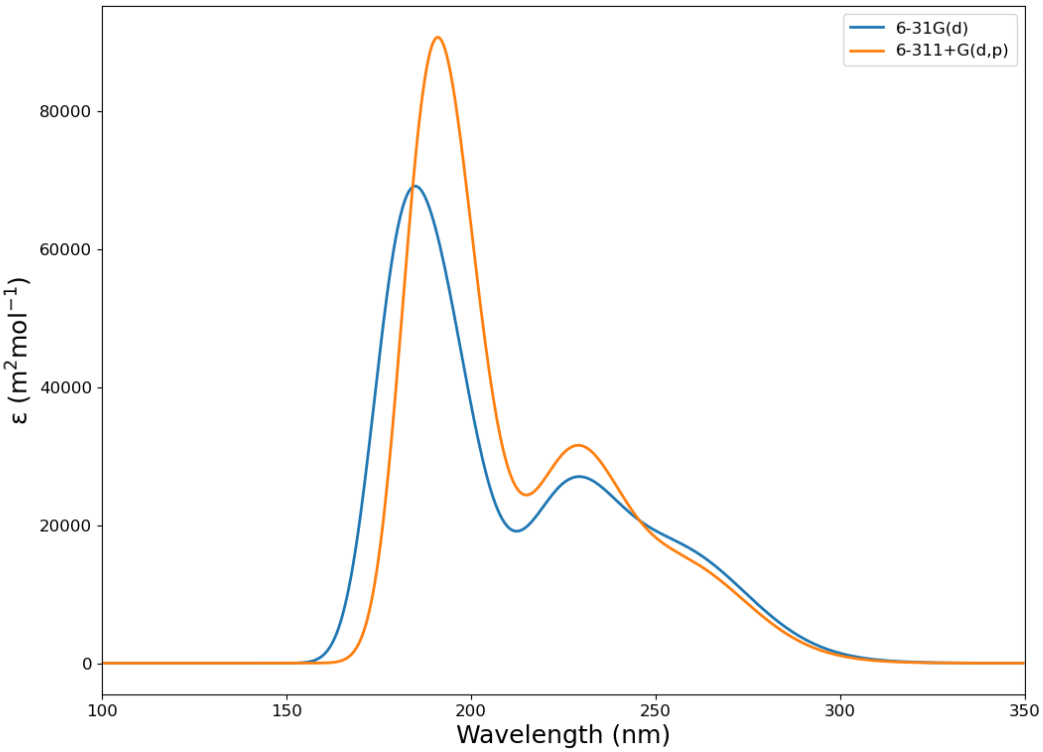

Figure A12. DFT-calculated absorption spectra of the EuFB5 complex using the 6-31G(d) basis set (top) and the 6-311+G(d,p) basis set (bottom).

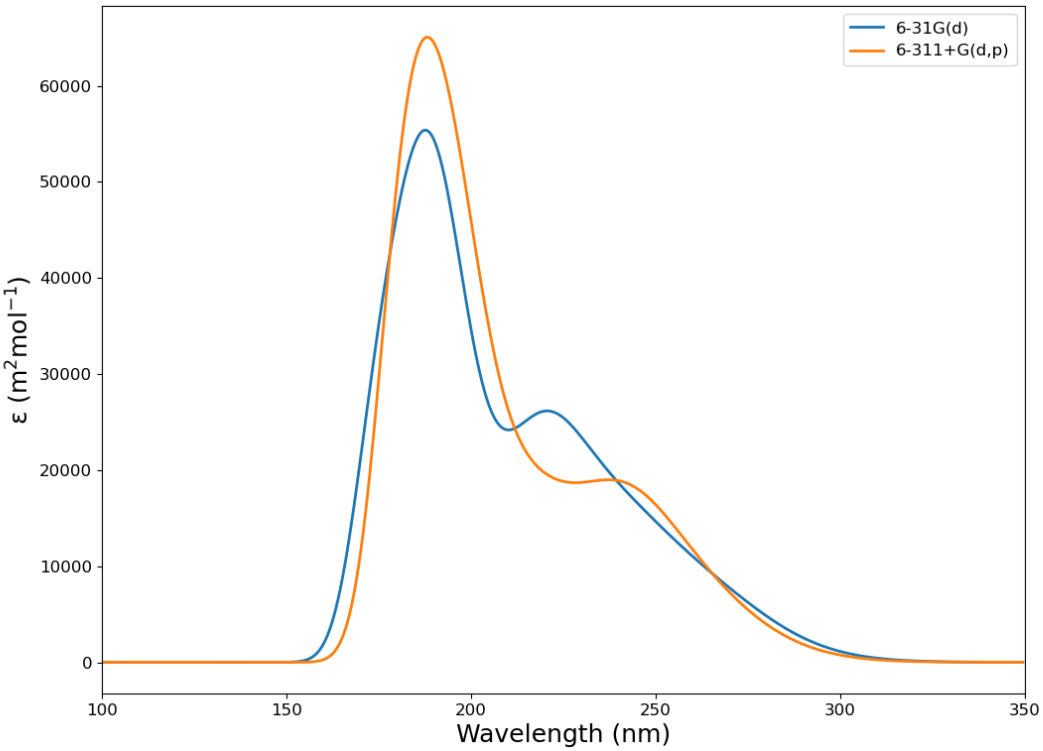

Figure A13. DFT-calculated absorption spectra of the EuFB6/EuFB6(H_2O) complex using the 6-31G(d) basis set (top) and the 6-311+G(d,p) basis set (bottom).

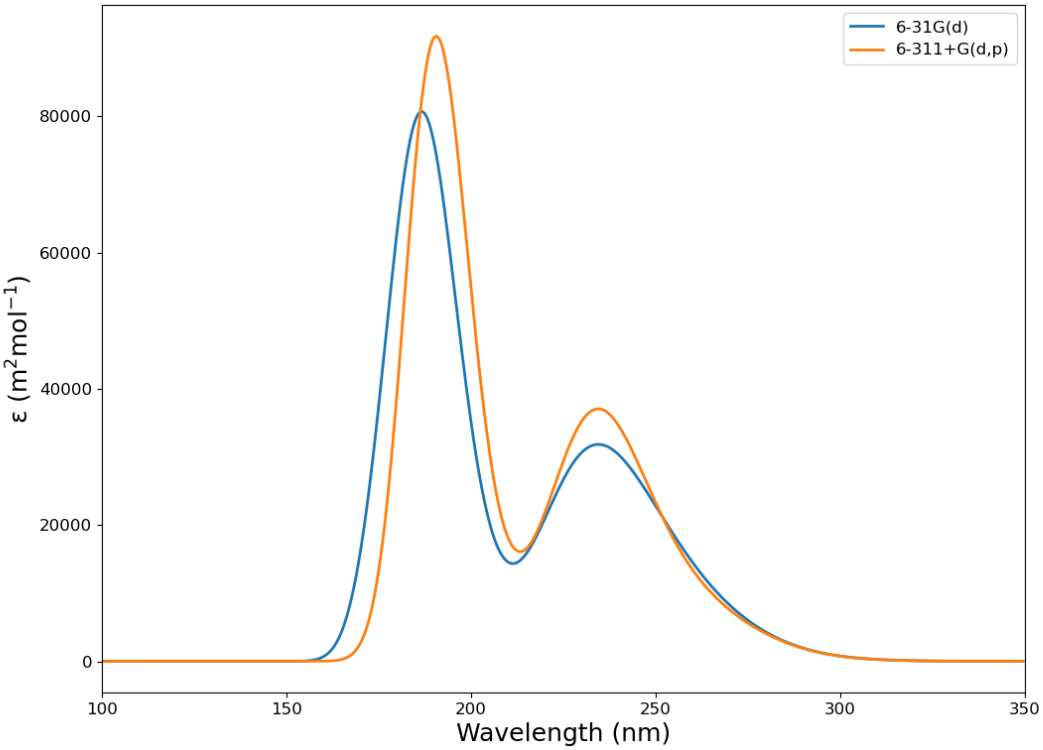

Figure A14. DFT-calculated absorption spectra of the EuFB7 complex using the 6-31G(d) basis set (top) and the 6-311+G(d,p) basis set (bottom).

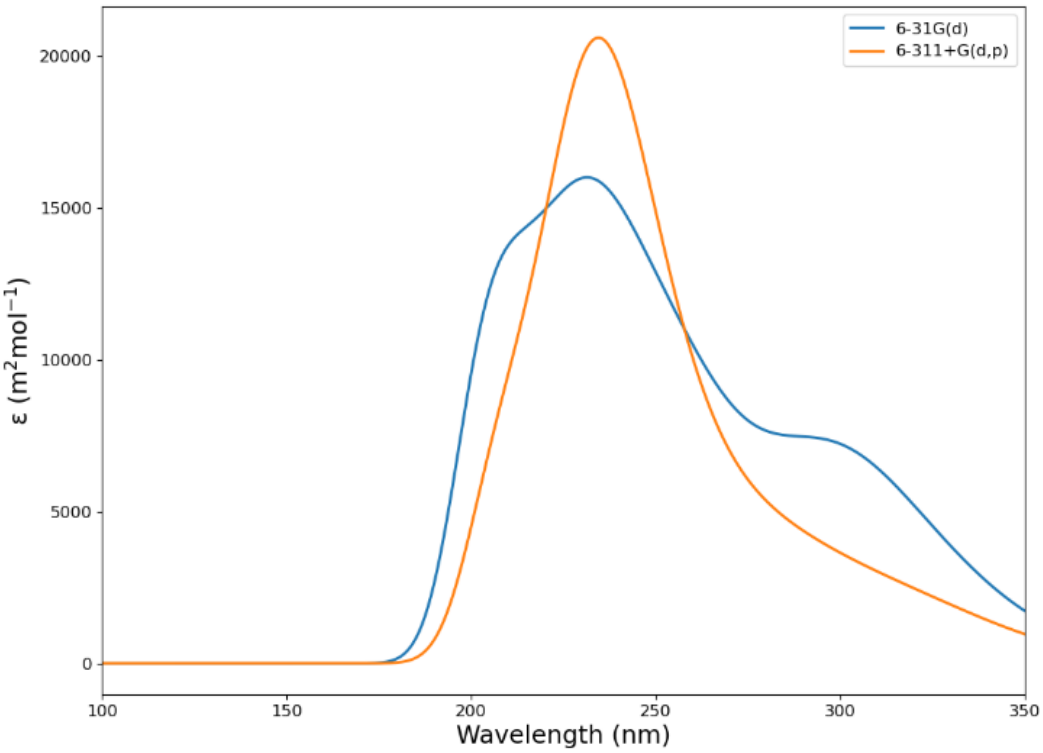

Figure A15. DFT-calculated absorption spectra of the EuFB8 complex using the 6-31G(d) basis set (top) and the 6-311+G(d,p) basis set (bottom).

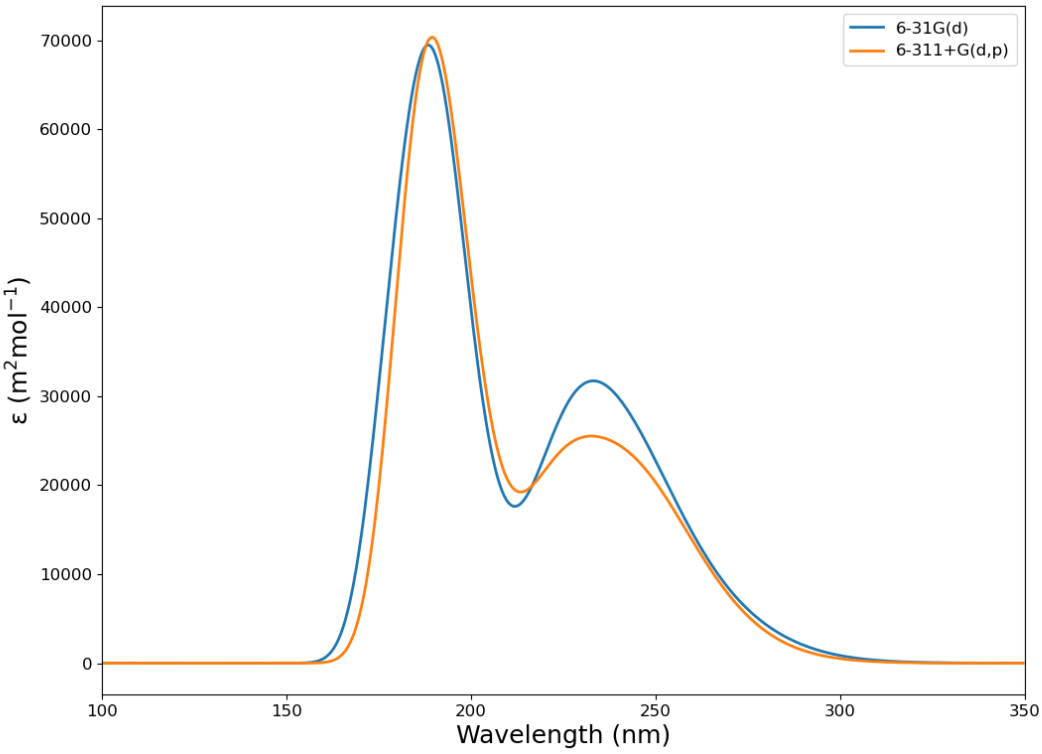

Figure A16. DFT-calculated absorption spectra of the EuFB9/EuFB9(H_2O) complex using the 6-31G(d) basis set (top) and the 6-311+G(d,p) basis set (bottom).

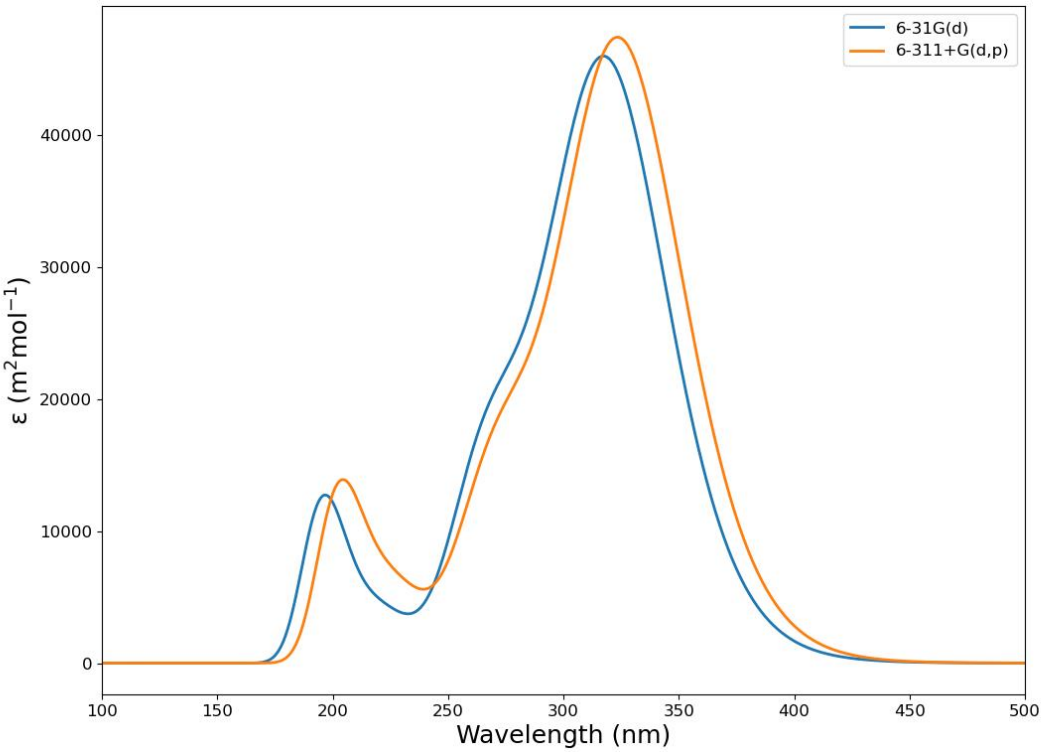

Figure A17. DFT-calculated absorption spectra of the EuTTA complex using the 6-31G(d) basis set (top) and the 6-311+G(d,p) basis set (bottom).

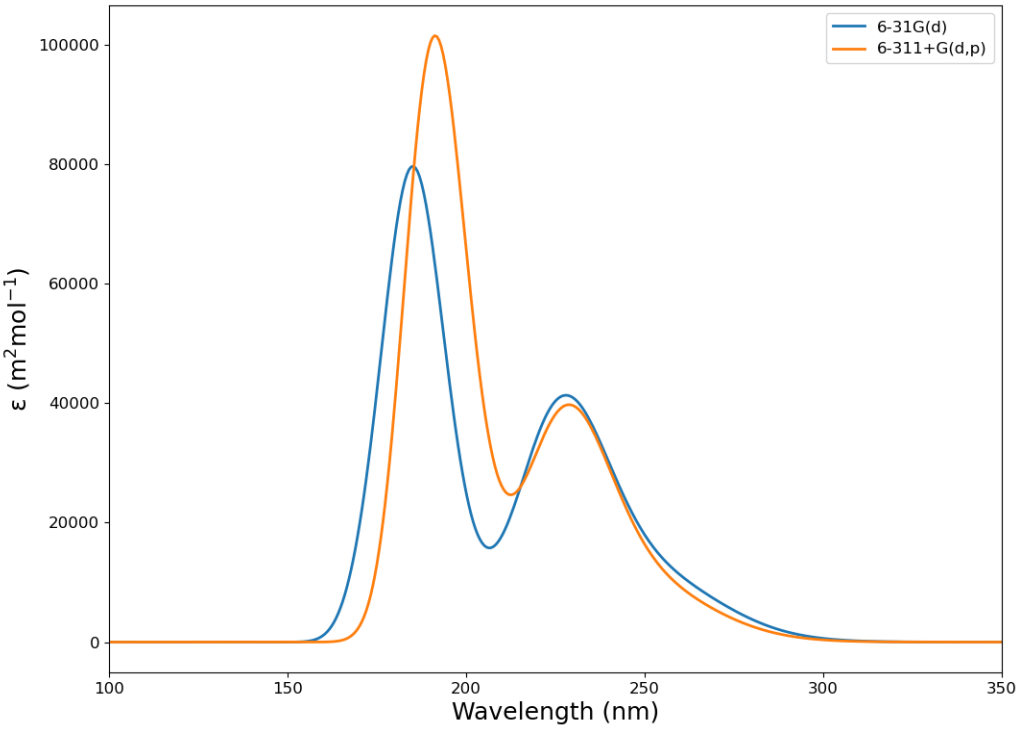

Figure A18. DFT-calculated absorption spectra of the EuFB1o2 complex using the 6-31G(d) basis set (top) and the 6-311+G(d,p) basis set (bottom).

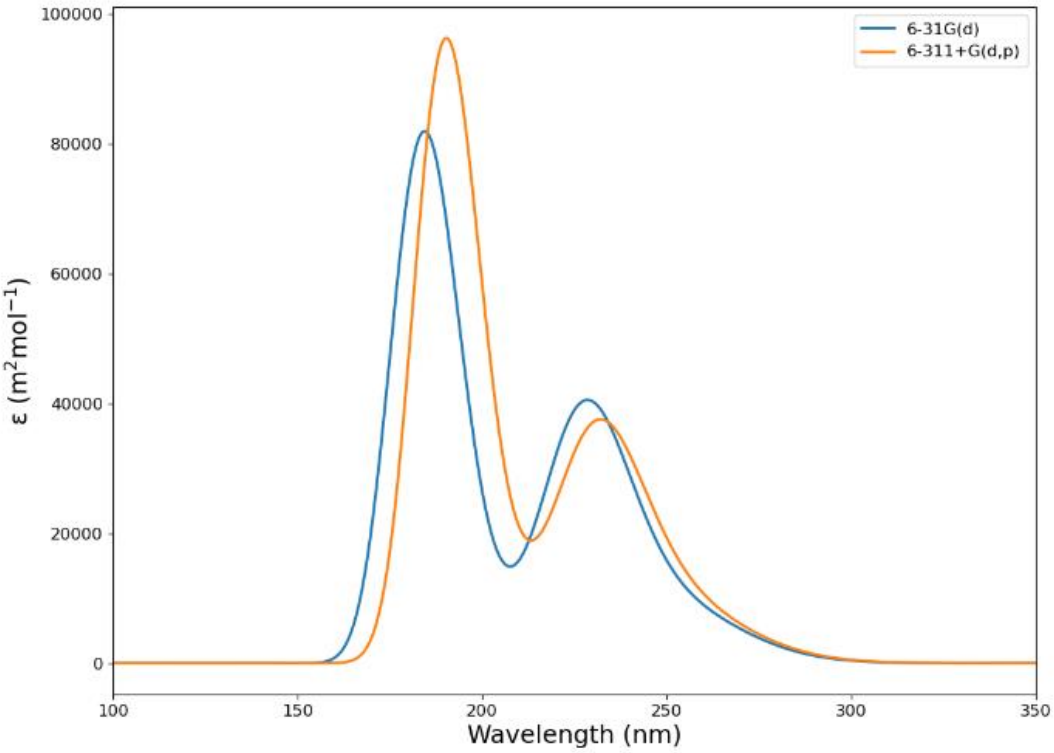

Figure A19. DFT-calculated absorption spectra of the EuFB1m1 complex using the 6-31G(d) basis set (top) and the 6-311+G(d,p) basis set (bottom).

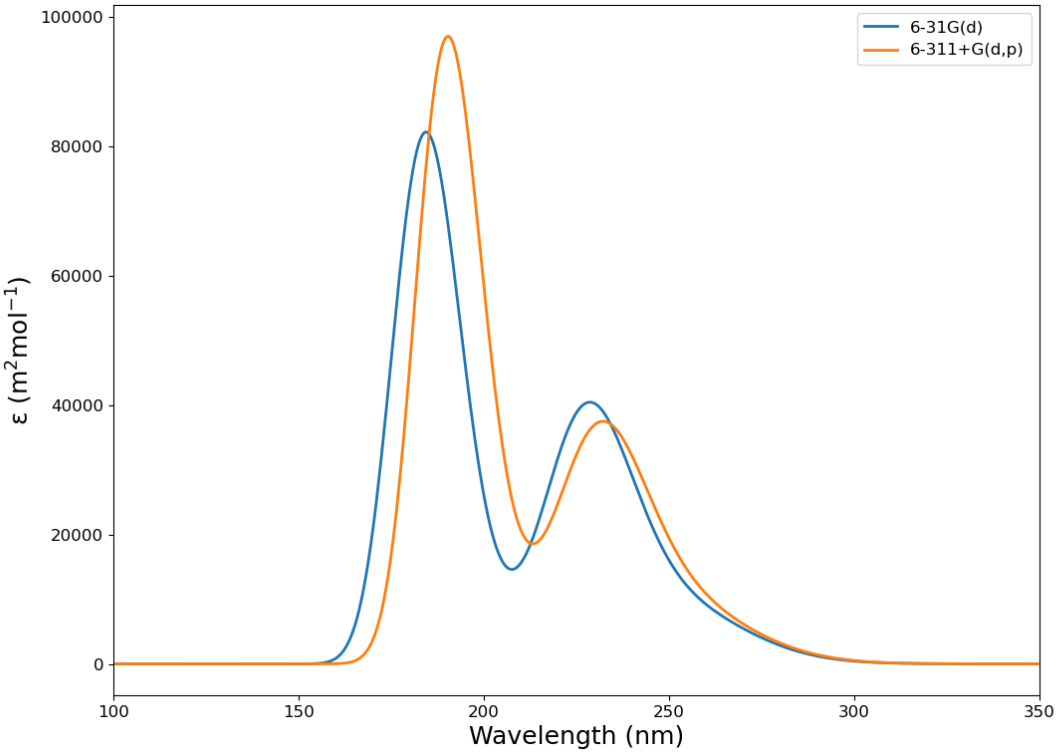

Figure A20. DFT-calculated absorption spectra of the EuFB1m2 complex using the 6-31G(d) basis set (top) and the 6-311+G(d,p) basis set (bottom).

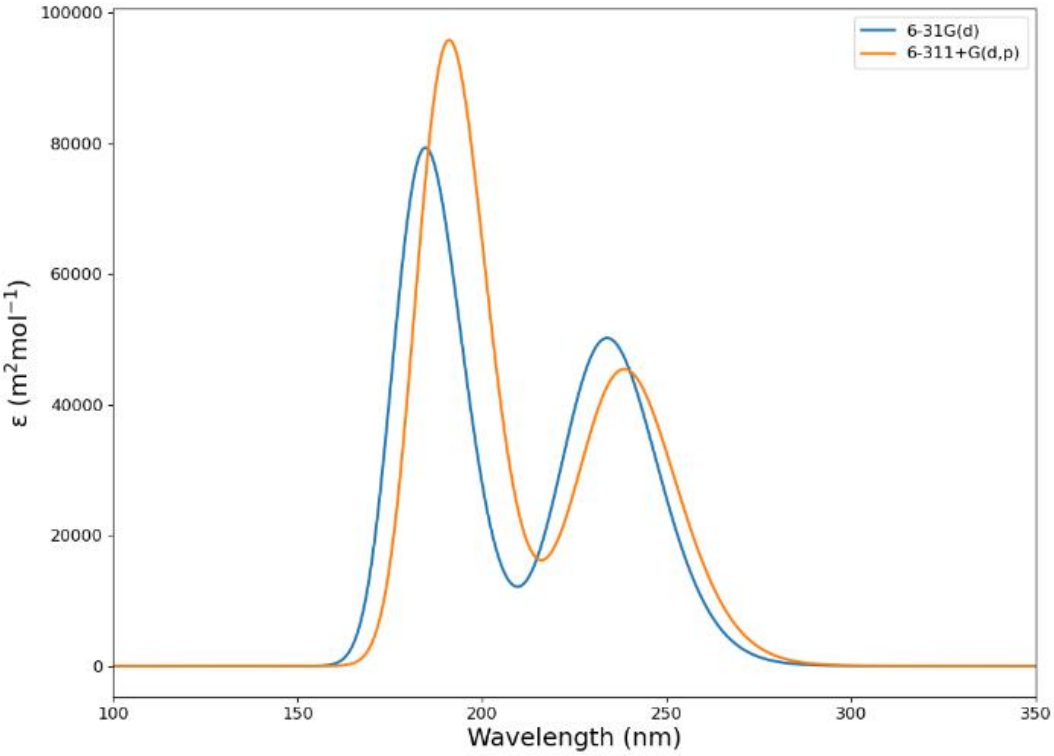

Figure A21. DFT-calculated absorption spectra of the EuFB1p complex using the 6-31G(d) basis set (top) and the 6-311+G(d,p) basis set (bottom).

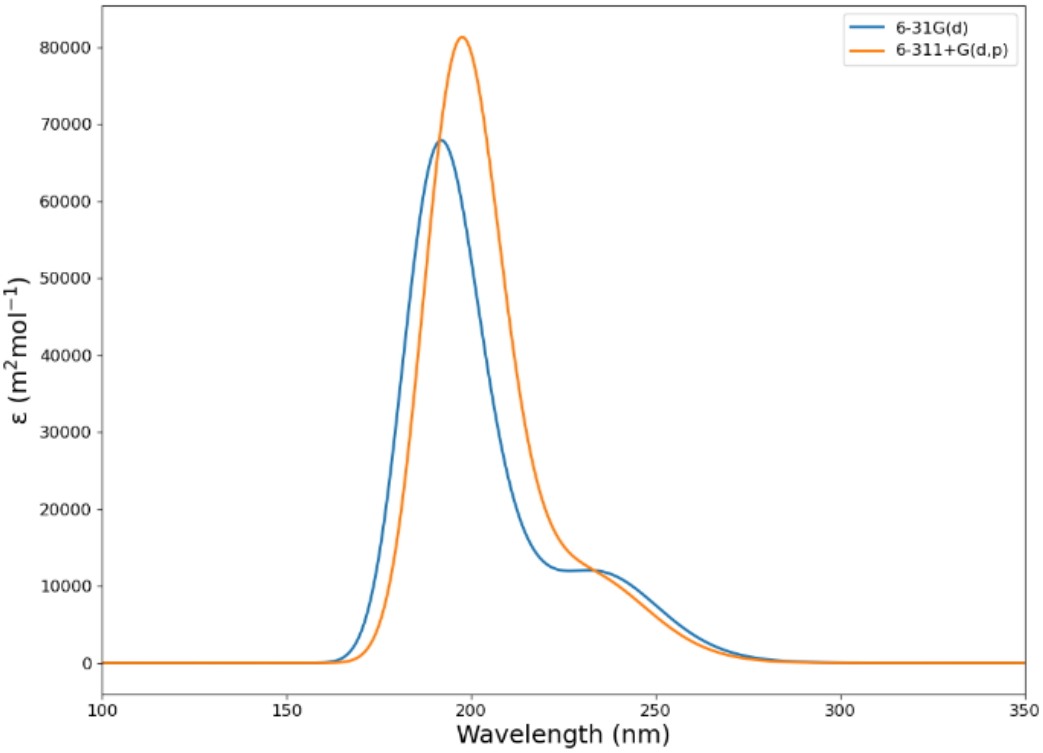

Figure A22. DFT-calculated absorption spectra of the EuFB2$(H_2O)_2$ complex using the 6-31G(d) basis set (top) and the 6-311+G(d,p) basis set (bottom).

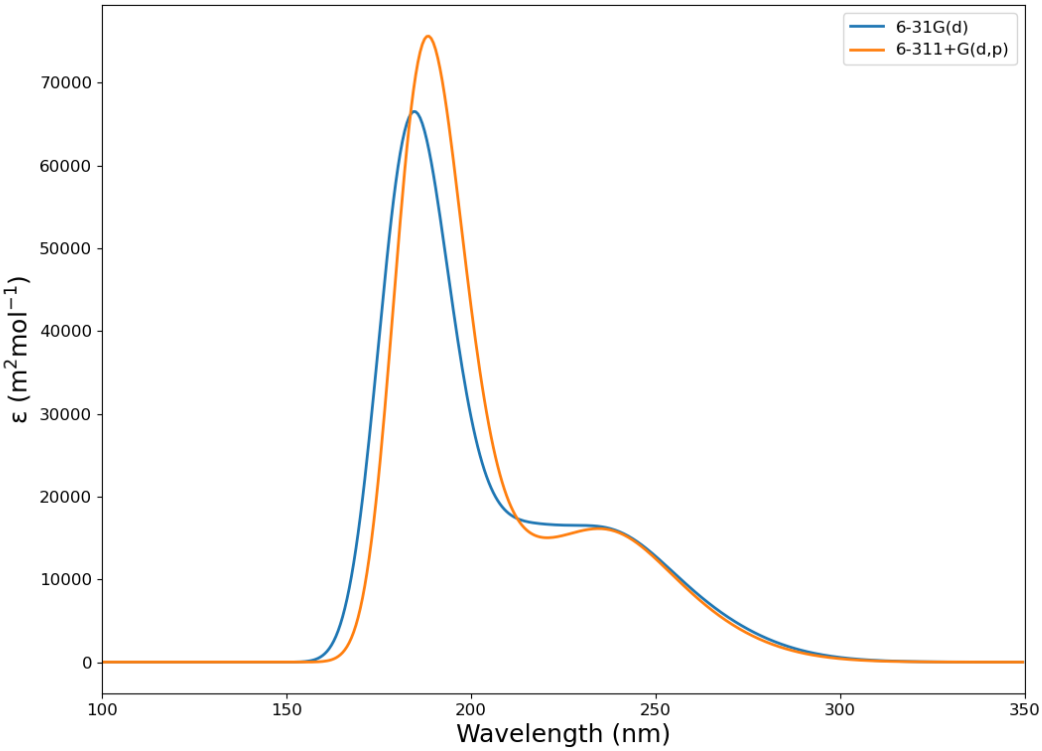

Figure A23. DFT-calculated absorption spectra of the EuFB6$(H_2O)_2$ complex using the 6-31G(d) basis set (top) and the 6-311+G(d,p) basis set (bottom).

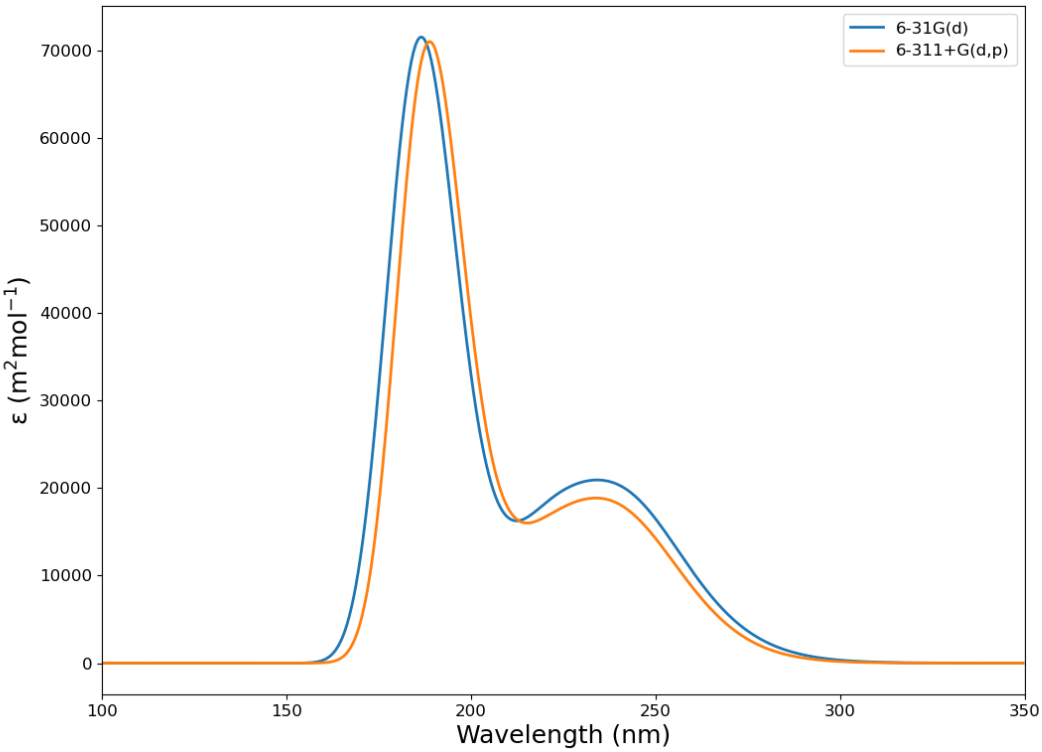

Figure A24. DFT-calculated absorption spectra of the EuFB9$(H_2O)_2$ complex using the 6-31G(d) basis set (top) and the 6-311+G(d,p) basis set (bottom).

Table A1. Lowest singlet and triplet energy levels calculated using the 6-311+g (d,p) basis sets along with calculated ISC, ET energy gaps and experimental luminescent quantum yields (Exp QY).

Complexes	Basis Set	Singlet (eV)	Triplet (eV)	$^5D_0$ (eV)	ΔE_{ISC} (eV)	ET (eV)	Exp QY (%)
EuFB1	6-31G(d)	4.7415	3.5573	2.1449	1.1842	1.4124	15
	6-311+G(d,p)	4.7388	3.5774		1.1614	1.4325	
EuFB2	6-31G(d)	4.8345	3.5875		1.2470	1.4426	10
	6-311+G(d,p)	4.9616	3.6278		1.3338	1.4829	
EuFB3	6-31G(d)	4.5329	3.4646		1.0683	1.3197	10
	6-311+G(d,p)	4.5191	3.4943		1.0248	1.3494	
EuFB4	6-31G(d)	4.9216	3.5947		1.3269	1.4498	5
	6-311+G(d,p)	4.8968	3.6015		1.2953	1.4566	
EuFB5	6-31G(d)	4.6791	3.4921		1.1870	1.3472	10
	6-311+G(d,p)	4.7419	3.5391		1.2028	1.3942	
EuFB6	6-31G(d)	4.6066	3.5950		1.0116	1.4501	20
	6-311+G(d,p)	4.6413	3.6130		1.0283	1.4681	
EuFB7	6-31G(d)	4.6493	3.4890		1.1603	1.3441	45
	6-311+G(d,p)	4.6743	3.5195		1.1548	1.3746	
EuFB8	6-31G(d)	3.7867	2.7371		1.0496	0.5922	0
	6-311+G(d,p)	3.8221	2.8321		0.9900	0.6872	
EuFB9	6-31G(d)	4.6109	3.5508		1.0601	1.4059	15
	6-311+G(d,p)	4.6840	3.5794		1.1046	1.4345	
EuTTA	6-31G(d)	3.3466	2.4478		0.8988	0.3029	23
	6-311+G(d,p)	3.3322	2.4539		0.8783	0.3090	

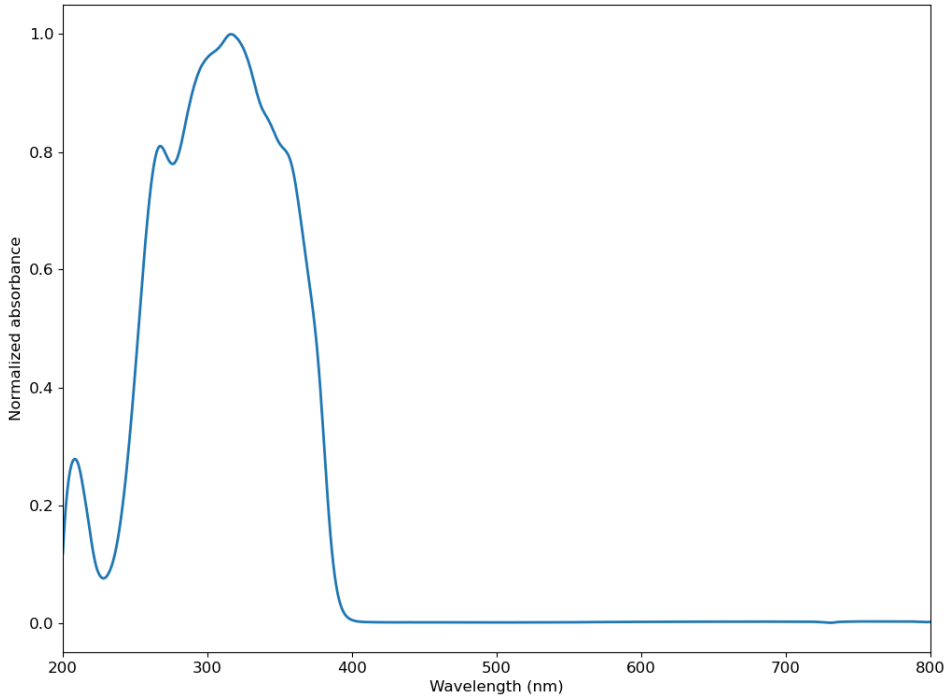

Figure A25. Normalized UV-Vis absorption spectra of TTA. The λ_{max} is 316 nm, with a smaller absorption band at 207 nm. Possible unresolved bands could be present at 268, 297 and 354 nm. The spectrum was normalized to be between 0 and 1.

Table A2. Absorbance, emission, and luminescent quantum yield values for uncoated and coated nanoparticles at different sizes. The absorbance, emission and luminescent quantum yield are also reported for the reference used in the calculation (size does not apply to the reference).

	NP size = 450 nm					NP size = 150-170 nm				
Coating Ratio	**Absorbance**	**Emission Area**	**QY (%)**	**Avg QY (%)**	**ST Dev (%)**	**Absorbance**	**Emission Area**	**QY (%)**	**Average QY (%)**	**ST Dev (%)**
Uncoated	0.3656295	832.9251	1.776757			0.4255752	1092.6156	2.00241592		
	0.3666511	705.6139	1.510859	1.6	0.1	0.3250841	1019.938	2.46313221	2.4	0.3
	0.3624441	687.5191	1.491512			0.3211667	1056.6465	2.58691627		
1-1	0.3354957	1533.7704	3.565633			0.4272185	1578.2711	2.88134165		
	0.2540875	1510.1760	4.666099	4.2	0.5	0.4326254	1759.4516	3.19282408	3.0	0.1
	0.2640960	1447.3447	4.309167			0.4275596	1641.3489	3.01847379		
1-5	0.5776821	6958.5430	9.39491			0.5546743	2245.0041	3.15676533		
	0.5855373	6711.5416	8.998651	9.2	0.2	0.5461447	2342.6851	3.36756411	3.2	0.1
	0.5942433	6865.4505	9.084226			0.5525795	2200.4975	3.13118893		
1-10	0.4315190	6645.0557	12.01052			0.5151846	3321.5184	5.02848309		
	0.4242373	6381.1242	11.80859	11.8	0.2	0.522571	3239.1687	4.8662895	4.91	0.08
	0.4235408	6242.6610	11.58931			0.5216022	3208.0976	4.83605599		
1-25	0.5588419	4157.1340	5.801874			0.4116277	9465.1582	17.934385		
	0.5643589	4218.3740	5.868125	5.85	0.04	0.4173218	9541.7523	17.9500948	18.0	0.2
	0.5668402	4238.1045	5.878874			0.4113301	9542.4404	18.2411463		
1-50	0.2740074	3063.8499	8.721042			0.2708082	8164.6429	23.5146537		
	0.2689446	3094.1449	9.032074	9.1	0.3	0.2686601	8192.9398	23.9412197	23.7	0.2
	0.2615482	3168.0284	9.524024			---		---		
1-75	0.3692428	1651.0316	3.487438			0.345236	7410.5697	16.741668		
	0.4008380	1554.0401	3.043708	3.3	0.2	0.3427901	7496.7286	17.1693241	17.1	0.3
	0.3916529	1640.9488	3.294404			0.3368147	7448.0582	17.3874217		
1-100	0.3504708	2573.9559	5.728125			0.4136566	6092.9614	11.4881917		
	0.3336387	2620.5125	6.166227	6.0	0.2	0.3983974	6094.9412	12.0105447	11.7	0.2
	0.3318786	2582.7789	6.119151			0.4016604	5946.5753	11.6410209		
Eu-TTA	0.5125101	13470.4872								
	0.5122252	13375.0477	---	23	---					
	0.5118893	13345.5651								